BIOPHYSICAL AND NETWORK MECHANISMS OF HIGH FREQUENCY EXTRACELLULAR POTENTIALS IN THE RAT HIPPOCAMPUS

Thesis by

Erik W. Schomburg

In Partial Fulfillment of the Requirements

for the Degree of

Doctor of Philosophy

California Institute of Technology

Pasadena, CA

2014

(Defended January 27, 2014)

Acknowledgements

I am indebted to many people for their guidance, collaboration, discussions, and support during the process of completing my Ph.D. After 8 years navigating through three departments at two schools, the full list has grown rather long. What was pivotal for me, and doubtless many others, was how welcoming and excited the scientists and staff were in each place I went. Caltech's CNS community and NYU's Neuroscience Institute embraced me and never questioned why a physics grad student, from another school in the latter case, would be hanging around. KLab's incredible range of expertise and creative approaches to understanding the mind was formative. I could not have followed that experience with a better opportunity than a move to the Buzsaki lab, where everyone was passionately pursuing the answers to the same questions I was asking, and doing so with techniques on the forefront of the field.

I wish to highlight some contributions that enabled and shaped my doctoral education:

- Christof Koch, my thesis advisor at Caltech. Christof's passion for neuroscience and the scope of his ideas are inspiring. I would not have even started if not for his willingness to take a chance on an embarrassingly naive student, and his patience as I began my journey.
- Costas Anastassiou, my research mentor during his time as a postdoc in KLab. Costas's steady and clearheaded support during the frequent times when I doubted my work and my abilities were deciding factors getting me through my difficulties. I benefited greatly and learned much from his commitment to building a tight-knit and engaged team in KLab, as well his ability to view the details of my projects in a larger context as part of a grander endeavor to understand neural systems.
- Gyuri Buzsaki, my unofficial thesis advisor at NYU, and his astounding energy as he answers one question about the brain and immediately asks three more. In addition to his obsession with the mechanistic details underlying the operation of larger neural systems, and every step in between, he secured my admiration with his compassion for the scientists he works with in pursuit of this goal.

- Kenji Mizuseki, whose unbelievable openness, helpfulness, and insight every single time I had even the most trivial question often helped me break through crucial barriers.
- Jerome Pine and Henry Lester, for serving on my committee and reading this thesis. Their patience and flexibility, as well as insightful feedback during my exams, helped me avoid much of the unnecessary stress many other students are forced to deal with. In addition, I greatly appreciate Henry, acting as my official PhD advisor during my time at NYU, for trusting me to stay on track.
- Gaute Einevoll, for showing me that talented scientists not involved in my projects saw their value. His generosity taught me how enjoyable it is to be part of a worldwide scientific community.
- Those who helpfully provided logistical and material support: Heather Hein, Joanne Meraz, Heather McKellar, Donna Driscoll, Philippe Brieu, Dan Caballero, and Nicholas Avrutin.
- The brilliant and warm members of the Koch and Buzsaki labs, their feedback, support, insight, criticism, and, most of all, their friendship.
- Some lab alumni that I still have not met, but who laid groundwork with their ‘Gold standard’ models and experiments: Carl Gold and Sean Montgomery
- My family, especially Mom and Dad, for their infinite reservoir of love and support as I struggled to find my place, regardless of how far I strayed from home.
- The Caltech Alpine Club and the Caltech Y for showing me how to engage in and organize deeply rewarding extracurriculars.
- The students I had a chance to work with, including Randall Lin, Nicholas Swenson, and those I had in class, who showed me I can earn my keep (and have fun) by helping others in addition to myself learn about science.
- The NIH, HFSP, and Mathers Foundation grants that funded the research.
- Finally, Christof at Caltech, and Dima Rinberg and the Alex9 Coffee Club at NYU, for so generously providing access to as much coffee as my heart (unwisely) desired, without which I would have taken at least another two years to finish.

Abstract

A fundamental question in neuroscience is how distributed networks of neurons communicate and coordinate dynamically and specifically. Several models propose that oscillating local networks can transiently couple to each other through phase-locked firing. Coherent local field potentials (LFP) between synaptically connected regions is often presented as evidence for such coupling. The physiological correlates of LFP signals depend on many anatomical and physiological factors, however, and how the underlying neural processes collectively generate features of different spatiotemporal scales is poorly understood. High frequency oscillations in the hippocampus, including gamma rhythms (30-100 Hz) that are organized by the theta oscillations (5-10 Hz) during active exploration and REM sleep, as well as sharp wave-ripples (SWRs, 140-200 Hz) during immobility or slow wave sleep, have each been associated with various aspects of learning and memory. Deciphering their physiology and functional consequences is crucial to understanding the operation of the hippocampal network.

We investigated the origins and coordination of high frequency LFPs in the hippocampo-entorhinal network using both biophysical models and analyses of large-scale recordings in behaving and sleeping rats. We found that the synchronization of pyramidal cell spikes substantially shapes, or even dominates, the electrical signature of SWRs in area CA1 of the hippocampus. The precise mechanisms coordinating this synchrony are still unresolved, but they appear to also affect CA1 activity during theta oscillations. The input to CA1, which often arrives in the form of gamma-frequency waves of activity from area CA3 and layer 3 of entorhinal cortex (EC3), did not strongly

influence the timing of CA1 pyramidal cells. Rather, our data are more consistent with local network interactions governing pyramidal cells' spike timing during the integration of their inputs. Furthermore, the relative timing of input from EC3 and CA3 during the theta cycle matched that found in previous work to engage mechanisms for synapse modification and active dendritic processes. Our work demonstrates how local networks interact with upstream inputs to generate a coordinated hippocampal output during behavior and sleep, in the form of theta-gamma coupling and SWRs.

Table of contents

Preface

Since Richard Caton first reported his measurements of electrical fluctuations in the brains of dogs and primates, and especially after the significance of these phenomena were emphasized by Hans Berger's development of electroencephalography and discovery of oscillatory patterns related to behavior, sensation, and epilepsy, brain scientists have struggled to understand what these signals represent. Extracellular electrical recordings of the brain (EEG outside the head, ECoG on the brain surface, LFP within the brain) exhibit a hierarchy of oscillatory patterns, with various relationships to behavior and cognitive states. These electrical signals are related to neural activity, and neural networks (biological and theoretical) also support a plethora of oscillatory dynamics. The relationship between the LFP and the network activity, however, are variable, dependent on many factors, and often not straightforward (see, for example, Chapters 3-5 of this thesis).

Though the biophysical foundations of how neural elements generate extracellular electric signals are relatively well understood, and several heuristic principles were developed for how these "microscopic" signals combine into measurable "macroscopic" signals, no generally accepted rules could be established for precisely which processes contribute to extracellular potentials, how much they contribute, and over which spatiotemporal scales are they integrated. The primary reason is that the generation and integration of extracellular potentials depends on the precise morphological and physiological properties of the neuron population in the region, as well as their

anatomical organization and temporal coordination, all of which vary within the brain and depend on the global state of the network.

It seems then that, while general principles can be formulated, our understanding of each electrical pattern in different brain structures must be separately dissected. The aim of this thesis is to refine our understanding of how the contributions of LFP generators depend on the spectral domain of interest, illustrate limitations of LFP analysis for inferring details of network activity, and improve our methods for dissecting LFP patterns. Furthermore, in the process of using hippocampal-entorhinal LFPs and unit activity towards these ends, we gained a better understanding of how the networks of the hippocampal formation operate and interact. (Or, more accurately, *I* gained a better understanding of how seductively tractable their workings appear, but how exasperatingly malleable they turn out to be. What I have learned, however, has aroused an intense desire to delve deeper into how the hippocampus, and neural circuits in general, are dynamically coordinated to drive our behavior, sustain our emotions, and enable our cognition.)

As with nearly any route to a Ph.D., the goals at the outset and in the final stages differed in their scope and theme. I initially hoped to develop a working model of LFPs, which could then be used to estimate the contributions of various possible sources of extracellular electric potentials. Furthermore, an accurate way to estimate extracellular fields arising within a model network could be used to begin an investigation of the "feedback problem": how do the electric potentials and fields generated by activity within a neuronal population affect the activity of the population? Might they increase or

decrease synchrony, or provide a way for neurons to interact virtually instantaneously? Previous work by my advisors and colleagues has shown this is possible, in principle, but a working model would greatly enhance our ability to predict if and when it may happen in practice.

During the course of my research, however, it became clear that answering this question will require a combination of advanced skills in algorithm development and optimization, clever methods of approximation and parallelization, in addition to excellent intuition for the theory of electric fields and circuits. While it is a worthy goal, my interests drifted toward the ways in which biological networks of neurons process, encode, and recall information, and how they coordinate their activity to perform these functions. The efforts described in this thesis to understand the network activity reflected in hippocampal extracellular potentials served both my initial goal of elucidating the biophysics underlying their generation and my present goal of understanding how network activity in the hippocampus relates to its hypothesized roles in spatial navigation and episodic memory.

My research additionally took a turn from primarily a modeling effort to one focused on data analysis of experimental recordings. My initial plan was to model many of the rich LFP dynamics exhibited by the rodent hippocampus while the animal is navigating through its environment, some aspects of which are presented in Chapter 4. These phenomena are quite complicated, however, arising from interactions between regions and within local circuits that are not yet well understood. To simplify the problem while maintaining a direct connection to experimental measurements, I shifted to first

model a phenomenon with fewer components, the sharp wave-ripple complex of the hippocampal area CA1. This work led to a better understanding of how high-frequency features of LFPs can be generated by non-synaptic currents, and it illustrated a case in which different kinds of network activity could give rise to similar signals in overlapping spectral bands.

The goal in the second part of my thesis research then became to differentiate these distinct processes and characterize how they related to activity in local and afferent regions. This understanding will equip future experimental and theoretical efforts with better frameworks and hypotheses from which to begin. For example, many theoreticians are presently trying to understand how multiple distinct gamma oscillations may arise within the same network. But the goals and relevance of such investigations are greatly impacted by what the LFP recordings motivating the question reflect: (1) oscillations that emerge from the local network, or (2) local activity entrained by afferent input, or (3) purely synaptic input that does not substantially affect the spiking of the targeted neurons. While I am very interested in the network and cellular mechanisms underlying the emergence of network oscillations, questions about this are related but distinct from the biophysics of LFP generation.

This thesis is structured in the following manner. There are three primary sections: (1) an introduction, describing the biophysical foundations of the LFP and our modeling techniques, as well as background on hippocampal LFP patterns; (2) our methods and results modeling hippocampal LFPs; and (3) the analysis and interpretation of high-frequency extracellular signals in the rat hippocampus. A concluding chapter summarizes

the main conclusions and places them in the context of today's investigations into brain networks, speculating on broader implications and outlining necessary future research.

The work presented here built on an immense amount of effort exerted by numerous other individuals. The following list ascribes proper credit for work described in the remaining chapters that was not performed by me.

- The pyramidal cell model used in Chapter 3, which formed the foundation for a large portion of this thesis, was built by Carl Gold. It is described in detail in his Caltech thesis from 2007, "Biophysics of extracellular action potentials."
- The basket cell model used in Chapter 3 was built by Anja Norenberg, Hua Hu, Peter Jonas, and their colleagues, and generously provided by Peter Jonas.
- The surgeries and experiments which produced all of the data analyzed in Chapters 4 and 5 were performed in the Buzsaki laboratory at Rutgers University and NYU. The students and postdocs who led those experiments (and they were surely assisted by others in the process) are Kenji Mizuseki, Sean Montgomery, Kamran Diba, Antal Berenyi, John Long, and Andres Grosmark.
- The data preprocessing, spike sorting, and behavioral/sleep state annotation for the largest portion of the data I analyzed were performed by Kenji Mizuseki. He additionally continually provided assistance regarding its organization, results from his own analysis, and ideas for new analysis.
- Data preprocessing and behavioral annotation for the additional data sets used here were performed by Sean Montgomery, David Sullivan, and Antal Berenyi.

- The ICA source separation and portions of the analysis of its output were performed by Antonio Fernandez-Ruiz.
- Extensive critical comments and suggestions throughout the research projects, as well as assistance with the composition and editing of Chapter 3 during its submission to the Journal of Neuroscience, were provided by Costas Anastassiou.
- The development of the NEURON software package, its continued maintenance and improvement, as well as assistance above and beyond the call of duty in implementing models, warrants acknowledgment of Michael Hines and Ted Carnevale.
- A few Matlab routines used here, as well as data visualizers for inspection, were written by alumni of the Buzsaki lab, including Michael Zugaro, Lynn Hazan, and Kenneth Harris. All of the remaining analysis code was otherwise either written by me or included in standard Matlab distributions.

I. Introduction

1. Modeling neural extracellular potentials

1.1 Basic biophysical principles, assumptions, and approximations

From the surface, the brain looks like a soft but relatively smooth, solid mass of tissue, not unlike many other organs in the body. The situation is not drastically different when the brain is sliced and examined with a low power light microscope, except for the appearance of some inhomogeneity and layering visible as changes in coloring. Once individual cells are stained, hints of the complexity emerge, and higher-powered microscopy (especially electron microscopy) reveals a dense and intricate "milieu" of cells, membranes, and other organic scaffolding (Syková & Nicholson 2008, Lichtman & Denk 2011, Bock et al. 2011). Accurately modeling charge conduction would appear to be non-trivial, yet experimental measurements of brain conductivity indicate that the extracellular milieu can be treated as an ohmic conductor with surprising accuracy on the frequency scales of interest to the neurophysiologist (Plonsey & Heppner 1967, Logothetis et al. 2007).

Furthermore, only a subset of all the processes in this complex cellular network need to be included in a model of the electrical recordings we wish to understand, i.e., those processes that involve substantial transmembrane ion currents on appropriate timescales. For example, while glial cells are increasingly recognized as important participants in neural function (Araque & Navarrete 2010, Han et al. 2013), their membrane currents change on slower timescales than the neuronal processes that

generate the electrical signals in the 1-2000 Hz frequency range that is typically studied in the brain (Mitzdorf 1985, Konnerth & Orkand 1986, Roitbak et al. 1987). We considered the additional possibility that presynaptic axon terminal currents may contribute to extracellular signals in this range. Small diameter fibers, myelination, and the resulting high input impedance and small current amplitudes, combined with variable segment orientations, and multiphasic sink-source time courses, suggest little direct contribution of presynaptic currents to cortical LFPs (but see Mitzdorf 1985). We did not exhaustively explore all possible cases; for example, the final axon segments of axo-axonic interneurons (chandelier cells) in CA1 are dense and oriented similarly along the pyramidal cell axon initial segments. Our numerical simulations using reconstructed basket cell axons (Section 3.3.3), however, were consistent with a minimal contribution of their presynaptic axon currents. Moreover, recordings of extracellular potentials elicited by single interneuron APs in slice experiments indicate that nearly all of the LFP signal following a local interneuron spike is generated by $GABA_A$ receptor-mediated postsynaptic currents (Glickfeld et al. 2009).

Finally, an important assumption in modeling neuronal transmembrane currents is the principle of charge conservation. To a good approximation, we usually may treat the intracellular and extracellular potentials independently, because the transmembrane resistance is much greater than the resistance of the extracellular space (Clark & Plonsey 1966). [This assumption may need re-evaluation, however: when a neuron is operating in the nonlinear regime near threshold, the extracellular field can significantly influence its dynamics (Anastassiou et al. 2010, 2011).] The intracellular potentials and currents, and

the resulting transmembrane current, are therefore typically calculated assuming a uniform and constant extracellular potential. From the extracellular viewpoint, transmembrane currents are sources and sinks of current. Conduction phase delays (or charge propagation effects) are also negligible at neurophysiological timescales (i.e., slower than a few microseconds, or hundreds of kHz in frequency terms) (Plonsey & Heppner 1967, Holt 1998). As a consequence, the intracellular and extracellular spaces are considered to be electrically neutral. Any charge flowing into a neuron must be balanced by an equal amount of charge flowing out. This charge conservation rule has two main consequences for the topics of this thesis. (1) Individual neurons to be modeled as electrical circuits with appropriate passive and active circuit elements linking fiber segments to each other and to the extracellular space. (2) The total transmembrane current for a single cell has no monopole moment, and so we often use our intuition about electric multipoles when conceptualizing the contributions of neuronal elements to extracellular potentials.

1.2 Background and motivation

In working out the biophysical origins of extracellular potentials, as well as improved analysis techniques such as current source density (CSD) estimates, researchers displayed impressive intuition and analytical skills that allowed them to develop a solid foundation for understanding how neural activity is converted to measured voltages. The biophysics of how transmembrane voltages lead to intracellular and transmembrane current flow were developed in stages, from active membrane dynamics (Hodgkin &

Huxley 1952), to core-conductor theory (Clark & Plonsey 1966), dendritic synaptic integration (Rall 1967), extracellular current flow (Plonsey & Heppner 1967), extracellular potentials from single cells (Rall 1962, Clark & Plonsey 1968) and excited populations (Rall & Shepherd 1968, Nicholson & Llinás 1971), to continuous field descriptions (Nicholson 1973). Several approximations (some of which were described in the previous section) justified by the timescales, temporal coordination, and anatomical symmetries inherent in many neural systems allow relatively simple mathematical transformations to estimate the spatial distribution of physiological sources of recorded electric potentials (Nicholson & Freeman 1975). These theories and models showed the importance of electrical and morphological properties of neurons, as well as the geometric arrangement and temporal coordination of the population.

Furthermore, such work also led to a number of basic principles, described and justified most comprehensively in Mitzdorf (1985), which guided researchers intuition regarding the origin and meaning of LFP signals to this day. This includes the rule of thumb that LFPs best reflect excitatory postsynaptic currents (EPSCs) in the neighborhood of the recording electrode. Mitzdorf (1985) based this conclusion of quantitative comparison of the estimated contributions of various possible sources to CSDs in the cortex. By considering the rough time course and geometry of individual sources, as well as how they sum and cancel in idealized neurons and populations, (Mitzdorf 1985) showed that EPSCs are best able to constructively combine into macroscopic signals in typical natural neocortical scenarios. Despite showing that somatic APs can combine effectively in some experimenter-evoked or epileptic

conditions that result in hypersynchronous firing, as well as providing examples of dendritic AP and inhibitory postsynaptic current (IPSC) signatures, (Mitzdorf 1985) argued that these were exceptions rather than the rule.

In some sense, this thesis is about exceptions, refinements, and illustrative cases that show, while this rule of thumb may be true much of the time, it cannot be relied upon for inferring details of network activity. Further investigation should seek to illuminate how typical physiological changes modify the archetypal models underlying the framework developed by Mitzdorf and her predecessors. For instance, how do synaptic barrages, such as those leading to the "high conductance state" of neurons in unanesthetized intact animals (Destexhe et al. 2003), change the amplitude, distribution, and time constants of the synaptic currents. On one hand, a depolarized membrane and concurrent excitatory input will amplify inhibitory synaptic currents and their LFP contributions. On the other hand, IPSC dipoles are likely to be more compact than those associated with distal EPSCs, leading to different spatial profiles (see Section 3.3.4, Figure 3.8) (Łęski et al. 2013). And how are different network activity patterns manifested in extracellular potentials? Mitzdorf's conclusions were about the amplitude of evoked and spontaneous CSDs, but the spectral content of such responses, or of more sustained activity, was not considered. The different timescales of distinct processes would lead to varying degrees of importance for different portions of the spectrum.

The next section outlines our basic approach toward building a detailed biophysical model of several possible contributors in order to test their relative importance in generating specific features of measured LFPs. This work illustrates how

the coordination of activity across a neural population and the fundamental timescales of the quantal processes at play can lead to different sources dominating the LFP in different frequency bands. However, our population model was tailored to the dorsal hippocampal area CA1, and some of our conclusions may not generalize well to other structures. To complement (or better motivate) such detailed models, more general approaches can prove extremely valuable (e.g., Lindén et al. 2011, Łęski et al. 2013). An additional worthwhile endeavor would be to develop parametric models of LFP/CSD contributions for generic sources, which could be used to construct LFPs within circuit or population models that are not biophysical representations in themselves. Such tools would facilitate the translation of network activity into a simulated LFP, providing additional ways to compare theory to experiment, greater flexibility in investigating the composition of extracellular recordings, and more efficient ways to investigate the role of extracellular fields as a feedback mechanism for coordinating network activity (Holt & Koch 1999, Weiss & Faber 2010, Anastassiou et al. 2011).

1.3 Our biophysical techniques for modeling LFPs

Control over the basic biophysical and geometrical properties of the neuronal constituents allows for broader study of field potentials in neuronal populations (see, for example, Lindén et al. 2011). Neurons in the brain, especially pyramidal cells, have a diverse array of ion channels distributed non-uniformly along their membranes that impart them with important but complicated dynamics. Some questions about neuronal function can be addressed by including only a subset of channels that are not perfectly

distributed within the cell. The strength and spatial distribution of transmembrane currents, however, is precisely what determines the extracellular potential generated by neuronal activity. Moreover, the membrane conductance profile changes as a function of synaptic or neuromodulator input, as well as various intracellular processes. Many of these subtleties can be safely ignored in certain situations. For example, (Gold et al. 2006) showed that the currents in the soma and axon hillock dominated the extracellular action potential (EAP) waveform (Mitzdorf 1985). The LFP, on the other hand, is thought to be comprised of mostly subthreshold currents distributed throughout the dendritic arbor, with this distribution playing a critical role in determining which signals are effectively integrated into the signal (Mitzdorf 1985, Lindén et al. 2011). The ways in which synaptically evoked currents are transformed and interact with each other is still poorly understood (London & Häusser 2005, Spruston 2008), and the precise distribution of active currents within dendrites may be highly variable (Gold et al. 2006). These gaps in our knowledge of dendritic electrophysiology present a challenge to a general theoretical investigation of LFP, but we can still ask specific questions and make qualitative judgments about the abilities of various cellular and network processes to reliably generate detectable extracellular signatures.

With this in mind, the basic methods we employed for modeling single neuron membrane currents, the resulting extracellular potential, and the summation of contributions from many cells are described in the next two sections.

1.3.1 Extracellular potentials from simulated neurons

Detailed biophysical models of individual neurons with elaborate morphologies are increasingly common (Koch & Segev 1998, Markram 2012, Gerstner et al. 2012). To facilitate rapid development and implementation of these models, specialized software packages [e.g., NEURON (Carnevale & Hines 2006) and GENESIS (Bower & Beeman 2003)] have been developed to simulate electrical and ionic activity within single and networked neurons. For compartmental model simulations (Figure 1.1, from Nicholson 1973), the software employs numerical integration algorithms to solve the cable equation, with additional current injections and conductance changes at each cable element determined by systems of kinetic equations modeling various ion channels. Because of the large existing database of detailed neuron models available for NEURON (Hines et al. 2004), as well as extensive experience using this simulator in the Koch laboratory, we chose to adopt this environment for single cell transmembrane current simulations.

NEURON simulates neuronal activity by taking a user-specified neuron morphology, breaking into isopotential compartments, which are connected to each other and to the extracellular space via intracellular and transmembrane resistance and capacitance, as well as active conductances, and numerically integrating the resulting system of differential equations in order to track the time course of voltages and currents for each compartment. The number of compartments must be high enough, and the integration time step short enough, such that the dependent variables converge to a stable unique solution for given initial conditions. For the choice of compartment number, a good rule of thumb is to begin with the “d-lambda rule” (Carnevale & Hines 2006 pp.

122-126), which uses a specified fraction of the AC length constant for each branch or cable section. NEURON allows for a variable time step using the CVODE method (Cohen & Hindmarsh 1996), which dynamically adjusts the time step in order to keep the estimated local error below a user-specified maximum allowable absolute error. This often works well to speed up simulations, but we used a fixed time step so that multiple simulations (e.g., different trials, input configurations, and model cells) could be flexibly combined into a composite LFP without the need to resample the results.

In addition to geometrical specifications and computational parameters, the following attributes must be specified for a neuron model: (1) passive circuit properties (e.g., axial intracellular resistance, membrane resistance and capacitance); (2) active conductance dynamics for ion-specific and non-specific channels (e.g., Hodgin-Huxley model of Na^+ and K^+ channels, Ca^{2+}-dependent K^+ channels, etc.); (3) channel density in each compartment for distributed mechanisms, or compartment locations for point processes (synapses, current injection, etc.); (4) Ca^{2+} diffusion and buffering mechanisms; and (5) initial conditions. Once all of the relevant morphological, biophysical, and computational parameters are set, the simulation runs with the variables of interest saved, and transformations on their values performed, as specified by the user. The precise neuron geometry does not matter for the single cell simulation (assuming the extracellular space is treated as an isopotential reference), because the neuron is modeled as a collections of circuit elements. The geometry comes into play once we use the single-cell simulation results to calculate the resulting extracellular potentials.

Carl Gold and Christof Koch, along with collaborators in the labs of Gyorgy Buzsaki and Kevan Martin, used compartmental models to investigate details of the the transformation from intracellular to extracellular currents, focusing primarily on the generation of EAPs (Gold 2007). We used one version of the model (D151, parameter set A) to recreate EAPs of a pyramidal cell from the CA1 region of the rat hippocampus (Gold et al. 2006, 2007). The reconstructed neuron had the following basic dimensions: soma surface area = 559 μm^2; total dendrite length = 10,155 μm; vertical (stratum oriens to stratum lacunosum-moleculare) dendritic arbor height = 677 μm. In addition to the passive properties of the membrane (membrane resistance R_m = 15 kΩ cm^2, membrane capacitance C_m = 1 μF cm^2, intracellular resistivity R_i = 70 Ω cm), the model incorporated 12 types of ion channels, including Na^+, K^+, Ca^{2+}, Ca^{2+}-dependent K^+, and dendritic hyperpolarization-activated I_h currents. The model had a resting membrane potential at the soma of -65 mV. We used 512 compartments and a 0.01 ms time step for our simulations, which yielded stable and consistent transmembrane currents and satisfied charge conservation requirements.

To excite the neurons, we inserted conductance-based synapses into individual compartments scattered throughout the cell. Each synapse was modeled as a time-varying conductance in series with a reversal potential $E_{rev,syn}$, based on the primary ionic transporter for the synapse type (e.g., Na^+ or Cl^- for AMPA and $GABA_A$ synapses, respectively). The time course of the conductance g after activation consisted of a fast rise and slower decay, described by a double exponential formula: $g(t) = G_0 [\exp(-t/\tau_{decay}) - \exp(-t/\tau_{rise})]$. The current I_{syn} passing into the cell through this synaptic conductance at

time t is then given by $I_{syn}(t) = g(t)*(V_m(t) - E_{rev,syn})$, where V_m is the membrane potential of the compartment at the synapse location. Measurement of the true synaptic current in neurons is notoriously difficult because of the separation between a synapse and the patch pipette, the effect of a cell's input impedance (which is variable), and the fact that the circuit has been modified by the patch, so we tested a range of values based on various estimates for the decay time constant. The rise time is much faster and, consequently, variation of its value plays a smaller role in the transformation from a train of synaptic activation times to the time course of the conductance variation, so we fixed its value at 0.1 ms.

The membrane potential throughout the cell changes in response to this additional synaptic conductance, and the current crossing the membrane at each compartment via resistive, capacitive, and synaptic currents can be calculated for each step in the simulation. One could treat the transmembrane current at each compartment as a point source of current in the extracellular space. Relative to the potential infinitely far from a point source at r_0, the electric potential at a point r would then given by $\Phi(r,t) = \rho I(r_0,t)/4\pi(r-r_0)$, where ρ is the resistivity of the extracellular space. We used a slightly more accurate approximation and treated each compartment as a line source (see Section 3.2.1). We used a real, uniform, scalar value for the resistivity of extracellular space, i.e., we approximated the extracellular milieu as a purely resistive, homogeneous, and isotropic volume conductor. A more detailed model would incorporate inhomogeneity across layers, anisotropy created by fiber orientations, and imaginary components of the impedance. Our assumption of ohmic behavior, however, appears to be adequate for the

typical spectral range of LFP analysis (Plonsey & Heppner 1967, Logothetis et al. 2007, Łęski et al. 2013), but its accuracy is still a matter of debate (e.g., Bédard et al. 2010).

1.3.2 From compartments to cells to populations

The contributions to the extracellular potential from each compartment in each cell sum linearly to give the total extracellular potential in the model population (see Figure 3.1). To simulate extracellular potentials emanating from membrane currents in pyramidal cells of the dorsal CA1 area of hippocampus, we chose soma locations randomly from a cylindrical disk (excluding a small region near the recording site), with the disk thickness chosen to capture the extent of the cell body layer. We included cells 15-500 μm from the recording site and assessed the successive contributions of cells within different distance ranges, though if correlations in membrane currents continue indefinitely with distance, the total potential does not converge to a finite value (Lindén et al. 2011). The extent of the population contributing to the extracellular signal is therefore determined to a large degree by the extent of correlated membrane currents and the temporal delays in these correlated fluctuations, as well as the extent of commonly oriented current dipoles. This principle likely explains the large disparity in estimated regions of integration for cortical LFP signals, from 200-300 μm to 2-3 mm (Juergens et al. 1999, Katzner et al. 2009).

On a microscopic level, each synaptic event, and even each action potential, will produce a unique pattern of currents and potentials within and around the cell. For distances less than ~100 μm, the extracellular potential from a synaptic input decays in an

approximately monopolar fashion (i.e., as 1/*r*), because this is not yet in the far-field regime where the membrane currents can be approximated as compact dipoles (Lindén et al. 2010). With excitatory synaptic current decay time constants on the order of milliseconds (Hestrin et al. 1990) and several hundred synaptic transmission events occurring each millisecond in this distance range[1], a volume-averaged current source density could be appropriately used to calculate the resulting LFP power, similar to the the framework used by Rall and Shepherd (1968) or Nicholson and Llinás (1971). In practice, however, calculating the appropriate transformation for a given synapse distribution and activation rate to the approximate time/frequency-dependent CSD distribution would be more cumbersome than simply running brute force simulations, an option which is readily available with today's computers. We instead used "average" membrane current distributions for stereotypical activation patterns (see Figure 3.8) and, in the case of synaptic currents, population averaging techniques to speed up calculations (see Section 3.2.3).

1.4 Comparing theory and experiment

Careful consideration and modeling of how the known neural elements could generate experimentally recorded potentials has led to hypotheses and subsequent experimental confirmation of several interesting features of their physiology and connections, such as the presence of dendro-dendritic synapses in the Rabbit olfactory bulb (Rall et al. 1966, Rall & Shepherd 1968) and active dendritic spike generation in

[1] [3×10^5 cells/mm^3 (Boss et al., 1987)] * [0.04 mm stratum pyramidale thickness (Andersen et al., 2007)] * [0.01π mm^2 disk radius] * [3×10^4 synapses/cell (Megías et al., 2001)] * [0.2 vesicle release (Murthy et al., 1997)] *[0.2 to 0.5 Hz firing rate (Mizuseki et al., 2013)]

cerebellar Purkinje cells (Llinás & Nicholson 1971, Nicholson & Llinás 1971). The latter case, however, drew considerable controversy (Calvin 1969, Hellerstein 1969), and for good reason. The models of Nicholson et al. were relatively simple by today's standards, but there were still multiple qualitatively distinct regimes in which the same set of free parameters could be tuned in different ways to give similar results. As Calvin (1969) stressed, finding one set of parameters that yields theoretical results in agreement with experiments does not prove it is the unique and accurate solution, and the parameter values are often justified in a biased (or even circular) manner.

It is important to independently validate the components of a model, and so we sought to avoid inappropriate comparisons between our theoretical results and previous reports from experimental recordings. The pyramidal cell model we used was developed and tuned using a data set that was independent from the recordings we used for comparison, and we felt confident it could be reasonably employed for quantitative estimates of extracellular signatures of spiking neuron populations. The basket cell model was not developed with this purpose in mind, however, but its EAP characteristics were within the proper ranges (Henze et al. 2000, Bartho et al. 2004), exhibiting a larger but narrower EAP compared to the pyramidal cell (Section 3.3.3, Figure 3.6).

Estimating synaptic contributions from these models, however, would be a tenuous extrapolation. The Gold et al. (2006, 2007) model was not developed to accurately emulate synaptic currents at all, the Nörenberg et al. (2010) and Hu et al. (2010) model was developed to test only specific characteristics of synaptic integration, and no compartmental model has yet been shown to precisely capture both intracellular

and extracellular signatures of synaptic input. Even if we had a reliable way to emulate the spatiotemporal profile of membrane current in response to a unitary synapse, and supposing the model would accurately adapt this response for different depolarization and conductance states during ongoing synaptic barrages, the number, rate, and spatiotemporal activation profile of synapses from different presynaptic populations is not well specified at present. We would still be left with a high-dimensional space of free parameters.

Luckily, a way to obtain quantitative estimates of the LFP contributions of some subpopulations of synapses onto CA1 pyramidal cells was available, with the parameter space being similarly constrained and reasonably well specified by experimental results. We developed a phenomenological model of the 'unitary field potentials' (uFields) generated by the postsynaptic currents evoked by single inhibitory interneuron spikes (Figure 1.2, compiled from Glickfeld et al. 2009), based on measurements of these uFields in CA1 and CA3 hippocampal slices (Glickfeld et al. 2009, Bazelot et al. 2010). By specifying only the temporal firing rate functions for the CA1 pyramidal and basket cell populations and their spatial arrangements, we could then compare the contributions of each set of neurons to extracellular potentials in CA1 to each other and to in vivo recordings. These simulations, the results and comparisons to experiments, and the implications are presented in Chapter 4.

1.5 Figures for Chapter 1

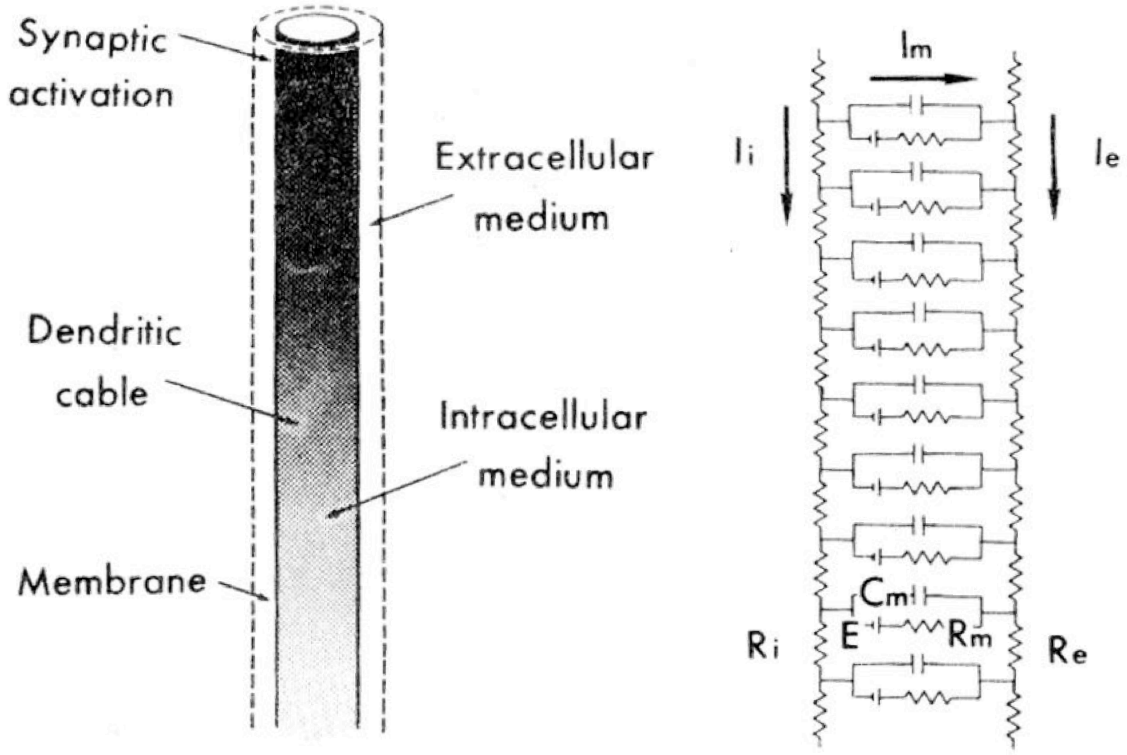

Figure 1.1. An illustration of a cable model of a neural fiber. At neurophysiological timescales, the Kirchoff's laws hold. In the determination of intracellular and transmembrane current flow, the extracellular space can be considered as isopotential. Current flow through the membrane via ion channels is modeled by current injection and time-dependent conductances distributed in the membrane. This allows the neural activity to be simulated, and the results used to calculate extracellular variation of the potential. For our purposes, we did not use this result to (iteratively) correct the intracellular calculation [but see Anastassiou et al. (2010, 2011)]. From Nicholson (1973).

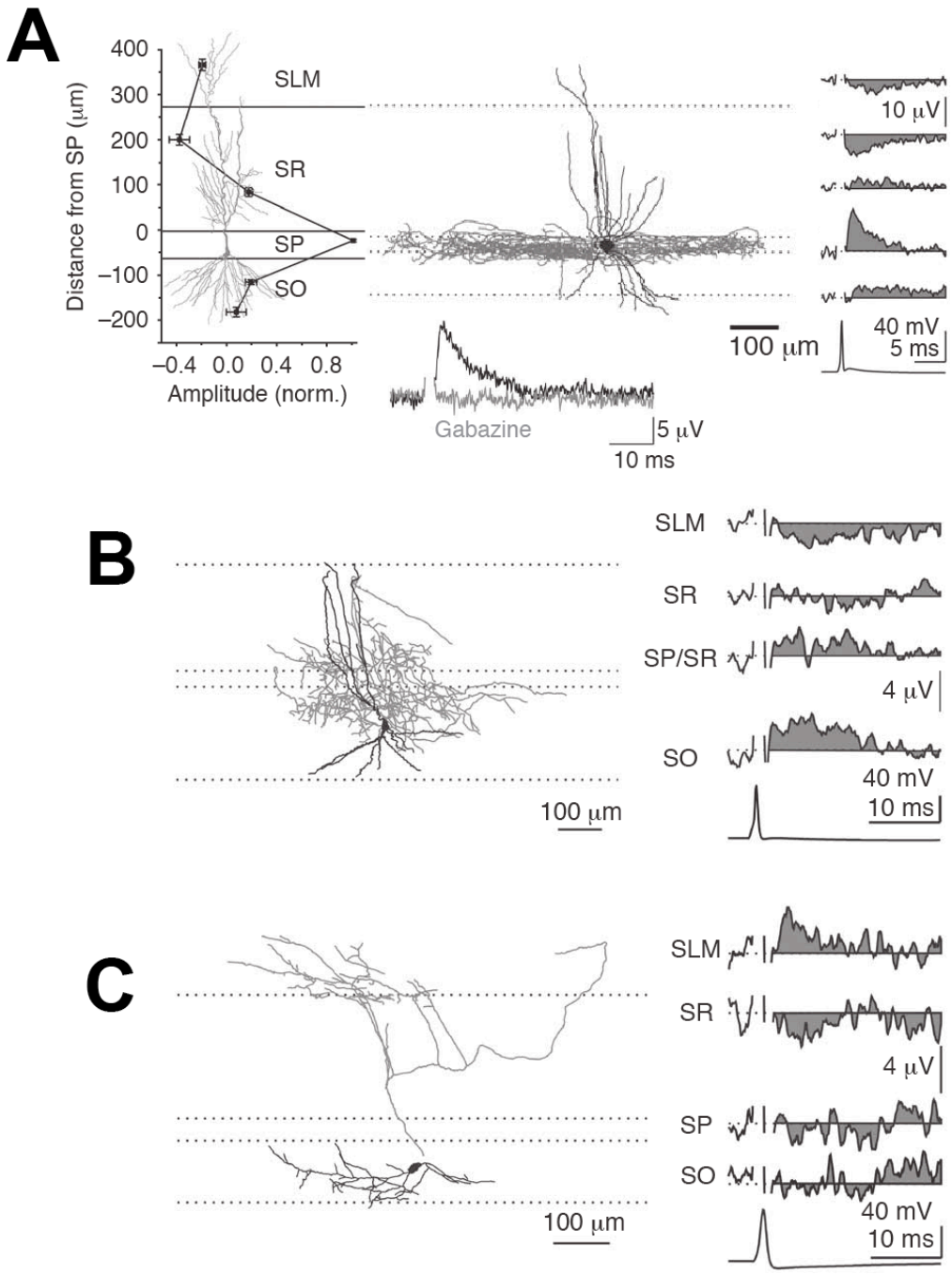

Figure 1.2. In vitro recordings of unitary inhibitory field potentials (uFields), i.e., the LFP contribution from single spikes of three different types of CA1 interneurons. ***A,*** Profile of uField of a perisomatically-targeting basket cell. *Left*, the average peak amplitude and its sign. *Right*, example traces after single spikes, recorded at different

depths relative to stratum pyramidale. Application of gabazine (*bottom*) abolished the uField. ***B, C*** Same as *A* for a bistratified cell (*B*) and a tuft-targeting oriens-lacunosum-moleculare (OLM) cell (*C*). Modified from Glickfeld et al. (2009).

2. Extracellular potentials in the hippocampus

2.1 Hippocampal anatomy and function

Early neuroanatomists, as well as anyone who begins to slice and study mammalian brains, could not help but be drawn to the hippocampus. It is one of the few brain structures with features of its anatomy clearly visible to the naked eye, and this clear organization also makes it attractive for neurophysiological studies. It has many of the same cellular components of the neocortex, but fewer principal cell layers, most of which are compact and comparatively uniform. The intrinsic and extrinsic synaptic pathways are also well organized, again leading to robust spontaneous and evoked activity during recording and stimulation. Because these inputs are layered along well-aligned dendrites and are activated in temporally coordinated patterns during certain behavioral states, the LFPs in the hippocampus can be large and distinctive. Finally, the hippocampus plays a crucial role in learning and memory, and many prominent features of its network activity are clearly related to these processes. For all of these reasons, it has been the subject of intensive investigation for many decades, but many aspects of its function continue to confound researchers.

Part of the difficulty linking its known roles in rodents to those found in humans may be due to historical and experimental accidents: the dorsal portion in rodents is relatively easy to access electrophysiologically, compared to the ventral portion, but the homologous domain to the ventral rodent hippocampus (which is more involved in emotional and contextual memory) appears to be enlarged and perhaps more important for primate cognition. There are conceptual similarities between navigation in physical

space and navigation in the broader mental space of episodic memory, however, so the differences in hippocampal function between species may be smaller than they seem. Even in rats, conflicting results still arise regarding the network dynamics of the dorsal hippocampus, and some of this confusion may be due to incomplete and/or mistaken assumptions regarding the physiological correlates of some of its electrical signals.

For a comprehensive overview of hippocampal anatomy and physiology, refer to *The Hippocampus Book* by Andersen et al. (2007). On a gross scale, the rat hippocampal formation is connected as a loop of 3-5 synapses, depending on which connections one counts (Figure 2.1). The primary excitatory pathway from the rest of the brain to the hippocampus proper (the dentate gyrus, areas CA1-CA3, and the subiculum) is through the entorhinal cortex (EC), which sends projections from its superficial layers to the dentate gyrus (DG), areas CA1-CA3, and the subiculum. Following Andersen et al. (2007), the "hippocampal formation" term in this thesis refers to the EC, DG, CA1-CA3, and the subiculum. Additional input arrives from various neocortical and subcortical regions, but the precise roles of these connections has yet to be worked out, and these inputs generate smaller current dipoles than the intrahippocampal afferents. Reciprocal connections to the medial septal nucleus and the diagonal band of Broca are important in coordinating and maintaining a circuit-wide, coherent, theta rhythm (described below). At the coarsest level, however, the circuit can be described as follows. The EC acts as the main conduit for signals coming to and from the hippocampus. Projection neurons in layer 2 of EC (EC2) run send axons through the perforant path to the DG and CA3. EC layer 3 (EC3) neurons project through the temporoammonic pathway (also called

perforant path) to CA1. The mossy fibers of the DG project to CA3, and CA3 sends axons through the Schaffer collateral pathway to CA1 and subiculum. The pyramidal neurons in CA1 project forward to both the subiculum, and to the deep layers of EC (EC5). The subiculum sends its efferents to the pre- and parasubiculum and deep EC. At no point in this loop are there substantial back-projections, except for some projections from CA3c to DG, and only within EC and CA3 are major recurrent excitatory connections present. An additional, parallel circuit involving CA2 has recently been described: CA2 integrates EC2 and CA3 input and projects to deep CA1 pyramidal cells (Chevaleyre & Siegelbaum 2010, Kohara et al. 2013).

Area CA1, which is located most dorsally at the septal pole of the hippocampus and is the easiest to reach and recognize with electrical probes, integrates two major inputs: the Schaffer collateral input from CA3 onto basal dendrites in stratum oriens and oblique apical dendrites in stratum radiatum, and the perforant path input from EC3 impinging on the distal apical tuft in stratum lacunosum-moleculare. CA1 has few recurrent connections between its pyramidal cells, but a rich array of inhibitory interneurons that receive both feedforward and feedback (from CA1 pyramidal neurons and other interneurons) input. The various interneuron subtypes have a diverse set of physiological properties and dynamics, receive input from distinct sources, and target specific dendritic domains of pyramidal cells and other interneurons (see Figure 1.2) (Freund & Buzsáki 1996, Klausberger & Somogyi 2008, Bezaire & Soltesz 2013). This diversity and specificity has led to numerous hypotheses about their specialized

functional roles in local network and dendritic computation (Klausberger & Somogyi 2008, Lovett-Barron et al. 2012, Royer et al. 2012, Lapray et al. 2012, Leão et al. 2012).

2.2 Hippocampal LFPs

Much of our current knowledge of hippocampal physiology has come from electrical recordings in the rodent hippocampus. Event-triggered averaging and multisite simultaneous recordings have revealed various spatiotemporal features that have been linked to various anatomical and physiological characteristics, several of which are described below. Initial recordings were done using single-site wires or wire bundles, but the current standard is to use either tetrode drive arrays (Nguyen et al. 2009) or silicon-based electrode arrays (Vandecasteele et al. 2012). Tetrode multi-drives have the advantage that each tetrode can be independently positioned into the pyramidal layer for single unit detection and spike sorting (Quian Quiroga 2007). Silicon probes have a fixed electrode geometry, which allows for the analysis of spatial structure in LFPs and the application of CSD analysis, while maintaining a high density of recording sites for unit clustering. All of the recordings described in this thesis were performed using silicon probes implanted chronically in rats (Montgomery & Buzsàki 2007, Diba & Buzsáki 2007, Mizuseki et al. 2009, Patel et al. 2012, Berényi et al. 2014). With the advent and continued development of high-speed optical reporters (Chemla & Chavane 2010, Chen et al. 2013), it is now feasible to record activity rhythms at LFP frequency scales in many more cells simultaneously, with the participating neurons being identifiable and chronically observable over long periods of time.

The following three sections describe the most commonly analyzed LFP patterns in the rodent hippocampus, as well as background on what is known about the underlying physiology. Chapters 3-5 describe our work to further dissect, understand, and model their generation in the rat hippocampus.

2.2.1 Theta oscillations

One of the most distinctive and robust oscillations in the mammalian brain, with a clear correspondence to behavior, is the 5-10 Hz theta rhythm of the rodent hippocampus [see Buzsáki (2002) for a comprehensive review]. The LFP signature is instantly recognizable (Figure 2.2), and theta power is strong and reliable enough to be used as an approximate surrogate for tracking different classes of behavior. When a rat is awake, the hippocampus becomes engaged in theta oscillations during times of active exploration/ navigation (especially during walking/running, but also during rearing) (Vanderwolf 1969). This oscillation entrains nearly all of the neurons in the hippocampus (especially the septal and intermediate portions; Patel et al. 2012) and the entorhinal cortex (especially the medial portion; Deshmukh et al. 2010), with each region becoming most active at a different phase of the cycle, and the different cell types within a region also prefer different phases (Mizuseki et al. 2009). Theta oscillations also emerge intermittently during sleep, corresponding to epochs of rapid eye movement (REM) sleep. Because the brain-wide LFPs and network activity look so similar to those during waking behavior, this sleep stage has also been referred to as paradoxical sleep.

One of the striking features of hippocampal theta is how well coordinated it is across the entire hippocampal circuit. Each area/layer of the dorsal hippocampus is coherent with the others and with the entorhinal cortex (Mitchell & Ranck 1980, Buzsáki et al. 1986, Alonso & García-Austt 1987, Montgomery et al. 2008; but see Kocsis et al. 1999), both within and across hemispheres (Kocsis et al. 1994). It has been well established that theta in the hippocampal formation is coordinated by the medial septum and the diagonal band of Broca (MSDBB), theta oscillations can be generated in isolated portions of the circuit, owing to both network and cellular resonance at theta frequencies (Konopacki et al. 1987, Leung & Yu 1998, Buzsáki 2002, Goutagny et al. 2009, Stark et al. 2013). Multiple mechanisms are therefore at play, which can be dissociated with pharmacology or deafferentation (Kramis et al. 1975, Soltesz & Deschênes 1993, Ylinen et al. 1995a). Indeed, the hippocampal theta LFP in the behaving animal is composed of multiple interacting theta dipoles (Leung 1984, Montgomery et al. 2008). Understanding these interactions will almost certainly be necessary in order to fully explain the intricate and state-dependent coordination of spiking throughout the network during theta oscillations (O'Keefe & Recce 1993, Poe et al. 2000, Mizuseki et al. 2009, Lever et al. 2010, Mizuseki et al. 2011).

Though the theta rhythm is widely coordinated in the hippocampal-entorhinal-MSDBB system, the ways in which hippocampal theta deviates from a monolithic signal likely illustrate functional separations within the structure. In the longitudinal direction, i.e., along the septotemporal axis of the hippocampus, theta phase delays are coordinated such that the neural activity can be described as a traveling wave from the septal pole

towards the temporal pole (Lubenov & Siapas 2009). The wave, however, does not propagate consistently along the entire extent of this axis. Rather, the septal and intermediate thirds are well coordinated, whereas the temporal third operates more independently (Patel et al. 2012). This separation is consistent with anatomical, genetic, functional, and other physiological differences between the septal and temporal regions of the hippocampus (Moser et al. 1993, Jung et al. 1994, Hock & Bunsey 1998, Andersen et al. 2007, Fanselow & Dong 2010, Royer et al. 2010, Dougherty et al. 2012, Schmidt et al. 2013, Patel et al. 2013), and may also help to explain differences between theories of hippocampal function in rodents and humans (O'Keefe & Nadel 1978, Squire 1992).

2.2.2 The sharp wave-ripple complex

In addition to theta oscillations, the other most distinctive electrophysiological phenomenon in the hippocampus is the sharp wave-ripple (SWR) complex (Figure 2.3). It is most recognizable within area CA1, though the effects reverberate through the rest of the circuit. One of the characteristics of the theta state is an elevated inhibitory tone, and upon release from this inhibition (e.g., when the rat stops running, or following a transition from a DOWN to UP state during slow-wave sleep), the CA3 network, which has many recurrent excitatory connections, generates large bursts of activity (Bragin et al. 1995, Sullivan et al. 2011, Viney et al. 2013). The resulting excitatory impulse to CA1, the “sharp wave”, induces a 140-200 Hz oscillation, the “ripple”, within its pyramidal-interneuron network (Buzsáki et al. 1992, Ylinen et al. 1995b).

The “sharp wave” in the CA1 LFP reflects a large, synchronous volley of excitation coming from CA3 through the Schaffer collateral pathway. Though the burst of excitation is thought to originate in the more densely connected CA3a and CA3b subregions, the CA3c population displays a greater increase in firing, and these pyramidal neurons project predominantly to stratum radiatum in CA1. This explains the large dendritic current sink generating the large negative wave in radiatum and a smaller positive wave in stratum pyramidale. The stratum radiatum LFP also exhibits a slower positive phase following the sharp wave, which is paired with hyperpolarization of the pyramidal cell somata (whether or not they spike), and so it may represent $GABA_B$-mediated inhibitory currents or depolarization-activated K^+ channels in the pyramidal cells.

The fast ripple is not coherent with activity in CA3, but is widely coordinated within CA1 (Figure 2.3; Chrobak & Buzsáki 1996, Csicsvari et al. 2000, Patel et al. 2013). The ripple power is strongest in the middle of stratum pyramidale (Mizuseki et al. 2011), and so it serves as an important physiological landmark during in vivo recording. The mechanisms of the precise temporal synchrony in the CA1 network during ripples are still debated. Much of the available evidence indicates that the basket cell population in CA1 is sufficient to coordinate spiking within the cell populations (Brunel & Wang 2003, Buhl et al. 2003, Buhl & Buzsáki 2005, Taxidis et al. 2011), but some studies have indicated that gap junctions between pyramidal cell axons, or even the sparse excitatory synaptic connections between pyramidal cells, also play an important role (Draguhn et al. 1998, Traub & Bibbig 2000, Maier et al. 2011). Regardless of the mechanisms of

coordination, the other aspect of any LFP signal we wish to understand is the biophysical origin of the currents that generate it. This is the question we chose to address using a modeling approach that allowed us to simulate extracellular potentials from specified population activity that was designed to mimic the measured statistics of spiking during SWRs.

During SWRs, as many as 5% of the clustered putative pyramidal neurons fire during a large 5-7 ms ripple wave, representing a 5-6 fold increase in firing rate from the baseline average. These units, furthermore, show an increase in synchrony beyond that expected for shared firing rate modulation (Csicsvari et al. 2000), and the spikes are strongly modulated by the phase of the ripple oscillation (Buzsáki et al. 1992, Ylinen et al. 1995b, Csicsvari et al. 1999a). Overall, interneurons also exhibit large increases in firing rate, though not as dramatic a change as the pyramidal population, as well as phase-locked spikes, but these changes in activity are cell-type specific, with basket cells and bistratified cells showing the greatest involvement (Klausberger et al. 2003, 2004, Varga et al. 2012, Forro et al. 2013).

Because of the immense increase in firing and and the high degree of synchrony during SWRs, they are suited to engage synaptic plasticity mechanisms in the participating neurons (Hebb 1949, Bliss & Lomo 1973, Bi & Poo 2001). SWRs were therefore hypothesized to play a role in memory consolidation during sleep (Buzsáki 1986, 1989). Since this role was proposed, several key features enabling it have been found: (1) SWR-related increases in firing propagate out of the hippocampus to its neocortical targets (Chrobak & Buzsáki 1996, Siapas & Wilson 1998, Logothetis et al.

2012); (2) the SWR participants and their temporal firing order reflect previous experience (Wilson & McNaughton 1994, Skaggs & McNaughton 1996, Ji & Wilson 2007, Peyrache et al. 2009, Davidson et al. 2009); (3) the disruption of SWRs during sleep following training impairs learning (Girardeau et al. 2009). SWRs during the awake state also appear to be important for learning, memory recall, working memory, and route planning (Carr et al. 2011, Jadhav et al. 2012, Pfeiffer & Foster 2013). Because of their apparent significance in learning, memory, and neural dynamics, an important goal is to understand what physiological processes SWRs represent.

The ripple in the stratum pyramidale LFP was previously thought to reflect mostly perisomatic IPSCs (Ylinen et al. 1995b), with some EAPs riding on top of this synaptically generated signal (Buzsáki 1986). The SWR LFP seemed then, to be a relatively simple and well-understood test case for a model of hippocampal LFP generation. Chapter 3 explains how our model in fact showed that the population spiking during SWRs in fact generates much more of the ripple power than we had expected, and may play a role in lower-frequency oscillations, as well. Furthermore, it brings us back to the question of the role of inhibitory synapses in enforcing such widespread synchronous firing, which has yet to be satisfactorily answered.

2.2.3 Gamma oscillations

30-90 Hz gamma oscillations have been widely studied throughout many cortical regions, having been implicated in sensory processing, attention, working memory, and learning (Singer & Gray 1995, Engel et al. 2001, Fries 2009, Wang 2010, Colgin &

Moser 2010, Lisman & Jensen 2013). Gamma oscillations usually reflect local activity (Katzner et al. 2009), but coherent gamma between spatially separated regions is thought to be important for communication and integration of neural codes (Engel et al. 2001, Fries 2009). Gamma oscillations nearly always involve GABAergic interneurons (Klausberger & Somogyi 2008), especially fast-spiking, perisomatically targeting ones, such as parvalbumin-expressing (PV+) basket cells (Buzsáki & Wang 2012).

In addition to the essential role of inhibitory interneurons in coordinating gamma oscillations, there is also evidence that inhibitory currents generate much of the gamma LFP signal, at least in the portions of the circuit (e.g., DG and CA1) with few recurrent excitatory connections. During carbachol-induced gamma *in vitro*, the application of gabazine into CA1 to block local $GABA_A$ synaptic transmission abolished CA1 gamma LFPs while leaving the CA3 gamma oscillation intact (Zemankovics et al. 2013). Similarly, whole-cell patch clamp recordings of DG granule cells *in vivo* showed inhibitory currents coherent with gamma LFPs, but very little gamma coherence between excitatory currents and LFPs (Pernía-Andrade & Jonas 2013). (Theta LFPs, on the other hand, were coherent with excitation, but weakly coherent with inhibition. This latter result likely does not also hold in CA1, where interneurons are highly theta-modulated (Fox & Ranck 1975).)

In the hippocampal formation, the typical amplitudes and frequencies of gamma oscillations vary from region to region, and independent gamma rhythms can arise out of the EC and CA3 (Bragin et al. 1995, Chrobak & Buzsáki 1998, Fisahn et al. 1998, Csicsvari et al. 2003). Even within a single region, events at different gamma frequencies

can occur (Csicsvari et al. 1999b, Middleton et al. 2008). The frequency differences probably result from a combination of differences in connectivity (e.g., strong recurrent connectivity in CA3; Li et al. 1994), the modulatory state and excitation-inhibition balance (Atallah & Scanziani 2009), the timescales of integration in layer 2/3 pyramidal and stellate cells and CA3 pyramidal cells (Jones 1994, Larkum et al. 2007, Pastoll et al. 2012, Makara & Magee 2013), and intrinsic cellular resonances (Traub et al. 1997, Brunel & Wang 2003, Tiesinga & Sejnowski 2009, Mann & Mody 2010, Broicher et al. 2012, Moca et al. 2013). During theta oscillations, CA3 pyramidal cells receive strong inhibition from GABAergic interneurons that are targeted by dentate granule cells (Acsády et al. 1998, Mori et al. 2007), but gamma oscillations emerge much more strongly and regularly from CA3 when this feedforward inhibition is removed (Bragin et al. 1995).

With the CA1 network integrating input from CA3 and EC3, as well as its own interneuron network, it is no wonder that its gamma-band spectral profile is more heterogeneous than those in its afferent regions (Chapter 4; Colgin et al. 2009, Belluscio et al. 2012).

2.2.4 Theta-gamma coupling

The hippocampal-entorhinal gamma rhythms do display temporal organization, and are coupled to the theta cycle. The most obvious form of this coupling cross-frequency coupling (CFC) is the modulation of gamma amplitude by theta phase (Bragin et al. 1995, Chrobak & Buzsáki 1998, Colgin et al. 2009, Tort et al. 2009, Belluscio et al.

2012, Pernía-Andrade & Jonas 2013). The dominant gamma frequency in the LFP also varies with theta phase (Colgin et al. 2009, Belluscio et al. 2012), which we could call phase-frequency coupling. Furthermore, phase-phase coupling has also been demonstrated (Belluscio et al. 2012), which may be related to the frequency-frequency coupling reported by (Bragin et al. 1995). Phase-amplitude coupling between theta and gamma, at least, has been linked to learning-related performance increases (Tort et al. 2009), and similar CFC phenomena have been reported in the human hippocampus (Mormann et al. 2005, Canolty et al. 2006, Axmacher et al. 2010). Indeed, theta-gamma coupling, and CFC in general, appears to be fundamental to hippocampal function and neural processing throughout the brain, as these rhythms likely serve complementary roles in organizing cell assembly sequences and mediating synaptic plasticity (Canolty & Knight 2010, Buzsáki 2010, Lisman & Jensen 2013). We will return to the topic in depth in Chapter 4 and the Conclusion.

2.3 Figures for Chapter 2

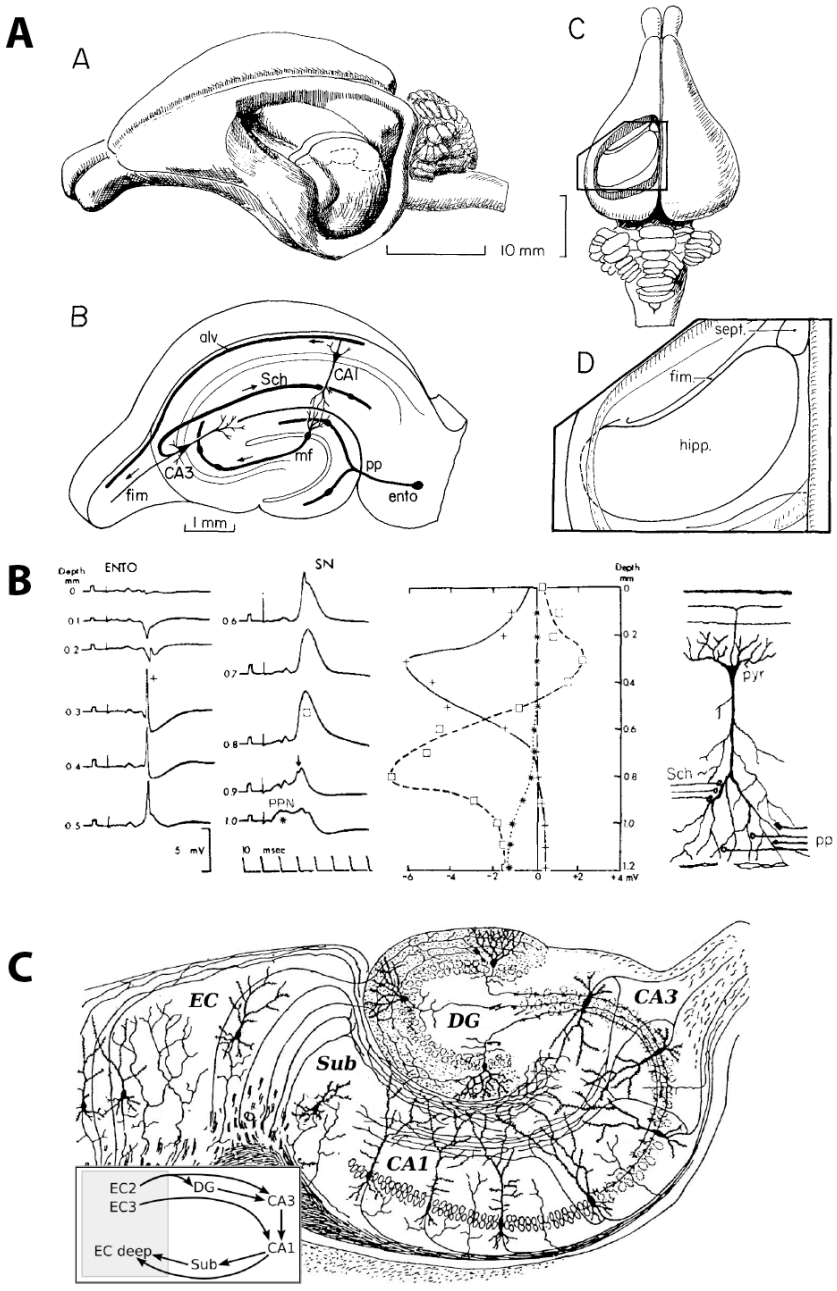

Figure 2.1. ***A,*** Anatomical layout of the rodent hippocampus. Sub-panel B shoes the laminar profile of the dentate gyrus (DG) and hippocampal CA1 and CA3 in a transverse plane of the hippocampus (marked in sub-panel A). The longitudinal axis is typically referred to by the septal-to-temporal (septum labeled in sub-panel D) orientation of the

hippocampus, which is medial-to-lateral in sub-panel C, and dorsal-to-ventral in sub-panel A. From Andersen et al. (1971). ***B,*** Extracellular population spike and synaptic current responses to antidromic (crosses), Schaffer collateral (squares), and perforant path (stars) stimulation, relative to depth in CA1. From Andersen et al. (1966). ***C,*** Modified drawing by Ramon y Cajal (1911). From the Hippocampus article on Wikipedia.

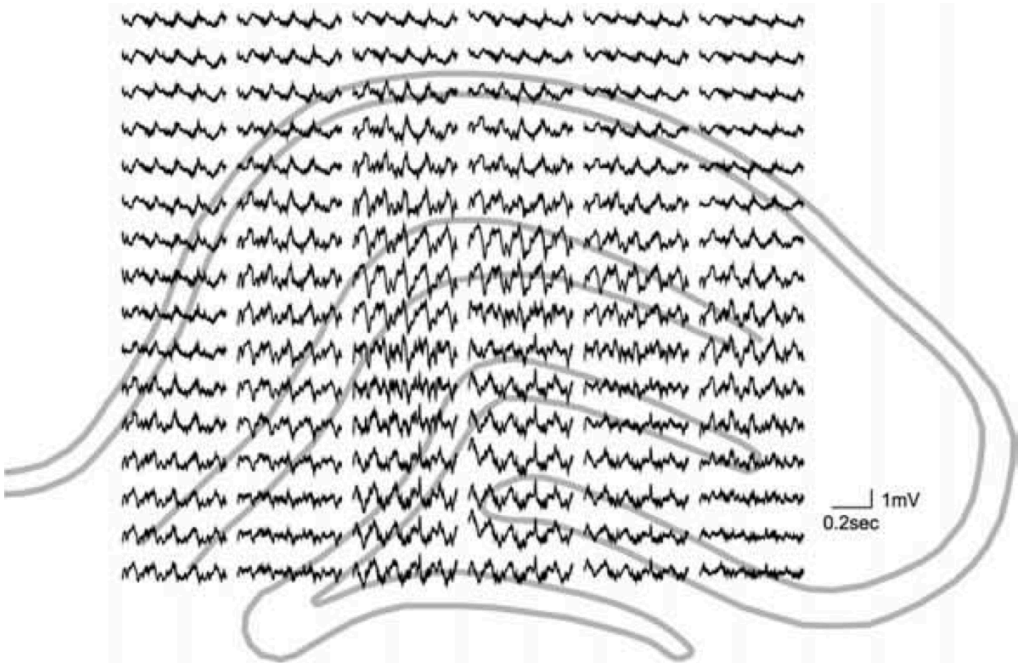

Figure 2.2. The coherent pattern of theta LFPs throughout a transverse plane (see Figure 2.1) in the dorsal hippocampus of a rat during running behavior. From Montgomery et al. (2009).

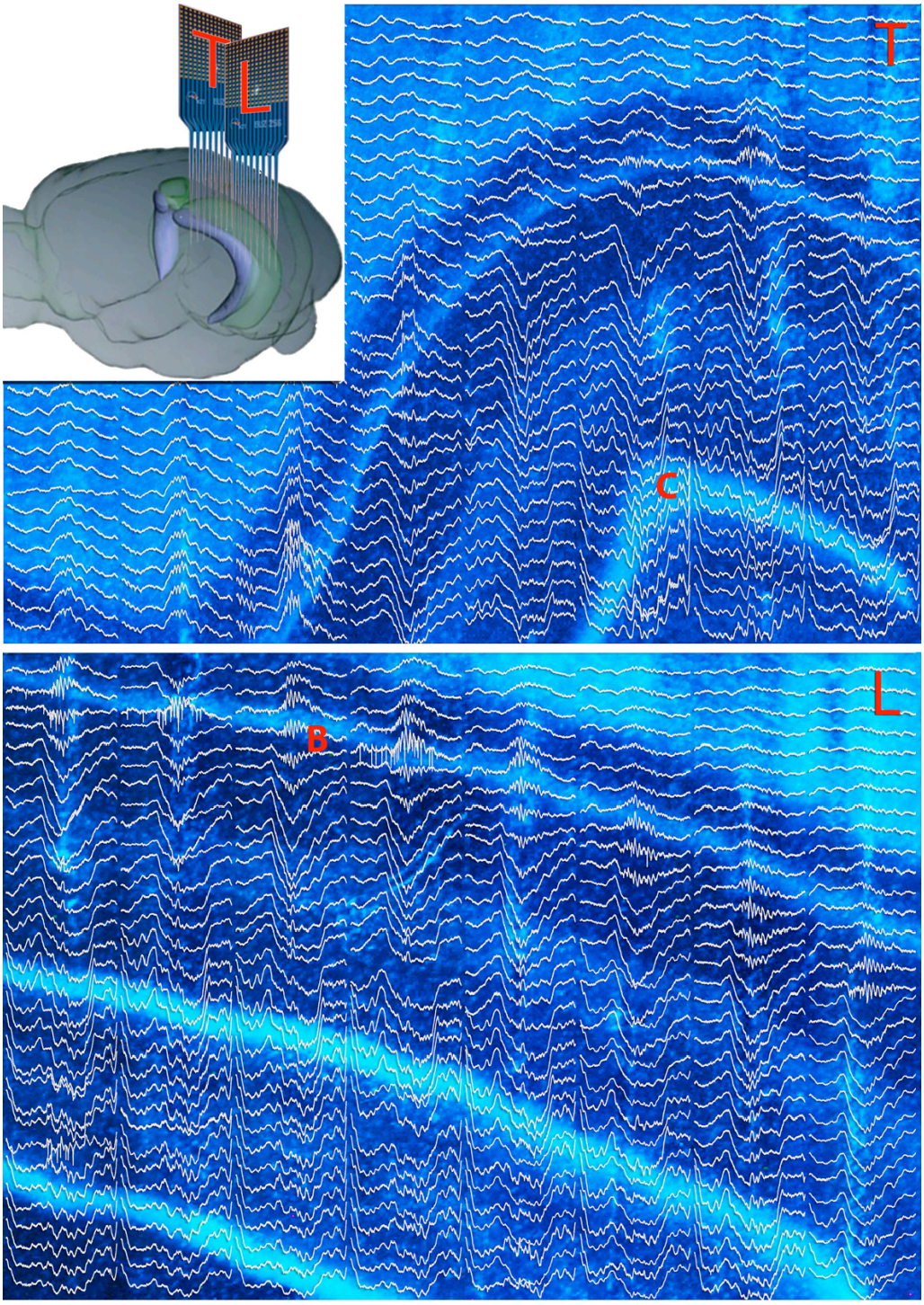

Figure 2.3. An example of LFP traces in the transverse (top) and septotemporal (bottom) directions during a sharp wave-ripple event. Taken from Berenyi et al. (2013).

II. Modeling extracellular potentials of the hippocampus

3. The spiking component of oscillatory extracellular potentials in the rat hippocampus

3.1 Introduction

Oscillations in extracellular electrical recordings within neural tissue are thought to reflect coordinated network activity, although their functional role and the physiology underlying their emergence remain enigmatic (Buzsáki 2006). The extracellular signal contains ~40-500 μV spikes (~1 ms wide) from the action potentials (APs) of nearby neurons (Gold et al. 2006), as well as slower features that are more widespread across the cortex and range from tens to thousands of microvolts. The precise origins of the latter components, collectively referred to as the local field potential (LFP), are still poorly understood (Logothetis 2003, Buzsáki et al. 2012, Einevoll et al. 2013), but postsynaptic currents are typically presumed to be the dominant source of LFP fluctuations (Mitzdorf 1985). As a result, researchers often filter their recordings in an attempt to separate synaptic input (~300 Hz) from spiking output (>500 Hz) of the neuronal population around the electrode. Other contributors have been proposed (Buzsáki et al. 2012), but experimental decomposition of LFPs is rarely feasible because transmembrane currents over several hundred micrometers are integrated into the signals (Katzner et al. 2009, Lindén et al. 2011).

Observing the LFP and its relationship with neuronal firing is a common method of identifying network oscillations. In general, as oscillation frequency increases, signal power tends to decrease (Buzsáki & Draguhn 2004). An exception is found in the 100-200 Hz band in the rat hippocampus, in which power and frequency are positively correlated for 90-150 Hz epsilon (often referred to as "fast gamma") (Sullivan et al. 2011, Belluscio et al. 2012) and 140-200 Hz sharp wave-ripple (SPW-R) oscillations (Csicsvari et al. 1999b, Sullivan et al. 2011). There are two general aspects of such oscillatory phenomena to be explained: the mechanisms for coordinating network activity and the current sources generating the measured signal. Several of the former have been proposed for SPW-Rs (Ylinen et al. 1995b, Traub & Bibbig 2000, Brunel & Wang 2003, Maier et al. 2011), with the common theme that rippling in CA1 emerges as the network responds to the excitatory impulse from CA3 that makes up the sharp wave (Buzsáki 1986). Dramatic increases in the firing of pyramidal cells and some types of interneurons are observed during SPW-Rs, with spikes phase-locked to the ripple field (Buzsáki et al. 1992, Csicsvari et al. 1999a, Klausberger et al. 2003, 2004). Although nearby APs will contribute features to ripple waveforms (Buzsáki 1986) (Reichinnek et al. 2010), perisomatic inhibitory currents in pyramidal cells were thought to generate most of the ripple signal (Ylinen et al. 1995b). However, several recent studies report evidence of spike "contamination" of LFP oscillations (Ray et al. 2008c, Quilichini et al. 2010, Zanos et al. 2011, Ray & Maunsell 2011a, Belluscio et al. 2012). Utilizing detailed biophysical models of neuronal populations of the hippocampus, as well as previously reported in vitro measurements of the LFP contributions from individual interneurons (Glickfeld et

al. 2009, Bazelot et al. 2010), we show that spiking neuron populations can generate a substantial proportion of the power above 100 Hz in the local extracellular field.

3.2 Methods

3.2.1 Neuron models

Neurons were compartmental models based on reconstructed cells from the rat hippocampus and simulated in NEURON (Carnevale & Hines 2006). Pyramidal cells throughout the population were based on a single neuron from rat CA1 that was patched, stained, and reconstructed by Henze et al. (2000), and modeled by Gold et al. (2006, 2007) to recreate extracellular action potential (EAP) waveforms (cell D151a; available for download at http://senselab.med.yale.edu/modeldb/ShowModel.asp?model=84589). The model neuron has the following basic dimensions: soma surface area, 559 μm^2; total dendrite length, 10,155 μm; vertical (stratum oriens to stratum lacunosum-moleculare) dendritic arbor height, 677 μm. In addition to the passive properties of the membrane (membrane resistance R_m = 15 kΩ m^2; membrane capacitance C_m = 1 μF cm^{-2}; intracellular resistivity R_i = 70 Ω cm), the model incorporates 12 types of ion channels, including Na^+ , K^+, Ca^{2+}, Ca^{2+}-dependent K^+, and dendritic hyperpolarization-activated I_h currents. The model had a resting membrane potential at the soma of -65 mV. A total of 512 compartments and a 0.01 ms time step were used for the simulations.

The dentate gyrus basket cell model of Norenberg et al. (2010) and Hu et al. (2010) was adopted and modified for estimating the extracellular potentials generated by AP currents in the CA1 interneuron population during fast oscillations. Its membrane

incorporates nonuniform passive resistance, I_h currents, and Na^+ and K^+ channels that confer the fast-spiking behavior typical of these interneurons (Wang & Buzsáki 1996). The model includes an extensive unmyelinated axon, which was morphed to remain within a flat disk around the CA1 pyramidal layer (see below). The model neuron has soma surface area of 883 μm^2, total dendrite length of 3756 μm, vertical (stratum oriens to stratum lacunosum-moleculare) dendritic arbor height of 419 μm, and total axon length of 17,461 μm. Its initial membrane properties ($R_{m,soma}$ = 6.4 kΩ cm^2; $R_{m,prox.\ dend.}$ = 6.4 kΩ cm^2; $R_{m,dist.\ dend.}$ = 12.7 kΩ cm^2; $R_{m,axon}$ = 325.4 kΩ cm^2; C_m = 1.06 μF cm^{-2}; R_i = 137 Ω cm) were originally determined by fitting to in vitro measurements of basket cell responses to current injection (Hu et al. 2010, Nörenberg et al. 2010), resulting in axon Rm values almost 2 orders of magnitude greater than the somatic Rm, and a low Na^+ channel density in the distal axon (30 mS cm^{-2}, compared with 200 mS cm^{-2} in the soma and 600 mS cm^{-2} in the proximal axon). However, these parameter fits would have been affected by the myelination that is present on portions of basket cell axons (Freund & Buzsáki 1996). In an attempt to obtain an upper bound on the axon contribution to EAPs by allowing strong AP propagation through the entire axonal arbor, we changed the axon Rm to that of the soma, kept the high Na^+ channel density of the proximal axon, and we set the Na^+ channel density in the distal axon to the somatic value. The model had a resting membrane potential at the soma of -66.3 mV. Basket cell simulations were performed using 2935 compartments and a 0.001 ms time step. The extensive axon and fast channel kinetics necessitated a shorter time step than the pyramidal cell model.

Synaptic inputs were modeled as transient conductance changes with a double exponential time profile $g(t) = G_0 [\exp(-t/\tau_{decay}) - \exp(-t/\tau_{rise})]$ in series with a reversal potential E_{syn}, which had a value of 0 mV for excitatory synapses (Jonas et al. 1993) and -75 mV for inhibitory (Buhl et al. 1995). To isolate the AP currents, spikes were elicited by randomly placed synapses on the dendrites (in a volley of 50 excitatory and 50 inhibitory synapses for the pyramidal cell, but only 15 excitatory synapses and no inhibition for the basket cell) in 50 trials. Each trial was then repeated with a passive soma and axon and the same synaptic input, which failed to elicit an AP. The membrane currents of the "suppressed-AP" case were subtracted from those of the spiking case, and the remaining membrane currents from 2 ms before to 5 ms after the somatic V_m passed above -10 mV were saved and averaged across all trials to remove effects of the specific synapse distribution. These "average AP currents," cleansed of any direct synaptic contributions, were then used to calculate the extracellular potentials within each spiking population. We confirmed that suppressing APs in a spiking population (see above) and adding in these average AP currents at the same times and locations as spikes in the fully active population introduced negligible differences in the extracellular potentials.

In simulations of synaptically generated LFPs within pyramidal cell populations, active ion channels were removed from the entire membrane to prevent spike generation at any point in the cell. Synapses were then distributed randomly throughout certain dendritic regions, with inhibitory synapses restricted to the soma and dendritic compartments ~100 μm from the soma, and excitatory synapses in the apical dendrites 100-350 μm away from the soma, in the region of stratum radiatum Schaffer collateral

input. The precise kinetics of synapse conductances are notoriously difficult to measure due to cable filtering, but for fast excitatory (e.g., AMPA receptor-mediated) and inhibitory ($GABA_A$ receptor-mediated) synapses, estimates for τ_{rise} and τ_{decay} (defined above) range from 0.1-1 and 2-10 ms, respectively (Hestrin et al. 1990, Jonas et al. 1993, Maccaferri et al. 2000, Glickfeld et al. 2009, Bazelot et al. 2010). We set τ_{rise} to 0.1 ms and tested τ_{decay} values from 1 to 7 ms. Two hundred excitatory and 200 inhibitory synapses were activated every 50 ms, with individual peak synapse conductances of G_0 = 0.3 nS.

3.2.2 Calculating extracellular potentials

We approximated the extracellular medium as a uniform, isotropic, ohmic conductor with resistivity σ = 333 Ω cm (López-Aguado et al. 2001, Logothetis et al. 2007, Goto et al. 2010, Anastassiou et al. 2011; but see Bedard et al. 2010). The extracellular potential, V_e, at a particular location within a population of cells is simply the linear superposition of the contributions from all compartments of all cells (10^5-10^6 total in the population simulations), with the contribution of each compartment being proportional to its net transmembrane current and inversely proportional to its distance from the electrode (see Figure 3.1A). We treated compartments as line sources of current (Holt & Koch 1999, Gold et al. 2006). Using Ohm's law in a cylindrical coordinate system,

$$V_e = \frac{\rho I}{4\pi l}\left|\log\frac{\sqrt{h^2+r^2}-h}{\sqrt{s^2+r^2}-s}\right|$$

where I is transmembrane current (positive value indicates current exiting the membrane), l is compartment length, r is the perpendicular distance from the electrode to a line through the compartment, h is longitudinal distance along this line from the electrode to one end of the compartment, and $s = l + h$ is longitudinal distance to the other end of the compartment. These calculations were performed in MATLAB using the results of the NEURON simulations.

3.2.2 Population activity

For the pyramidal cell population, we used a single morphology and one set of membrane parameters, and likewise for the basket cell population. Cells were oriented with the apical axis along the stratum oriens to stratum radiatum direction, with random rotations about this axis, and somata were randomly placed within the cell body layers for the respective cell types. The centers of pyramidal cell somata were located within a disk 40 μm thick and 1 mm in diameter at a density of 3×10^5 per cm^3 (Boss et al. 1987, Aika et al. 1994) (9416 sites), and the basket cell soma centers were within an 80-μm-thick disk (Freund & Buzsáki 1996) of the same diameter at a density of 7.5×10^3 per cm^3, resulting in 471 sites (5% of pyramidal cell number; 2.5% of the density) (Olbrich & Braak 1985, Aika et al. 1994, Freund & Buzsáki 1996). This basket cell population approximates interneurons known to be active during SPW-Rs (Klausberger et al. 2003, 2004). Cell bodies were excluded from a 15 μm radius volume around the electrode shank. Because the cell position refers to the location of the center of its soma, which had

a maximum diameter of 11.5 μm for the pyramidal cell and 12 μm for the basket cell, soma surfaces could therefore approach within 9 μm of the "virtual electrode."

The dendritic arbor of each pyramidal neuron in the rat hippocampus {which typically has a total of ~30,000 synaptic contacts; Megias:2001uh} constantly receives input from numerous afferents, but independently simulating all 9416 neurons in our population would have prohibited us from effectively exploring the large parameter space available for the spatiotemporal patterns of synaptic input. Instead, similar to our technique for constructing a population of spiking neurons, we simulated 50 passive pyramidal neurons receiving similar synaptic input patterns (see Section 3.2.1). The resulting membrane currents in each compartment were averaged across these 50 trials to obtain the "average subthreshold cell," which was then used to calculate the contribution from constituent cells in the population. The contributions from all cells within 100 μm of the electrode shank were calculated; outside of this radius, the potentials from 20% of the cells were scaled up by a factor of 5 and added to the potentials from those of the inner cells. This estimation method resulted in ~5% error when compared with tests in which each cell was separately simulated and included in the calculation of the population potentials, but reduced simulation time by nearly 2 orders of magnitude.

By using average subthreshold and AP currents in cells with synaptic currents removed, we effectively decoupled spike and synapse currents within the population and could estimate their contributions separately. When simulating AP-generated potentials from rhythmically firing cell populations, the spiking neurons were randomly chosen from the population, with an independent set each oscillation period. Spike times were

pulled from a periodic probability density function (pdf) that consisted of repeating Gaussians ($\exp[-t^2/2\sigma^2]$). Unless otherwise noted (see Figure 3.3), we set σ to one-fifth of the cycle period. This pdf was also used to generate synapse activation times for simulations of synaptically generated LFPs (see Figure 3.10). Additional spiking from cells that are poorly modulated within an oscillation does not impart substantial power at frequencies ~500 Hz on average (see Figure 3.2, black curves, which are barely visible in C because they remain below 2.2×10^{-7}).

3.2.3 IPSCs from unitary field potentials

To estimate the contribution of IPSCs elicited by firing basket cells to LFPs, we summed up the stratum pyramidale "unitary field potentials" (uFields) arising from individual CA1 basket cells measured by Glickfeld et al. (2009). Spike times for basket cells were pulled from the periodic Gaussian pdf described above, and a positive uField was added at each "spike" to the total V_e with the following characteristics: 15.8 μV amplitude, linear rise with 1.2 ms 10-90% rise time, exponential decay with 6.6 ms time constant (Glickfeld et al. 2009) (see Figure 3.10 A). Bazelot et al. (2010) measured similar uFields from basket cells in CA3, and they found that the uFields could be detected in stratum pyramidale across a total distance of ~1 mm on average, although their amplitudes typically decreased by >50% within 250-300 μm from the locations at which they were maximal. The same uField was therefore added for each basket cell spike within a 500-μm-diameter disk around the electrode, regardless of the exact location of the cell.

3.2.4 Experimental procedures

In vivo CA1 recordings from a male Long– Evans rat with a chronically implanted multielectrode array were used for direct comparison with simulation results. All experimental data presented here are from eight channels from one shank of a silicon multi-electrode array within dorsal CA1 during one recording session, while the animal slept in its home cage. Surgery, recording methods, and experimental procedures were described by Montgomery et al. (2008).

3.2.5 Data analysis

Filters were implemented using bandpass Butterworth IIR filters, designed using the MATLAB DSP Systems Toolbox, with >60 dB stopband attenuation. The filters were applied in both the forward and reverse directions to remove phase distortions. For some portions of the LFP analysis of in vivo recordings, electrode signals were downsampled to 1250 Hz. Current source densities (CSDs) were calculated using the 1-D second spatial derivative of the depth-recorded LFPs (Nicholson & Freeman 1975). In the sleep session analyzed here, theta epochs were detected using the ratio of power in the theta band (5–11 Hz) to delta band (1– 4 Hz) of the LFP (Mizuseki et al. 2009). Nontheta epochs during sleep sessions were considered slow wave sleep (SWS). All data presented here are from SWS.

To detect SPW-R events in in vivo recordings, we followed a procedure based on Sullivan et al. (2011). In brief, the LFP signal was bandpass filtered from 140 to 210 Hz,

rectified, smoothed with three-sample boxcar kernel, and z-score normalized. Portions of the resulting signal were marked as candidate events if their amplitude was >2 SDs above the mean. Event peaks were extracted by taking the maxima of the 140-210 Hz pyramidal layer CSD and enforcing a minimum separation between event peaks of 50 ms. One hundred millisecond segments of the wide-band LFP signal around these event peaks were then analyzed further using the multitaper FFT in the MATLAB signal processing toolbox. FFT power spectra were z-score normalized by the mean and SD of power at each frequency in 20,000 randomly chosen 100 ms windows throughout the SWS epochs during the recording session. Candidate events with spectral peaks >3 SD above the mean that were between 140 and 210 Hz were classified as ripples.

The duration of ripple events and the frequency and amplitude of individual waves within a single ripple vary in vivo, but the amplitude and frequency of our simulated ripples are approximately constant. To perform a fair comparison, we also estimated the instantaneous frequency and amplitude of individual troughs in the 50-210 Hz bandpass-filtered signal (the pass band was widened from the SPW-R detection procedure above to prevent attenuation of ~100 Hz oscillations). The frequency of the trough was defined as the inverse of the time interval between the peaks flanking it, and its amplitude was defined as the absolute value of the trough minimum of the filtered signal. Only troughs with flanking peaks that were within oscillatory events (defined as intervals during which the 1.4 ms boxcar average of the absolute value of the 50-210 Hz bandpass filtered signal remained above 1 SD and has at least one peak >2 SDs; Csicsvari et al. 1999b) were included.

Power spectra presented for simulated extracellular potentials were first calculated using 100 ms time windows of the raw signal, and the spectra were then averaged over 25 trials.

3.3 Results

3.3.1 Spiking contribution to the LFP

To reliably estimate the spike content of extracellular recordings using our theoretical framework, it is necessary to simulate accurate spike waveforms. The model by Gold et al. (2006, 2007) was developed for this purpose, emulating intracellular and extracellular action potentials based on simultaneous in vivo intracellular and extracellular recordings of rat CA1 pyramidal cell APs (Henze et al. 2000) based on appropriate distribution of transmembrane currents. Figure 3.1 shows the spatial variation of EAPs produced by the pyramidal cell model with membrane biophysics governed by parameter set A of Gold et al. (2007). Before calculating the extracellular potential V_e, subthreshold membrane currents were subtracted, and the remaining membrane currents were averaged over 50 trials. To visualize EAP trends that were less dependent on details of the dendritic morphology, each plotted waveform is an average of 25 EAPs on a ring around the apical axis (Figure 3.1B, top to bottom), with the radius and vertical position indicated by the starting point of each trace. The amplitudes of EAPs decrease with distance from the soma (Figure 3.1C), and they widen (Figure 3.1D) due to both the decreasing dominance of the strong Na^+ currents at the soma and axon hillock (Gold et al. 2006), as well as intrinsic low-pass filtering of currents by the cell membrane, which

leads to smaller current dipoles for high-frequency components (Mitzdorf 1985, Pettersen & Einevoll 2008).

Using these average AP currents, we calculated the extracellular potentials due to spiking within a population of pyramidal cells arranged to resemble those in the dorsal CA1 region of the rat hippocampus (Figure 3.2A). We computed V_e during firing that was either random or synchronized by a rhythm of frequency f, with f ranging from 50 to 400 Hz (Figure 3.2B). In the rhythmic cases, spike times were modulated by a periodic Gaussian pdf, with the SD of spike times in each group of APs given by $\sigma = 0.2/f$. Because f and σ were inversely related, higher frequency rhythms more effectively synchronized spiking within the population, resulting in more EAP overlap and greater signal power. We quantified this trend using the averaged FFT of 100 ms segments of V_e over 25 trials (Figure 3.2C). Oscillation power peaked between 150 and 200 Hz, and then slowly decreased with further increases in frequency, because fewer APs occurred within each period. In these simulations, 2, 4, or 6% of the population fired each 10 ms, which is within the physiological range estimated for fast oscillations of the rat hippocampus during SWS by Csicsvari et al. (1999a, 1999b, 2000).

The power–frequency relationship depends crucially on the relationship between σ and f. Our choice of the $\sigma = 0.2/f$ spread in each Gaussian-shaped packet of spikes in the population results in an approximately sinusoidal shape of the spiking pdf with a nearly full depth of modulation. Lower depths of modulation (e.g., $\sigma = 0.3/f$) may be treated as a combination of a fully modulated set of events superimposed on a baseline of unmodulated activity (i.e., random events with constant probability), and the effective

"baseline" spikes add inconsistent power at frequencies <500 Hz that averages out over multiple events (Figure 3.2 B, C, black traces). Firing phase histograms constructed from many fast LFP oscillations recorded in vivo do not appear to show population bursts that are substantially narrower than the period of oscillation in the normal hippocampus (Ylinen et al. 1995b, Csicsvari et al. 1999b, Csicsvari et al. 2003, Colgin et al. 2009, Sullivan et al. 2011). If tighter phase coupling was present, it led to increases in the power at both the oscillation frequency as well as at its harmonics in our simulations. For example, decreasing σ from 4 to 2 ms in the 50 Hz case approximately tripled the power of the 50 Hz LFP oscillations, but also caused a peak at 100 Hz to emerge in the spectrum that was around one-half the power of the 50 Hz component (Figure 3.3 A, B). Further decreasing σ to 1 ms caused the power of the 100 Hz harmonic to become greater than the 50 Hz peak, due to a more prominent positive repolarization phase (Figure 3.3A). Firing rates during normal oscillations near 50 Hz are not as high as during the faster ripple oscillations, however, and the number of cells effectively modulated by medium to slow gamma rhythms is substantially less than for epsilon frequency rhythms (Belluscio et al. 2012). These considerations are instead most relevant during spike-and-wave discharges and "fast ripples" of the epileptic state (Bragin et al. 1999, Blumenfeld 2005, Foffani et al. 2007, Staley 2007).

If σ is independent of f, then rhythms with frequencies less than ~$0.2/\sigma$ will have substantial power in their harmonics, with the power of these harmonics determined by σ. This is illustrated for σ = 3, 2, and 1 ms in Figure 3.3C. The average signal power during rhythms faster than that which was most powerful for a given σ dropped off quickly in

our scheme (we kept the average firing rate of the population constant while varying the frequency of the rhythm that modulates spike timing), because faster rhythms have fewer spikes clustered into each population burst. Additionally, once f went above ~$0.2/\sigma$, neighboring burst events overlapped and the depth of modulation of firing rapidly fell off. The peak power was between 150 and 200 Hz in the $\sigma = 0.2/f$ case (Figure 3.2C) because that range was where the optimal balance was achieved between synchrony and spike count in each population burst.

When the pyramidal cell population was in an active state and the firing rhythm was synchronized over several hundred micrometers, much of the field potential amplitude could be attributed to cells too far away for their APs to be recognized as such (Buzsáki 2004). Figure 3.4 illustrates this with an eight-electrode shank in the center of a 1-mm-diameter population in which spike times are modulated by a 150 Hz rhythm. In Figure 3.4A, the extracellular potentials are decomposed by cell distance from the electrode in 50 μm steps in an outside-in manner. That is, cells with somata in a particular 50-μm-wide ring have their EAPs added to the signal generated by all the cells further away. The firing of cells >100 μm from the electrodes produced a smooth 150 Hz V_e that was at least one-half of the amplitude of most peaks in the cumulative potential, with more proximal EAPs adding larger but narrower spikes on top of this signal at the pyramidal layer, but adding little to the signal in the dendritic layers. In terms of oscillatory power (Figure 3.4B), spikes from the few cells near the electrode created a wideband spectrum, although with a consistent peak at 150 Hz (which is why this peak dominates the 25 trial average spectrum in Figure 3.4B). The most power coming from an

individual ring was for cells 50-100 μm from the electrode; this range had the most effective combination of spike count and EAP amplitude. On average, the signal originating from cells 100-150 μm away was as powerful as that from cells closer than 50 μm (Figure 3.4B), and adding the contribution from all cells >100 μm to the signal from cells <100 μm increased the signal power fivefold (Figure 3.4C).

These results depended on a high degree of synchrony across space in the rhythm driving the population firing. Substantial phase coherence of LFP oscillations is often present over distances ~1 mm in both the transverse and longitudinal directions within the CA1 pyramidal layer during SWRs occurring in SWS (Ylinen et al. 1995b, Sullivan et al. 2011), with the amplitude and spatial coherence of the ripple positively correlated (Csicsvari et al. 2000). Phase delays and decoherence within CA1 have been reported for theta and gamma band oscillations (Bragin et al. 1995, Lubenov & Siapas 2009), but we are not aware of detailed analyses of the spatial profile of fast oscillation phase synchrony within CA1 stratum pyramidale during theta activity. If population synchrony is related to oscillation frequency, with slower oscillations exhibiting a greater spread in spike timing, then the temporal delays associated with activity propagating at a finite speed through the hippocampus (Lubenov & Siapas 2009) will affect high-frequency rhythms more than those at lower frequencies, because a given temporal delay in activity between two locations will correspond to a larger phase delay for the faster oscillation. For example, temporal delays of 10 μs/μm along one direction (e.g., if spiking activity is locked to the local theta phase, which propagates along the septotemporal axis at approximately this speed) (Lubenov & Siapas 2009) resulted in an average spectral power at the oscillation

frequency that was approximately one-half of the power in the case with no delays for a population undergoing 100 Hz oscillations, and the ratio was approximately one-quarter for 200 Hz oscillations (Figure 3.5). Thus, there may be a close link between high-frequency power and temporal coordination of firing across space, with a more synchronized population able to generate stronger oscillations in the LFP (Csicsvari et al. 2000; Ray et al. 2008c).

3.3.2 Comparison with in vivo recordings

We analyzed recordings from linear electrode arrays in the rat hippocampus during SWS (Montgomery et al. 2008). SWRs were detected in dorsal CA1 during SWS epochs from a single sleep session, and events with a dominant ripple frequency between 140 and 160 Hz were extracted for comparison to V_e within a simulated pyramidal cell population exhibiting a 150 Hz firing rhythm (Figure 3.6). During in vivo SWR events, APs in a large portion of pyramidal cells and some inhibitory interneuron types (e.g., basket cells and bistratified cells) (Klausberger et al. 2003, 2004, Varga et al. 2012, Forro et al. 2013) are phase-locked to the field ripple, with pyramidal cell firing centered at the ripple trough (recorded in stratum pyramidale) and interneurons lagging ~1-2 ms (Sullivan et al. 2011). Of the oscillatory events that met our SWR detection criteria, 26 had dominant frequencies between 140 and 160 Hz. Averaging the wideband signal during these events (Figure 3.6A) showed that, overall, they indeed occurred during negative deflections in the stratum radiatum LFP, reflecting excitatory “sharp wave” input from CA3 (Ylinen et al. 1995b). The oscillatory characteristics of this input were highly

variable, however, in contrast to the consistent perisomatic ripple. Applying a bandpass filter from 50 to 5000 Hz before averaging removed the slower SPW LFP deflection and revealed weaker ripple-frequency oscillations in stratum radiatum with the opposite phase of the stratum pyramidale potentials (Figure 3.6B), reflecting what are most likely passive return currents in the dendrites from a perisomatic drive. We simulated similar depth profiles for rhythmic population firing at the same frequencies as these 26 in vivo ripples, then applied the same filter and averaged the resulting potentials (Figure 3.6D). The amplitude and phase profiles of the simulated averages were very similar to those of the in vivo recordings (Figure 3.6B), and individual in silico voltage traces were characteristically similar to the in vivo ripples (Figure 3.6C). More quantitative comparisons of these AP-generated potentials to both in vivo recordings and simulations of synaptically generated LFPs are described below (see Figure 3.10).

3.3.3 Interneuron AP contributions to field potentials

Some interneuron types, specifically basket and bistratified cells (Klausberger et al. 2003, 2004), substantially increase their firing during SWRs, with spike times modulated by the ripple. While these cells make up <5% of the cell population in CA1 (Olbrich & Braak 1985, Aika et al. 1994, Freund & Buzsáki 1996), their average firing rates during SWRs can be three to four times greater (Csicsvari et al. 1999a, Csicsvari et al. 2000). To estimate the contribution of their EAPs to SWRs and other fast oscillations, we used the dentate gyrus basket cell model of Nörenberg et al. (2010) and Hu et al. (2010). While the model was not specifically tuned to reproduce basket cell EAPs, the

qualitative features of the EAP shape and amplitude (Figure 3.7A) are similar to those reported by Henze et al. (2000) for a CA1 basket cell that was 50-100 μm from two neighboring shanks of a multielectrode array. Their EAP amplitude is similar to pyramidal cell EAPs, but the basket cell EAPs were significantly narrower (Figure 3.7B), consistent with experimental observations (Bartho et al. 2004). A previous modeling study saw little effect of axon fibers beyond the initial segment on EAPs (Gold et al. 2006), but that was for pyramidal cells with myelinated axons that project out of the local region. The situation could plausibly be different with a dense arbor of unmyelinated axon fibers and terminals, as with local interneurons. However, we saw only minor effects on the average EAP profile (Figure 3.7B) for basket cells with and without an extensive, active axon (see Materials and Methods).

We simulated V_e signatures of spiking in a combined population of 471 basket cells and 9416 pyramidal cells. The basket cell somata were positioned in a disk of the same radius as the pyramidal cells (0.5 mm), but approximately twice as thick (100 μm); this population was intended to account for both the basket and bistratified cells that are active during SWRs. We allowed 40% of the basket cells and 8% of the pyramidal cells to fire each 10 ms. With the number of basket cells being 5% of the number of pyramidal cells, but five times more active, the total number of basket cell APs was one-quarter the total number of pyramidal cell APs. These values are similar to the activity levels reported in (Csicsvari et al. 1999a, 2000) during SWRs, although they actually overestimate the proportion of spikes estimated to originate from basket cells. Spike times in both populations were again clustered in population bursts with $\sigma = 0.2/f$

(Csicsvari et al. 1999a), and the preferred spike phase for basket cells was delayed by 90° from pyramidal cell firing (Sullivan et al. 2011). The lower numbers of basket cell spikes and their narrower width resulted in a substantially smaller contribution to the combined population potentials than the pyramidal cell spikes. Figure 3.8, B and D, shows the case of a 200 Hz rhythm, and the results for 50-400 Hz are summarized in Figure 3.8C. The average power over 25 trials at the oscillation frequency of the extracellular potentials generated by spiking basket cells was <5%, even at 400 Hz. The more visible increases in power when this was added to the pyramid AP-generated potentials (Figure 3.8C) are due to the ($V_e^{PYR} \times V_e^{BC}$) product term contributing to the power measure when the ($V_e^{PYR} + V_e^{BC}$) signal amplitude was squared.

Consistent with their small effect on average single cell EAPs, axons in the basket cell population contributed little to the LFP oscillation. For the 200 Hz oscillations in Figure 3.7, the root-mean-square error of the pyramidal layer V_e with the truncated axon (compared with the population with the full axon) was 2.7 μV, resulting in an average power at 200 Hz that was ~8% less for the population with truncated axons.

3.3.4 Synaptic currents during fast oscillations

In the AP-generated extracellular potentials described above, the increase in power with increasing frequency (up to ~150 Hz) is due to the narrow EAPs overlapping more as the faster rhythms more effectively synchronize spikes. This is in contrast to the behavior expected for signals generated by slower postsynaptic currents with similar temporal synchrony. The postsynaptic conductance change resulting from synapse

activation has a quick rise, but its decay is much slower than an AP, with exponential decay time constants between 2 and 10 ms in hippocampal pyramidal cells (Hestrin et al. 1990, Jonas et al. 1993, Maccaferri et al. 2000). The slower this decay, the greater the attenuation of the high-frequency component of the total synaptic current.

We explored the frequency dependence of V_e in a population receiving layer-specific oscillatory synaptic input (Figure 3.9A). The initiation times for the rhythmically modulated synapses were determined by the same pdf as the APs in Figures 3.2, 3.4, 3.6, and 3.8. The potentials shown are for synapses with τ_{decay} of 4 ms (Materials and Methods), but similar results were obtained when τ_{decay} was varied from 1 to 7 ms (Figure 3.9 C, E, insets). In one scheme, constant excitation impinged on the apical Schaffer collateral dendritic region along with rhythmic inhibition at perisomatic basket and bistratified cell target domains (Sik et al. 1994, Megías et al. 2001) (Figure 3.9 B, C), similar to the input pattern thought to be important for rippling LFPs in CA1 during SWRs (Buzsáki et al. 1992, Csicsvari et al. 2000). Next, the opposite pattern was used rhythmic apical excitation and constant perisomatic inhibition (Figure 3.9 D, E), analogous to oscillating input from CA3 (or entorhinal cortex, although entorhinal input is even more distal) (Andersen et al. 2007) during tonic inhibition. The ability of such synaptic inputs to generate oscillatory signals at the rhythm frequency rapidly decreases as the oscillation frequency increases, which is illustrated qualitatively in Figure 3.9, B and D, and quantitatively in Figure 3.9, C and E. Also noteworthy are the differences in the depth profile of the oscillating signals between the two schemes shown. Apical excitation generated larger amplitude fluctuations in the extracellular potentials in the

dendritic layers, with a distinct phase reversal just proximal to the somatic layer, similar to gamma frequency LFPs in CA1 following lesions to the entorhinal cortex (Bragin et al. 1995). In contrast, rhythmic perisomatic inhibition produced a relatively strong oscillation in the pyramidal layer potential, but extended weakly into the dendritic layers. There were two primary causes of this: (1) differences in the strength and geometry of the current dipoles produced by synaptic input distributed around the soma versus apical input, and (2) an inhibitory synapse reversal potential $E_{rev,inh}$ that is closer to the subthreshold V_m than the excitatory $E_{rev,exc}$. When either (1) rhythmic excitation is instead placed perisomatically with constant inhibition in the apical dendrites, or (2) $E_{rev,inh}$ is set to -130 mV (the same voltage difference from the -65 mV resting potential of the membrane as the 0 mV $E_{rev,exc}$), the dendritic layer V_e did start to oscillate, but both alternatives produced substantially weaker oscillations than the case of a strong apical rhythmic drive (data not shown).

3.3.5 Combining APs and IPSCs

Our neuronal population simulation methods allow us to explore the effects of the spatiotemporal distribution, reversal potentials, and kinetics of synaptic currents on extracellular potentials. Unfortunately, the large number of parameters and the lack of precise experimental validation of many of them make a reliable quantification of synaptic contributions to fast LFPs impractical. To perform more trustworthy quantitative comparisons between synaptically generated field potentials and both our simulated AP-generated potentials and in vivo recordings, we took advantage of measurements reported

by Glickfeld et al. (2009) and Bazelot et al. (2010). They performed intracellular and extracellular recordings in hippocampal slices and characterized the extracellular uFields following individual inhibitory interneurons APs. These deflections in the extracellular potential presumably reflect the summed IPSCs elicited in the numerous neurons contacted by the axons of the interneurons. The uFields were visible over several hundred micrometers, but their amplitude decayed with distance, with amplitudes reduced by >50% at electrodes 250-300 μm from the site with the largest uField (Bazelot et al. 2010). We therefore constructed an interneuron population with the same parameters as before, but only included cells within 250 μm of the electrode, to estimate the combined field potentials when 30% of the population fired every 10 ms (Csicsvari et al. 2000). We added the average CA1 basket cell stratum pyramidale uField (Figure 3.10A; 15.8 μV amplitude, linear rise with 1.2 ms 10-90% rise time, exponential decay with 6.6 ms time constant) (Glickfeld et al. 2009) to the total stratum pyramidale V_e at the time of each basket cell spike. Spike times were modulated by a periodic Gaussian pdf ($\sigma = 0.2/f$) at different frequencies f.

As in the simulations of compartmental models receiving synaptic input, the amplitude of the oscillatory component of the resulting LFP decreased with increasing frequency (Figure 3.10B). In this case, however, there were fewer critical parameters to determine because we started with experimentally characterized basket cell uFields. We therefore used these simulations to estimate the contributions of both IPSCs and pyramidal cell AP currents to oscillations in the cumulative LFP and compared them to in vivo ripples. The amplitude and frequency of the V_e oscillation is not constant during

SWRs, however, in contrast with the more consistent simulated potentials generated by our simulations, so fixed time window FFT measurements of oscillation power would not produce a fair comparison. We instead measured instantaneous frequencies and amplitudes of individual waves within detected ripples and compared these with simulated ripples. With 10% of the pyramidal cell population firing and 30% of the basket cell population producing uFields each 10 ms (Csicsvari et al. 2000), the waveform characteristics, ripple amplitudes, and frequency–amplitude relationship of in vivo ripples with dominant frequencies between 140 and 160 Hz were very well reproduced by the combined AP-generated and IPSC-generated ripples (Figure 3.10 C, D). The contributions of the two components were similar over the 100-200 Hz frequency range, with APs remaining similarly powerful (Figure 3.2), but IPSC-generated power decreasing with increasing frequency. In these simulations, the basket cell firing rhythm underlying the IPSC-generated ripples (i.e., the summed uFields) lagged the pyramidal cell rhythm by 90° (Sullivan et al. 2011). Experimental estimates of the average phase lag are between 60 and 100° for gamma, epsilon, and ripple oscillations in CA1 (Csicsvari et al. 2003, Sullivan et al. 2011). The combined ripple amplitudes were reduced by 10-13 and 40-47% for 0 and 180° phase lags, respectively, and the oscillation amplitude of each component of the simulated LFPs was proportional to the size of the active population (data not shown).

3.4 Discussion

Given the observed relationship between spike synchrony and oscillation frequency during hippocampal fast oscillations (Csicsvari et al. 1999b, Sullivan et al. 2011), the increase in oscillation power at frequencies >80 Hz is likely to involve more substantial contributions from local AP currents to the measured LFP signal. The details of our findings rest on accurate reproduction of the spatiotemporal profiles of AP membrane currents, for which the CA1 pyramidal cell model of Gold et al. (2006, 2007) was developed. The EAP amplitudes from our model (cell D151a) (Gold et al. 2007) are on the low end of the spectrum reported by Henze et al. (2000). Our population model may therefore underestimate stratum pyramidale signal amplitudes. Furthermore, the model of Gold et al. was not designed to accurately recreate slower Ca^{2+} spikes (Kamondi et al. 1998), spike afterpotentials (afterhyperpolarization, or AHP, being the most prominent) (Gustafsson & Wigström 1981, Storm 1987, 1989), and intrinsic membrane oscillations (Leung 1991, 1998), all of which may affect LFPs.

While our simulations indicate that APs in basket cells, even with their dense local constellation of axon terminals, contribute much less to slower components of the extracellular potential than pyramidal cells, further experimental dissection or more focused axon modeling are needed to demonstrate this more definitively.

Most of the simulations presented here have event timing modulated in an approximately sinusoidal fashion, resulting from the $0.2/f$ width of each Gaussian-shaped burst. The signal power contributed by AP currents depends on the relationship between synchrony and rhythm frequency (Figure 3.3). We kept the $\sigma = 0.2/f$ relationship for spike

synchronization consistent across frequencies because of the high degree of phasic modulation of spikes within fast hippocampal oscillations (Csicsvari et al. 1999a, 1999b, 2000, Sullivan et al. 2011; but see Colgin et al. 2009). The neuronal networks of the brain do often display an excitation–frequency–synchrony relationship in which stronger excitatory driving force leads to faster oscillations (Whittington et al. 1995, Csicsvari et al. 1999b, Sullivan et al. 2011), with inhibition being effective at gating spike times (Whittington et al. 1995, Hasenstaub et al. 2005, Cardin et al. 2009).

The 100-200 Hz oscillations in the hippocampus during SWS exhibit a high degree of phase coherence across CA1 (Ylinen et al. 1995b, Csicsvari et al. 2000, Sullivan et al. 2011), as required for AP currents to contribute a substantial portion of the LFP signal. If similar coherence characteristics of fast oscillations that occur during theta states are found, it could indicate that these network patterns share common mechanisms of generation, which would have implications for our understanding of how these oscillations may assume their hypothesized role in interregional coupling in the behaving animal (Colgin et al. 2009). More detailed analyses and perturbations of network activity throughout the hippocampal– entorhinal circuit during these brain states are still needed to better appreciate how these regions are interacting.

The contribution of fast spikes to slower LFP signals additionally relies upon a large number of active, synchronous neurons. Our firing rates and synchrony parameters were motivated by the estimates of Csicsvari and colleagues (1999a, 1999b, 2000), which were based on units classified as putative pyramidal cells and interneurons, but how representative such units are of the CA1 neuron population remains an open question.

While a significant fraction of CA1 pyramidal cells may be inactive during exploration, many of the "silent cells" are active during SWS (Thompson & Best 1989).

We found that summed synaptic and AP currents are both capable of generating oscillatory extracellular potentials, and our results suggest that there is an opportunity for a transition from synaptic to spike-related currents as the dominant current generator of oscillatory potentials near 100-150 Hz. This is consistent with widespread experimental observations of a high correlation between spiking activity and power in LFP bands faster than 90 Hz, and with principal cell firing consistently centered on the oscillation trough in the cell body layer (Csicsvari et al. 1999a, 1999b, 2000, Canolty et al. 2006, Ray et al. 2008a, Le Van Quyen et al. 2008, Ray et al. 2008b, Colgin et al. 2009, Le Van Quyen et al. 2010, Bragin et al. 2011, Sullivan et al. 2011, Jackson et al. 2011, Ray & Maunsell 2011b, Belluscio et al. 2012). A specific LFP pattern near this transition point is the SPW-R complex of the hippocampal CA1 region (Buzsáki et al. 1992). These events coincide with dramatic increases in excitation and synchrony within the pyramidal cell population, more so than the interneuron population (Csicsvari et al. 1999a), and our simulated AP-generated ripples reproduce several features of the SPW-R waveform and depth profile. A large AP component of ripple fields provides a parsimonious explanation of a number of observations reported in the investigations by (Csicsvari et al. 1999a) (Csicsvari et al. 1999b, 2000): (1) a much stronger correlation between ripple amplitude and pyramidal cell firing rates than interneuron firing rates (Csicsvari et al. 1999b); (2) the summed activity of CA1 pyramidal cells better predicted ripple features than interneuron and CA3 pyramidal cell activity (Csicsvari et al. 1999a, 2000); (3) the discharge probability curve

of pyramidal cells matched the ripple power curve much more precisely than the discharge probabilities of the two classes of recorded interneurons (Csicsvari et al. 1999a); (4) ripple amplitude was correlated with the spatial coherence of pyramidal cell firing, but not with the spatial coherence of interneuron firing (Csicsvari et al. 2000); (5) oscillation amplitude was larger for higher frequencies (Csicsvari et al. 1999b).

These results do not resolve questions concerning the mechanisms of synchronization, however. Indeed, they are consistent with any mechanism that properly synchronizes pyramidal cell firing [e.g., rhythmic inhibition (Ylinen et al. 1995b); recurrent excitation (Maier et al. 2011); electrical synapses (Draguhn et al. 1998); ephaptic coupling (Holt & Koch 1999, Anastassiou et al. 2011)]. Optogenetic and pharmacogenetic manipulation of neuronal activity offers the possibility of testing these mechanisms and our hypotheses in vivo by selectively silencing either pyramidal cells or parvalbumin expressing interneurons in CA1, though the network response to SPW input with either of these cell types inactivated is unknown. We have also not addressed the shape of the SPW-R envelope. It presumably reflects the SPW synaptic excitation, inhibitory synaptic currents, AP and AHP currents, active dendritic currents such as Ca^{2+} spikes, and passive return currents from all of these.

Network and field patterns at frequencies >80 Hz have been linked to several aspects of cognition, learning, memory, and cross-regional coupling (Chrobak & Buzsáki 1996, Canolty et al. 2006, Jacobs & Kahana 2009, Colgin et al. 2009, Carr et al. 2011). At the same time, several authors have noted the likelihood that filtered LFPs at these frequencies are “contaminated” by local spiking activity (Zanos et al. 2011, Ray &

Maunsell 2011a), and our results indicate that much of the spiking component cannot be removed by subtraction of spikes from the nearby units (Zanos et al. 2011, Belluscio et al. 2012). Thus, it is worth highlighting ways to mitigate this ambiguity in the source of these signals. First, if AP currents dominate an oscillatory signal, the negative spikes created by strong inward Na^+ currents at the soma during APs should appear at the troughs of the signal in the cell body layer. If perisomatic inhibition is the primary current generating the LFP, we might also expect cells receiving this inhibition to fire near the troughs (i.e., the inhibitory current minima). However, time delays between minimal inhibitory current and depolarization of the membrane past threshold may correspond to significant phase difference at high frequencies. Indeed, in the network model of Taxidis et al. (2011), pyramidal cell spikes during SPW-Rs occurred ~90° after the trough of inhibitory synaptic current, and we have seen similar delays in preliminary simulations of synaptically driven SPW-Rs with the model of Gold et al. (2007). Second, depth recordings and current source density analyses (Nicholson & Freeman 1975, Pettersen et al. 2006, Łęski et al. 2011) can locate the signal source layers in laminated structures, and the depth profiles of synaptic currents and AP currents can differ substantially (Figures 3.6 and 3.9). Passive return currents during processes with concentrated active driving currents should cause a phase reversal somewhere along the somatodendritic axis; knowledge of the location and spread of synaptic contacts along this axis should provide clues about which processes are generating the field fluctuations. Third, phase synchrony of rhythmic spiking over several hundred micrometers within the somatic layer is

important for the summation of AP currents from many distant cells to generate a smooth LFP oscillation waveform.

It may be that fast oscillations primarily reflect a highly excited network, with local inhibitory interneurons synchronizing themselves and effectively gating principal neuron firing within narrow time windows (Hasenstaub et al. 2005, Whittington et al. 2010). Complicating this picture, excitatory input from an afferent region undergoing fast oscillations may also generate such fast LFP signals, as well as push the local network into its own fast oscillation state. Simultaneous multisite recordings along the somatodendritic axis and within the cell body layers of several connected brain regions are therefore important for the dissection of network interactions during fast oscillations.

3.5 Figures for Chapter 3

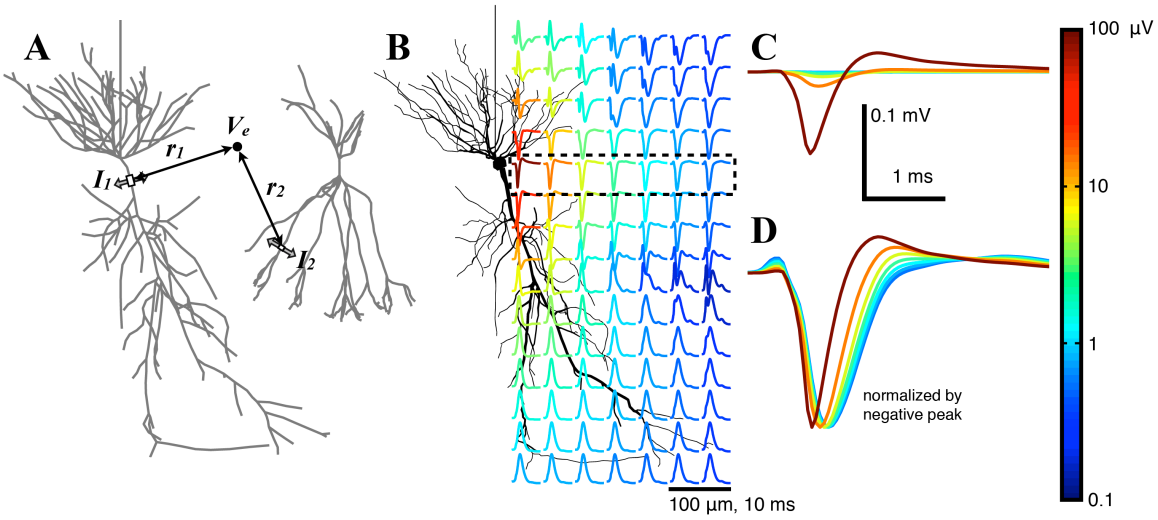

Figure 3.1. Average extracellular action potential (EAP) of the pyramidal cell model. ***A***, Illustration of V_e calculation in a population through the superposition of contributions from all compartments in all cells. Individual compartment contributions are primarily determined by their transmembrane currents and distances from the electrode. ***B***, Location dependence of the EAP for the pyramidal cell model. The peak-to-peak voltage range is indicated by the color of each trace. Subthreshold currents have been removed, and each EAP waveform is an average over 25 points at a fixed radius from the apical axis (the vertical direction here) to remove the dependence on the precise dendritic geometry. EAPs are calculated at the location of the start of each trace. ***C***, EAPs within the cell body layer (*B*, dashed box) with voltages drawn to scale. EAP amplitude decreases rapidly with distance. The largest EAP is calculated 20 µm from the soma center, and then at 50 µm intervals. ***D***, Same traces as in ***C***, but normalized by the negative peak.

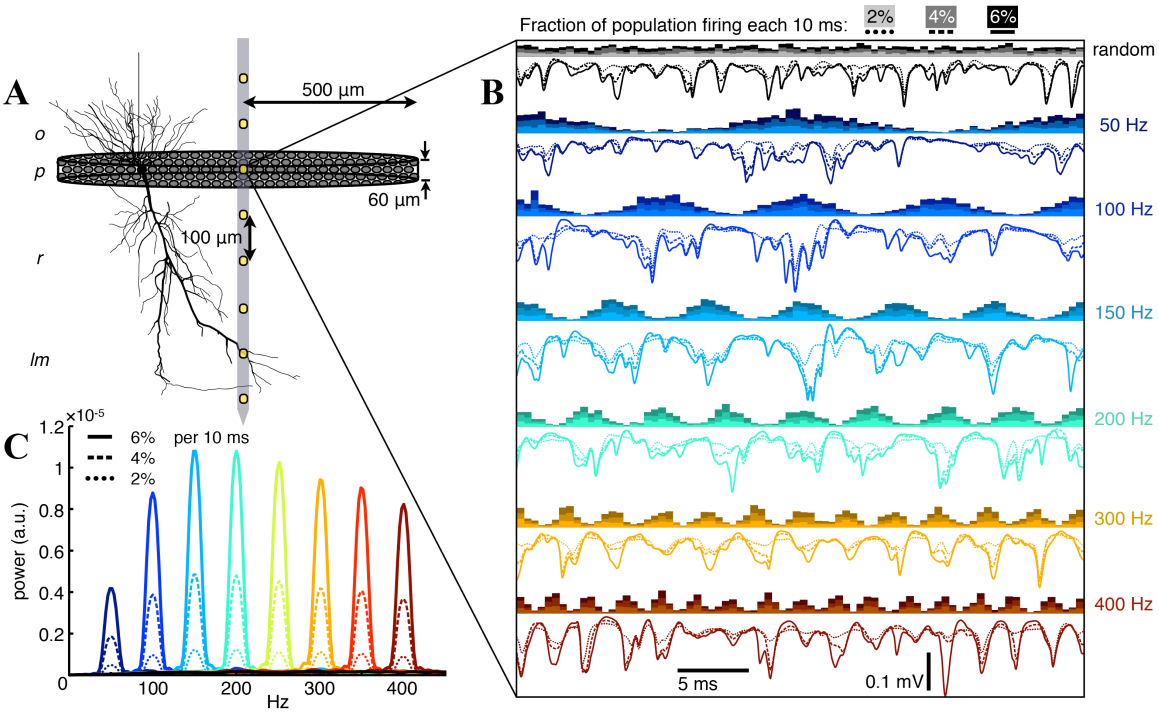

Figure 3.2. Extracellular signatures of phase-modulated spiking in a pyramidal cell population. ***A***, Illustration of the model. The 9416 pyramidal cells were randomly distributed with their soma centers in a 40-µm-thick circular disk with 1 mm diameter. V_e values were calculated along a virtual electrode shank oriented along the central axes of the disk. Layer abbreviations: o, Stratum oriens; p, stratum pyramidale; r, stratum radiatum; lm, stratum lacunosum-moleculare. ***B***, Extracellular potentials in stratum pyramidale arising from AP currents in randomly and rhythmically spiking populations with varying modulation frequency and three different average firing rates (2, 4, 6% per 10 ms). Histograms of APs are shown above the corresponding voltage traces. ***C***, Averaged FFT power spectra over 25 trials for V_e in stratum pyramidale. Spectra are shown for each case from *B* and for two additional frequencies (250 and 350 Hz). Note that the unmodulated spiking spectra (grayscale in *B*) are not visible because the maximum value in the most active case shown is 2.2×10^{-7}. Power spectral densities

(psds) throughout this manuscript were estimated using the multitaper method with a time-bandwidth product of 4 and an 8192-point FFT (Percival & Walden 1993), so the arbitrary psd units (a.u.) are consistent in all figures.

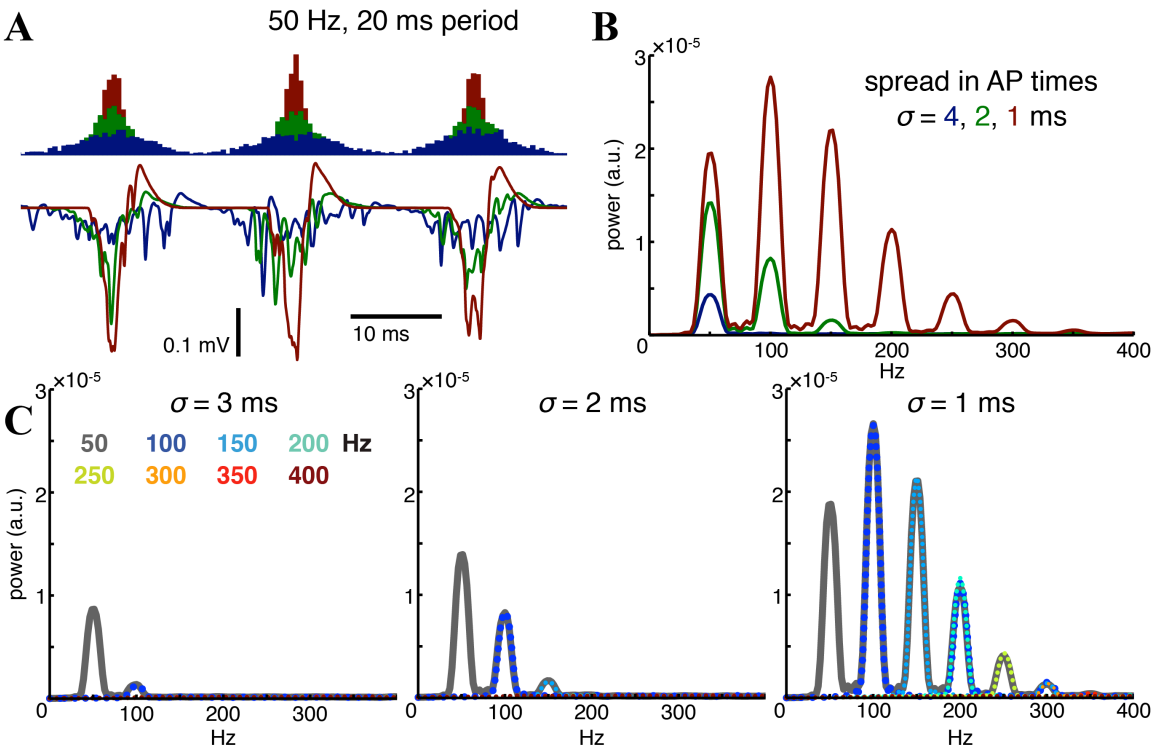

Figure 3.3. Effect of additional synchrony at slower oscillation frequencies. ***A***, Spike histograms and the resulting stratum pyramidale extracellular potentials for three different widths of the Gaussian-shaped bursts of spiking in the population [σ = 1 ms (red), 2 ms (green), 4 ms (blue)] during a 50 Hz rhythm. At low σ (high synchrony), the extracellular potentials essentially consist of periodically reoccurring population spikes. ***B***, The 25 trial averages of the FFT spectra of the extracellular potentials in *A*. Narrower population bursts increase power at both the rhythm frequency and its harmonics, with the power at the harmonics exceeding that at the rhythm frequency for very synchronous

spiking. ***C***, Average power spectra for 50 – 400 Hz rhythms in which the repeating Gaussian-shaped population bursts have widths of σ = 3, 2, 1 ms, independent of the oscillation. Six percent of the population fires each 10 ms with spike times modulated within the periodic probability density function. Faster rhythms therefore have these spikes separated into more bursts and, consequently, have fewer spikes per burst.

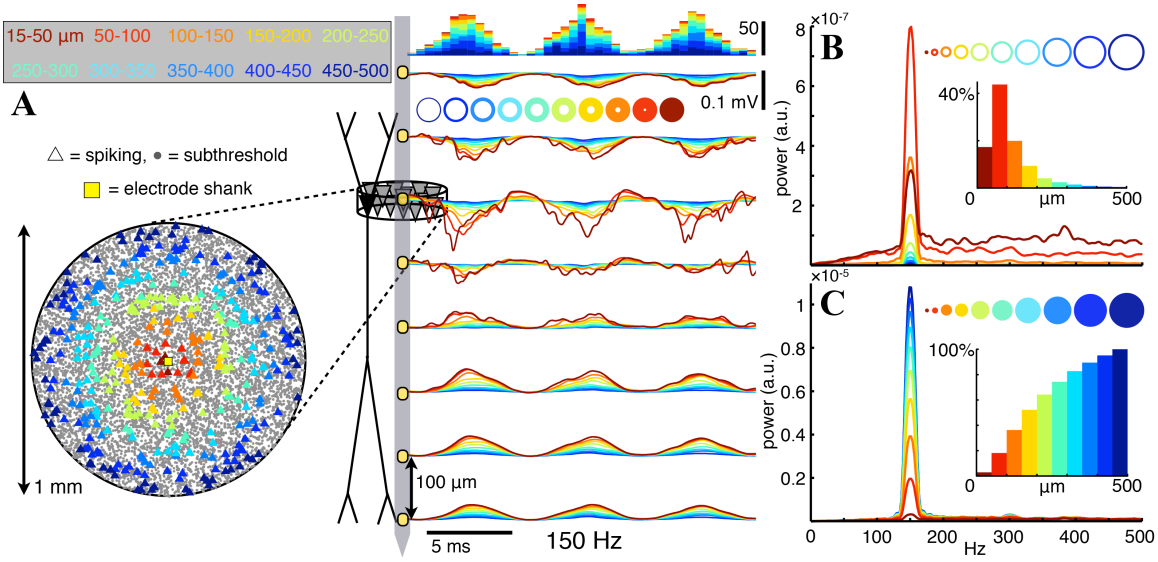

Figure 3.4. EAPs from groups of distant neurons can contribute substantially to fast LFP oscillations. ***A***, Extracellular potentials (right) along the stratum oriens–stratum radiatum axis in a rhythmically bursting population with 6% of the population firing each 10 ms. Spike bursts recur periodically at 150 Hz and have a Gaussian shape with σ = 1.3 ms (i.e., one-fifth of the oscillation period). The locations of neurons that spike during one 6.7 ms period are indicated by triangles in a top-down view of the pyramidal layer (left), with colors indicating the 50-µm-wide ring from which the spikes originate. V_e traces are colored correspondingly, with contributions from each ring of cells adding cumulatively

from the outside in. Stacked histograms above the potential traces show spike times. ***B***, ***C***, Averaged power spectra of the stratum pyramidale V_e from each individual ring (*B*) and for the inside-out cumulative potentials indicated by the colored disks (*C*). The insets indicate the proportions of the total 150 Hz power generated by each ring- or disk-shaped subpopulation (i.e., the peak values of the power spectra, normalized by the power at 150 Hz in the full population). Note that the contributions of the rings in *B* to the cumulative spectra in *C* do not sum linearly because we are displaying spectral power, which is proportional to the square of the amplitude.

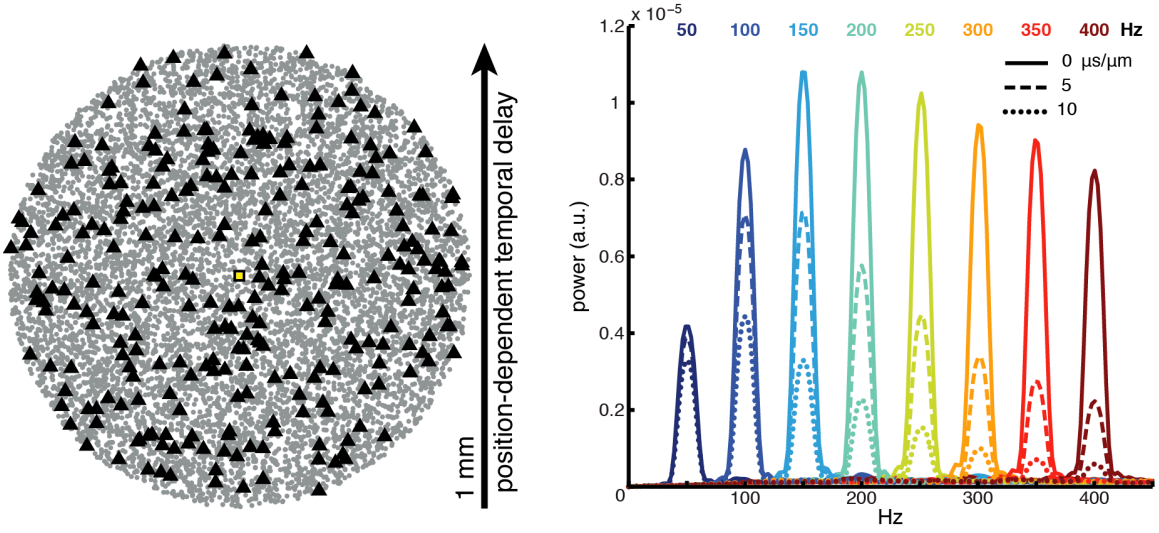

Figure 3.5. Effect of spatial synchrony on oscillatory potentials. *Left*, Locations of CA1 pyramidal cell somata within a 1-mm- diameter disk. The triangles show the location of cells spiking within a 5 ms interval (3% of the population). The temporal offsets of the periodic probability density function that modulates spike timing are shifted in a position-dependent manner along one dimension within the cell body layer, similar to the case in

which activity propagates along one direction in CA1 (Lubenov & Siapas 2009). *Right*, Average power spectra of V_e in stratum pyramidale over 25 trials with pyramidal neurons undergoing rhythmic firing, as in Figure 3.2, with varying levels of spatial synchrony. Color indicates the frequency of the firing rhythm, and line type indicates the time delay per unit distance of the oscillating spike probability function. Solid lines, 0 μs/μm (no delays); dashed lines, 5 μs/μm; dotted lines, 10 μs/μm.

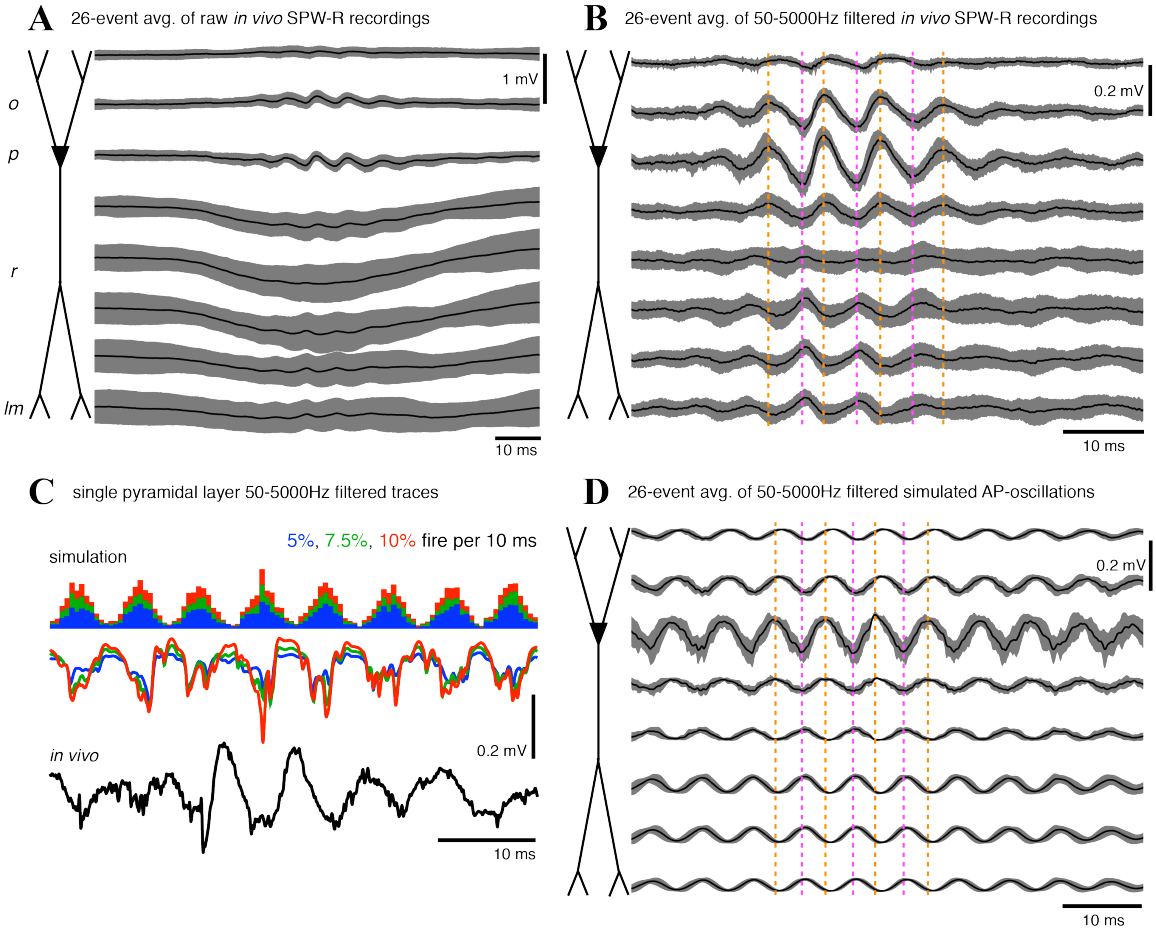

Figure 3.6. Simulated AP-generated ripples are characteristically similar to in vivo ripples. ***A***, Ripple-triggered average of wideband in vivo depth recordings (100 μm

electrode spacing) during 26 SPW-Rs with a dominant frequency between 140 and 160 Hz. Note the large variability in the SPW field potentials in the apical dendritic region, consistent with the ripple oscillation being generated locally, rather than driven by a coherent CA3 oscillation (Csicsvari et al. 2000). ***B***, Fifty to 5000 Hz bandpass filter applied before averaging the ripple events in *A*. The ripple is strongest in the pyramidal layer (Ylinen et al. 1995b), with a phase reversal 150-200 μm below (in stratum radiatum). The dashed vertical lines are visual aids for phase alignment. ***C***, Comparison of single representative stratum pyramidale voltage traces for simulated ripples consisting only of EAPs from a pyramidal cell population in which 5% (blue), 7.5% (green), or 10% (red) of the cells fire each 10 ms (spike histograms shown above voltage traces) and filtered in vivo ripple events (black). The firing probabilities are modulated by the same probability function as in Figures 5.2 and 5.4. ***D***, The 26 trial average of simulated EAP-generated ripples with frequencies set to the dominant frequencies measured during the in vivo ripple events of *A* and *B*.

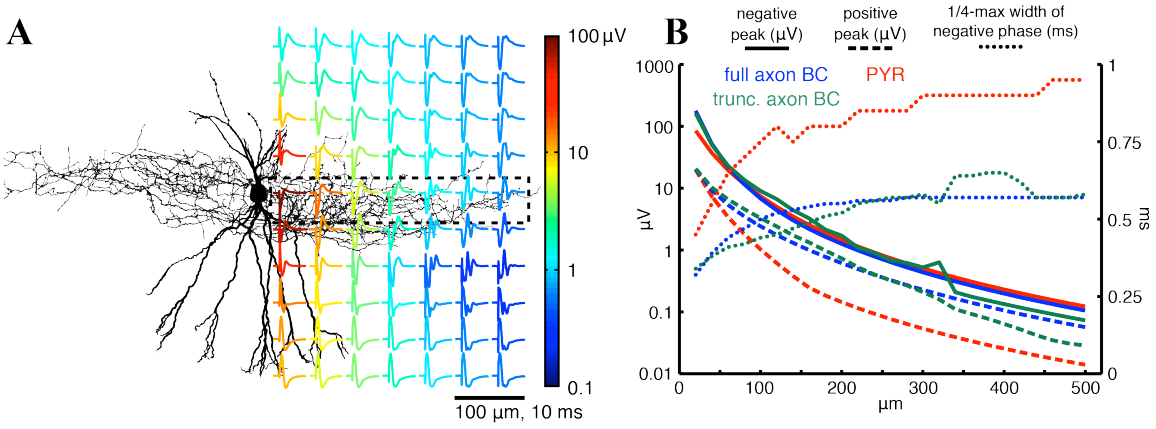

Figure 3.7. Spatiotemporal characteristics of basket cell EAPs. ***A***, Location dependence

of EAPs for the single basket cell model with peak-to-peak voltage range indicated by the color of each trace. As in Figure 3.1, subthreshold currents have been removed, and each trace is an average over 25 points at a fixed radius around the vertical dendritic axis. ***B***, EAP amplitude and width versus distance for the cell models: blue, pyramidal cell (PYR); purple, basket cell (BC); orange, basket cell with axon truncated at 68 µm. The amplitude of the negative (solid lines) and positive (dashed lines) peaks correspond to the left axis, and the width of the negative phase (dotted lines) corresponds to the right axis.

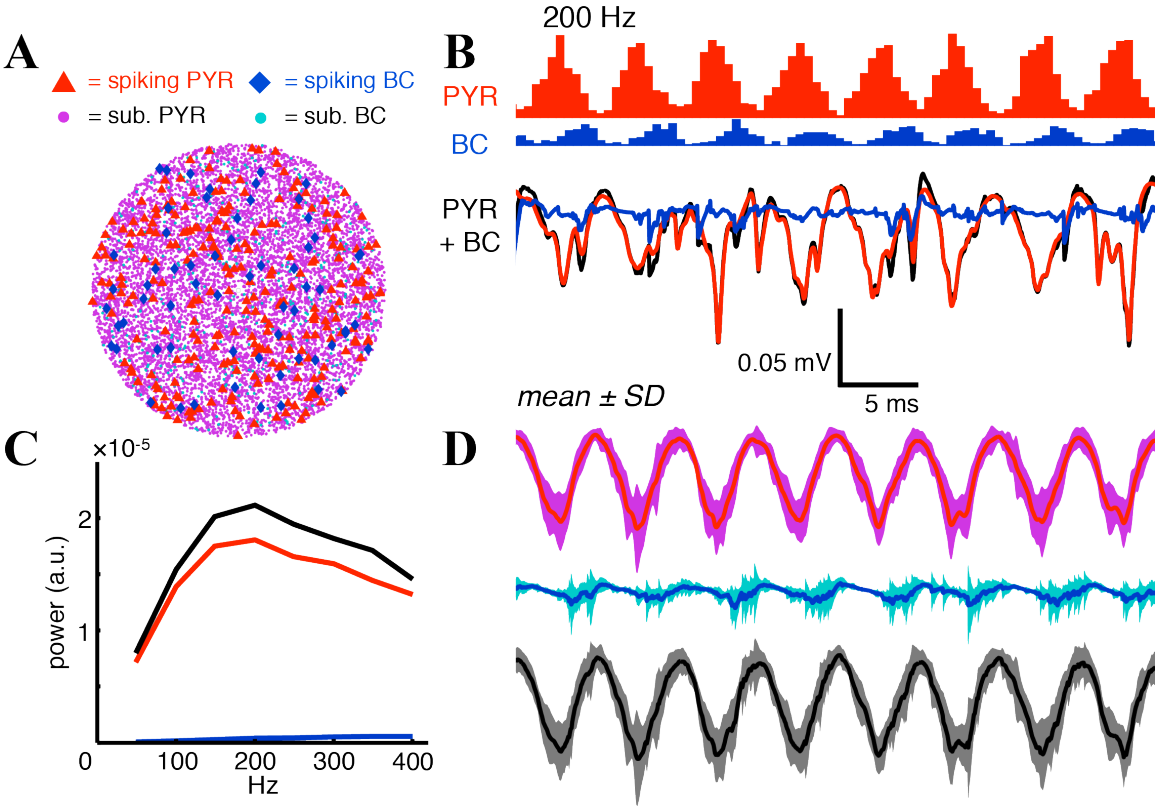

Figure 3.8. Basket cell EAPs contributed little to simulated ripple LFPs. ***A***, Locations of pyramidal cell (PYR) and basket cell (BC) somata within stratum pyramidale in a 1-mm-diameter simulated population. The small circles represent subthreshold cells, and the

larger triangles and diamonds represent cells spiking within one 5 ms period. ***B***, Spiking histograms and extracellular potentials from populations of pyramidal cells (red) and basket cells (blue) during 200 Hz rhythmic spiking with all synaptic driving currents removed, as well as the extracellular potential when both signals are combined (black). Here, basket cells are less numerous (5% of pyramids) but have five times higher average firing rates than pyramidal cells. Peak basket cell firing lags that of pyramidal cells by 90° (1.25 ms at 200 Hz) (Sullivan et al. 2011). ***C***, Spectral peaks of 25-trial-average FFTs of stratum pyramidale potentials from the separate (color) and combined (black) populations during rhythms from 50 to 400 Hz. ***D***, Mean ± SD for the potentials in *B* over 25 trials.

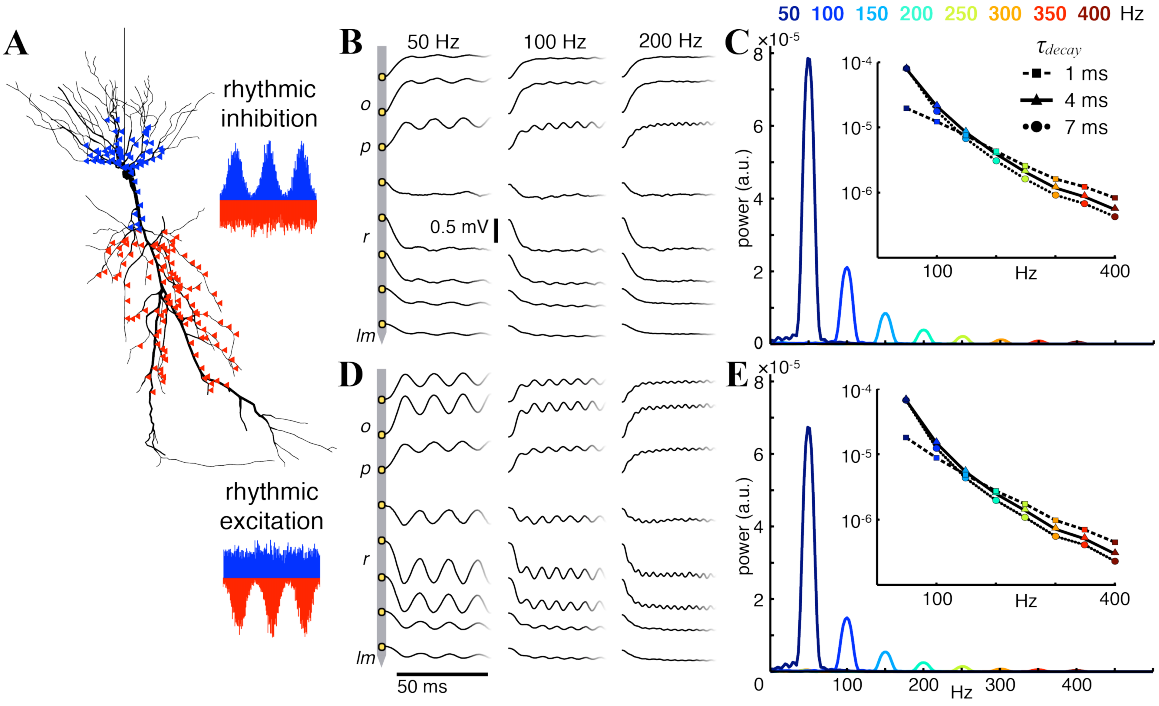

Figure 3.9. Simulation of extracellular potentials from synaptic input oscillations in a

passive pyramidal cell population. ***A***, 200 apical excitatory and 200 perisomatic inhibitory synapses are triggered each 50 ms, with the initiation times for one type (*B*, *C*, inhibitory; *D*, *E*, excitatory) modulated within a periodic Gaussian probability density function for $f = 50 – 400$ Hz in 50 Hz steps with SDs $\sigma = 0.2/f$, similar to the firing profiles in the rhythmically spiking population simulations. Synapses of the opposing type are activated with a constant probability. Both synapse types have $\tau_{decay} = 4$ ms. ***B***, ***D***, Example V_e traces for the 50, 100, and 200 Hz cases. ***C***, ***E***, Power spectra of *stratum pyramidale* V_e. Insets show the peak power values on a log scale for each oscillation frequency with τ_{decay} of the oscillating synapses varied from 1 to 7 ms.

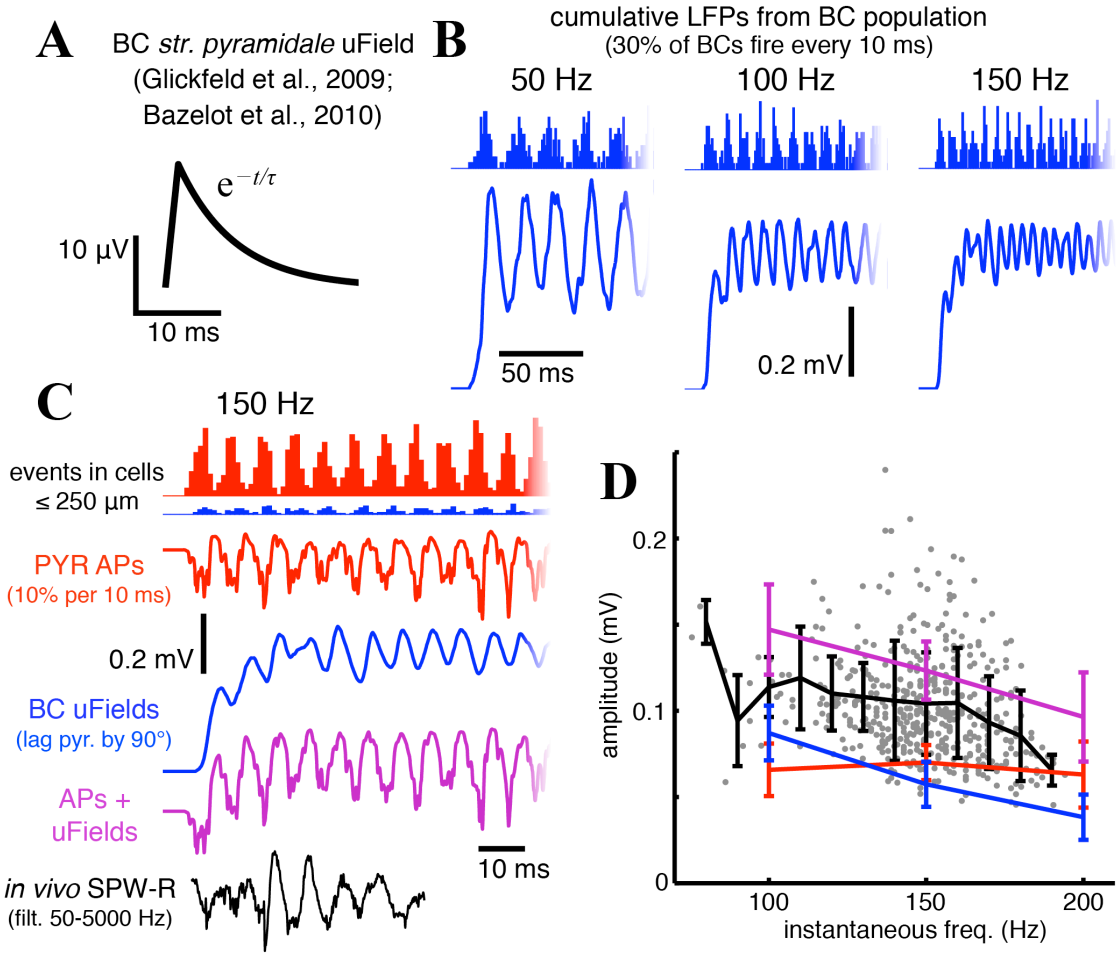

Figure 3.10. APs and IPSCs contribute similar amounts of power to 100 –200 Hz SPW-R LFPs. ***A***, uField in stratum pyramidale from a single basket cell (BC) spike, modeled after uFields measured by Glickfeld et al. (2009) and Bazelot et al. (2010). ***B***, Cumulative LFPs in a rhythmically firing basket cell population when the uField in *A* is added at the time of each spike for basket cells within 250 µm of the electrode contribute uFields; 30% of the population spikes each 10 ms. Histograms above the LFP curves indicate spike times. ***C***, Comparison of simulated LFPs from pyramidal cell EAPs (red) during a 150 Hz population rhythm with 10% spiking each 10 ms (as in Figure 3.6), basket cell uFields (blue), the two combined (magenta) with the basket cell spiking rhythm lagging

the pyramidal cell rhythm by 90° (Sullivan et al. 2011), and a 50 –5000 Hz bandpass filtered SPW-R recorded *in vivo* (black). The histogram shows all events occurring in cells within 250 μm from the electrode; the potentials include pyramidal cell EAPs from all cells within 500 μm and basket cell uFields from all cells within 250 μm of the electrode. ***D***, Comparison of amplitudes for *in vivo* and simulated ripples. The gray dots show instantaneous amplitudes and frequencies of individual troughs within in vivo fast oscillation events between 50 and 210 Hz, the black line marks the mean (±SD) trough amplitudes in 10 Hz bins of these *in vivo* ripple waves, and colored lines (same colors as in *C*) indicate mean (±SD) trough amplitudes during simulated ripples in populations oscillating at 100, 150, and 200 Hz.

III. Analyzing and interpreting multisite intracranial electrical recordings

4. High frequency signals, oscillations, and interactions in the hippocampal-entorhinal circuit

4.1 Introduction

4.1.1 Cross-frequency coupling and gamma coherence

Brain networks support a variety of oscillatory activity patterns over a wide range of time, frequency, and distance scales (Buzsáki 2006). Oscillations have been hypothesized to serve several computational purposes, such as clocking (Laurent 1996, Freund & Katona 2007, Moore et al. 2013), gating (Jensen & Mazaheri 2010), segmentation (Hasselmo et al. 2002, Buzsáki 2010), synchronization (Laurent 1996, Engel et al. 2001, Steriade 2006), desynchronization (Mizuseki & Buzsáki 2014), state maintenance (Jensen & Lisman 2005), among others. In addition, multiple oscillations, likely serving different functional roles, may co-occur and interact (Steriade 2006, Jensen & Colgin 2007). One of these forms of interaction, phase-amplitude cross-frequency coupling, is readily observed in hippocampal LFPs during theta oscillations (Bragin et al. 1995, Canolty et al. 2006, Colgin et al. 2009, Belluscio et al. 2012). The modulation of gamma power by theta phase in CA3, for instance, has been shown to increase in the rodent hippocampus during learning (Tort et al. 2009).

Differences in the theta modulation and interregional coherence of sub-bands of the broad the gamma frequency range, has led some authors to hypothesize a role for gamma oscillations in routing information flow through different parts of the hippocampal network. In support of this, Colgin et al. (2009) reported higher coherence in the fast gamma band (65-140 Hz) than the slow gamma band (25-50 Hz) between CA1 and layer 3 of the entorhinal cortex (EC3), with the opposite relationship between CA1 and CA3. High power events in the fast gamma band tended to occur near the trough of the CA1 stratum pyramidale theta wave, whereas the slow gamma events occurred earlier in the cycle, on the descending phase near the theta peak. Previous work has suggested that long-term potentiation (LTP) and depression (LTD) occurs on different theta phases (Pavlides et al. 1988, Orr et al. 2001, Hyman et al. 2003), inspiring models in which different theta phases serve differential encoding and retrieval roles (Hasselmo et al. 2002). Colgin et al. interpreted their data in this light, proposing that fast gamma events reflect encoding events coupled to EC3, and that slow gamma events herald memory recall initiated by CA3. Such a role for fast gamma oscillations is at odds, however, with several other findings regarding dendritic activation, synaptic plasticity, and the temporal ordering of input to CA1.

Specifically, the theta phase of maximal dendritic excitation arriving from EC3 is at the theta peak in CA1 stratum pyramidale (corresponding to the trough and a current sink in stratum lacunosum-moleculare, the site of the EC3-CA1 perforant path synapses) (Andersen et al. 1966, Holsheimer et al. 1982, Buzsáki et al. 1986, Brankack et al. 1993, Kamondi, Acsády, Wang, et al. 1998), which is separated from both maximal CA1

spiking (Fox et al. 1986, Mizuseki et al. 2009) and the strongest fast gamma power (Colgin et al. 2009, Belluscio et al. 2012) by around half a theta cycle (though note the asymmetry of the cycle; Leung 1984, Belluscio et al. 2012). A more complex profile of gamma band activity during theta oscillations was shown by Belluscio et al. (2012), and it was the medium gamma (60-90 Hz) signal that arrived at the proper phase and frequency (Chrobak & Buzsáki 1998) to correspond to entorhinal input. Furthermore, several studies have found that entorhinal input to CA1 has a weak and slow effect at the soma (Levy et al. 1995, Remondes & Schuman 2002, Jarsky et al. 2005), making it difficult to see how coherent fast oscillations would arise or be advantageous.

Chapter 3 showed that substantial amounts of power near 100 Hz can be generated by spikes in a population undergoing rhythmic changes in excitability around that frequency, and this band is generally susceptible to spectral contamination from spike waveforms (Zanos et al. 2011, Ray & Maunsell 2011a, Belluscio et al. 2012). In addition to the EC3 input, CA3 and CA1 can both generate intrinsic gamma oscillations in this band (Csicsvari et al. 1999b, Sullivan et al. 2011), meaning that afferent excitatory input, local inhibitory currents (but see Waldert et al. 2013), and local spiking activity all overlap in this spectral band. At low frequencies (<60 Hz), LFPs appear to reflect mostly synaptic currents, which can entrain neuron firing. At high frequencies (>150 Hz), LFPs are more indicative of local spiking activity. But the relationships, especially in this mid-frequency range, between the LFP and input (afferent synapses), local processing (synapses, membrane oscillations, dendritic spikes, etc.), and output (action potentials) are not well understood. Studies that pool LFP events within the medium/fast gamma and

epsilon frequency bands, and especially those that do not characterize the spatial structure of the LFP (e.g., when tetrodes or single wires are used), may therefore be combining multiple distinct processes into a single class of phenomena, obscuring the functional significance of each process.

An understanding of the neural dynamics within the hippocampal-entorhinal circuit is integral to understanding spatial coding and memory in the brain (Hartley et al. 2014), and so it is important to decipher the physiological correlates of the LFP signals measured in those regions. We sought to develop ways to detect, distinguish, identify, and characterize activities that contribute to the gamma/epsilon band in recordings from the dorsal hippocampus and medial entorhinal cortex in sleeping and behaving rats. We interpret our results in the context of the rodent hippocampal-entorhinal network, but many of the techniques and conclusions are applicable to other systems, as well.

4.1.2 Stepping back: what is a neural oscillation, anyway?

There are many well-studied examples of network oscillations in nature (Engel et al. 2001, Buzsáki 2006, Marder & Bucher 2007, Wang 2010, Vanrullen & Dubois 2011, Buzsáki et al. 2013), but considerable controversy still exists over the functional roles and importance of oscillations in brain networks. The first issue that needs clarification is precisely how one defines the term oscillation. What characteristics and dynamics must a system possess in order to be considered an oscillating system? In the case of the brain, which part(s) of the system are we referring to? In physics, an oscillating system is one in which energy is periodically transferred or converted between different components (e.g.,

between kinetic and potential energy in a pendulum). In neural populations, we generally conceive of oscillations as rhythmic changes in excitability, but we must decide if this refers to the excitability of an individual neuron's membrane, its spiking activity, or the spiking activity of the population as a whole. It is also plausible that the measured variable, such as the LFP, could exhibit periodic fluctuations due to variation in synaptic currents in the distal dendrites, but these fluctuations might not propagate to the soma. In this case the neurons near the recording site would not actually be oscillating individually, though, as a whole, they or an afferent population could be.

Detecting an oscillation is often not straightforward. LFPs are generated by a complicated mixture of sources subject to numerous biophysical filters in the conversion of neuronal activity to measured voltage (Einevoll et al. 2013), and they can be poor indicators of local spiking (Mitzdorf 1985). It is important to assess whether spiking activity is rhythmically modulated by the oscillating variable, as well as confirm that the source is local (e.g., using appropriate current source density analysis to exclude volume conducted currents as the cause of an LFP signal). Spectral leakage from broadband changes in power associated with spiking (Manning et al. 2009, Ray & Maunsell 2011a) or harmonics of lower frequencies (Leung et al. 1982, Buzsáki et al. 1983, Montgomery et al. 2008) can lead to spurious power increases and phase locking of spikes . Ideally, we could do away with using the LFP altogether and measure spikes and membrane potentials across the population directly (Quian Quiroga & Panzeri 2009). While recording technologies are approaching this point (Buzsáki 2004, Ahrens et al. 2013, Chen et al. 2013), it is still rare to obtain sufficient simultaneous unit count, recording

duration, and temporal resolution to confidently assess the presence or absence of transient oscillatory dynamics using spikes alone (Mureşan et al. 2008).

We recorded in CA1 and CA3 of the hippocampus and layers 2-5 of the dorsocaudal medial EC, then applied a combination of methods across a wide range of frequencies, including independent component analysis (ICA) and cross-frequency coupling (CFC) measures in the LFP, spike-field coherence, and spike train correlations. Consistent with previous reports, we found that gamma power in the LFP of each region was modulated by the theta rhythm, with multiple distinct frequency bands in CA1 stratum pyramidale emerging at different phases of the theta cycle. The gamma sub-bands corresponded to the activation of different neuron populations throughout the circuit, reflecting both afferent synaptic input and local processes. Single units detected in each region were phase-locked to the LFP gamma patterns in different ways. Interneurons in CA1 displayed a heterogeneous spike-field coherence profile, with subpopulations preferring different gamma sub-bands of the LFP. CA1 pyramidal cells, however, were modulated poorly or not at all by the phase of afferent gamma rhythms. When compared to LFPs in their own region (i.e., at another site in stratum pyramidale 400 μm away), they were most strongly modulated high frequencies (140-160 Hz) in a way that was not explainable by simple spike contamination. The medium-fast gamma coherence (weak, but significant) between the CA1 LFP and LFPs recorded from its afferent regions therefore did not indicate that the principal cell populations were coupled at gamma frequencies. The timing of EC3-CA1 interactions was instead more consistent with

models of hippocampal function that exploit longer timescale mechanisms for dendritic activation, synaptic modification, and coordination of entorhinal and CA3 input.

4.2 Methods

4.2.1 Descriptions of the data sets

We analyzed recordings from electrodes implanted chronically in the right dorsal hippocampus and dorsocaudal medial entorhinal cortex (EC) of behaving and sleeping rats (male Long-Evans, 250-400 g). Three animals had one 4-shank probe in EC and one 4- or 8-shank probe in hippocampus, oriented along the septotemporal axis (Mizuseki et al. 2009). Shanks were separated by 200 μm, and each shank had 8 staggered contacts with 20 μm vertical spacing. Three animals had one probe in CA1 and one in CA3, both in the left hemisphere (Diba & Buzsáki 2007, 2008). One animal had a 256-site array (8 shanks separated by 300 μm, 32 sites per shank, linearly arranged with 50 μm spacing) implanted the transverse plane of the right dorsal hippocampus (Berényi et al. 2014). In all cases, two stainless steel screws in the skull above the cerebellum were used as indifferent and ground electrodes during recordings.

Data were recorded during sleep or behavior at either 32.552 kHz or 20 kHz. For LFP analysis, data were downsampled to 1252 Hz or 1250 Hz, respectively. For unit analysis, signals were high-pass filtered (>0.8 kHz) for offline spike detection and sorting. Behavioral tasks included running on a linear track for water reward, retrieving water or food on large and small square platforms, rewarded wheel-running, and delayed alternation between arms on a T-maze for reward (Diba & Buzsáki 2007, Pastalkova et al.

2008, Mizuseki et al. 2009, Berényi et al. 2014). Recordings were also made during rest/ sleep in the home cage preceding and following behavioral trials.

Spikes were detected and clustered semiautomatically from the digitally high-pass filtered signal (0.8–5 kHz) and automatically sorted using KlustaKwik (Harris et al. 2000), followed by manual adjustment of the clusters using the Klusters software package (Hazan et al. 2006). Putative pyramidal cells and interneurons were separated on the basis of their autocorrelograms, waveforms, and mean firing rates (Bartho et al. 2004, Mizuseki et al. 2009). EC layers were identified by the reversal of ripple-triggered sharp waves (Chrobak & Buzsáki 1996) and reversal of theta waves (Alonso & García-Austt 1987, Chrobak & Buzsáki 1998, Hafting et al. 2008), assisted by histological verification of the recording tracks (Mizuseki et al. 2009).

Theta periods were detected automatically using the ratio of the LFP power in theta band (5- 11 Hz) to the power of nearby bands (1-4 Hz, 12-14 Hz), followed by manual adjustment with the aid of visual inspection of whitened power spectra. Theta epochs during walking/running were classified as RUN, and those during sleep were classified as REM, with non-REM sleep periods classified as slow-wave sleep (SWS).

4.2.2 Independent Component Analysis

The analysis of in vivo hippocampal LFPs with independent component analysis (ICA) has been described and validated by Makarov et al. (2010) and Fernández-Ruiz et al. (2012). We used the infomax algorithm initially proposed by Bell and Sejnowski (1995) and implemented in the EEGLAB Matlab toolbox (Delorme & Makeig 2004). The

routine returns the activations $s_n(t)$ and the spatial weights $V_{i,n}$ of the same number of components ('generators') as input channels (32 in our case). In the case of hippocampal LFPs, only a few generators have significant amplitude and distinct spatial distributions in the hippocampus (Korovaichuk et al. 2010). Once LFP generators have been extracted from the raw LFPs, they can be analyzed as if they alone were active (Fernández-Ruiz & Herreras 2013).

4.2.3 Theta phase estimation

Unless otherwise noted, we used the middle of the CA1 pyramidal layer (determined using ripple power; Mizuseki et al. 2011) as the theta reference. When multiple CA1 stratum pyramidale sites were present, we took the angular mean of their individual phases. 0 and 360 degrees refer to the waveform peaks, 180 degrees to the troughs. To determine the theta phase, two separate methods were employed: (1) the phase of the analytic signal given by the Hilbert transform of the theta bandpass-filtered (4-12 Hz) LFP; (2) the linearly interpolated phase between maxima and minima in each theta cycle of the 1-60 Hz bandpass filtered LFP (Belluscio et al. 2012). The intervals in which to detect extrema were determined using zero-crossings of the narrowband-filtered (4-10 Hz) signal.

4.2.4 Spectral analysis

To assess spectral events at a high resolution in time and frequency, we calculated the complex wavelet transform (CWT) of the LFP with the Wavelet Toolbox in Matlab.

We used complex Morlet wavelets with 9 waves of decreasing amplitude from the central peak, the fourth from the center being ~4% of the central peak's height ('cmor5-1' in Matlab). These were scaled in a logarithmically spaced manner from 20-240 Hz in 28 steps. The CWT gives an amplitude and phase measure for each wavelet scale at all time points in the data, obtained by convolving the real and imaginary parts (which are out of phase by 90 degrees) of the wavelets with the data vectors.

The theta modulation of the LFP spectrum was calculated by binning time points into theta phase intervals (see Section 4.2.3) and taking the mean amplitude of the CWT at each frequency for each phase bin. To compare changes across frequencies, CWT amplitudes were normalized by the mean and standard deviation (z-score) at each frequency for the epochs of interest. The modulation index (MI) between the CWT amplitude and theta phase was assessed using the weighted circular mean of the amplitude distribution across phases (Canolty et al. 2006). Significance was assessed with the distribution of MI values for a set of surrogate amplitude and phase vectors that were shifted with respect to each other by randomly chosen temporal offsets (Canolty et al. 2006).

The phase-locking of unit spikes to LFP features at each frequency was measured using CWTs at the time of each spike. Two methods were tested, both of which produced similar results. (1) If the CWT amplitudes were ignored, the modulation indices for each frequency were calculated using the length of the mean phase vector, and significance was estimated using the Rayleigh test for non-uniformity (Berens 2009). (2) The CWT amplitudes could be incorporated as weights in calculating the mean phase vector. This

has the desirable property that times of higher power at a given frequency count more towards the modulation index. In this case, however, the Rayleigh test is no longer appropriate for estimating significance. We instead compared the MI to the distribution of MI values of surrogate spike phases following random temporal shifting of the spike trains relative to the CWTs. [This surrogate testing was very computationally intensive, and a more efficient alternative would instead be to implement Moore's modification of the Rayleigh test (Moore 1980).]

Single units may "prefer" a particular frequency of the LFP, but fail to fire in a phase-locked manner in relation to it. We therefore also calculated the mean z-scored CWT amplitudes for the spike times of each unit. The strength and significance of the relationships between spikes and power at each frequency would be best assessed through surrogate analysis, but we have not yet run these calculations.

Average LFP power and coherence spectra were calculated with Welch's power spectral density method (the *pwelch()* and *mscohere()* functions in the Matlab Signal Processing Toolbox). We used a 4096-point FFT, applied to up to 10 minutes of data in the epochs of interest (or as much as was available if less than 10 minutes of this state occurred during the recording). To estimate significance thresholds for coherence, the same calculations were performed 200 additional times after randomly shifting (by 1 to 30 seconds) one of the LFP data vectors (in a circular fashion) with respect to the other.

4.2.5 Cross- and Auto-correlations

The cross-correlogram (CCG) of a pair of single units was calculated by placing spikes into 0.8 ms bins (the LFP sampling rate) and convolving the resulting spike count vectors, up to a maximum time lag of 500 ms. To obtain the multiunit CCG (mCCG) for a given population of single units or between two different populations, we used the following procedure. First, the unnormalized CCG between each pair of units in a recording was computed. Then, for each category of unit pair (detection region and putative cell type, i.e., pyramidal or interneuron), the CCGs were summed with a consistent pre and post ordering. In the case of unit pairs of the same category, only pairs from different sites were included (because an artificial dip at zero lag was introduced by the inability to detect multiple spikes at the same time and location), and each pair was included only once. By summing the unnormalized single unit CCGs, units with more spikes have greater influence over the multiunit CCG. On the other hand, summing normalized single unit CCGs (Csicsvari et al. 2003) amplifies noise from low-firing units. The best method may be to sum normalized pairs that exceed a spike count threshold, but we have not yet explored the optimal threshold. The results presented here are for summed unnormalized CCGs.

4.3 Results

4.3.1 Cross-frequency coupling: theta-modulation of fast oscillations

The occurrence and/or amplitude, as well as the frequency, of gamma oscillations in the hippocampus were biased by the phase of the concurrent theta oscillation (Bragin

et al. 1995, Chrobak & Buzsáki 1998, Colgin et al. 2009, Belluscio et al. 2012). After calculating time-resolved wavelet-based spectra of LFP recordings (Section 4.2.4), we measured how the power in each frequency band depended on the theta phase estimated from the CA1 stratum pyramidale LFP (Section 4.2.3). In CA1, slow gamma (25-50 Hz) power was concentrated at the descending phase of theta, medium gamma (60-100 Hz) at the peak of theta, and epsilon (100+ Hz, also often called "fast" or "high" gamma) at the trough of theta (Figure 4.1). Some previous studies have proposed potential sources and functions of these sub-bands (Colgin et al. 2009, Ray & Maunsell 2011a, Belluscio et al. 2012, Scheffer-Teixeira et al. 2013), and we sought to further decipher their origins and their coordination within the hippocampal-entorhinal circuit.

Most of the excitatory synaptic input to CA1, which impinges on the pyramidal cell dendrites (Megías et al. 2001) and generates the strongest current dipoles generating extracellular potentials (Buzsáki et al. 1986), arrives from CA3 and layer 3 of the entorhinal cortex (EC3) (Andersen et al. 2007). The EC3 network was most active near the theta peak (Figure 4.2; Mizuseki et al. 2009), which was also the phase at which most of its gamma power is concentrated (Figure 4.1). EC3 gamma oscillations are in the medium-fast frequency range (Figure 4.1; Chrobak & Buzsáki 1998). EC3 is therefore the most likely cause of the medium gamma power in CA1 at the theta peak. CA3 exhibits slow gamma oscillations (Figure 4.1; Bragin et al. 1995), and most of its spiking activity occurred on the descending phase of CA1 theta (Figure 4.2; Mizuseki et al. 2009), which makes it the best candidate for causing the slow gamma power in CA1 at this theta phase. The high-frequency power (>90 Hz) near the theta trough coincided with

the highest rate of firing across the pyramidal cell population. This band most likely reflects some combination of broadband spectral leakage of spikes into the gamma range (Zanos et al. 2011, Ray & Maunsell 2011a, Belluscio et al. 2012), coordinated IPSCs within the highly active CA1 network (CA1 interneurons also fire a great deal at this phase), and coordination of the pyramidal cell spikes (Schomburg et al. 2012).

These conclusions are further supported by the network activity changes from awake theta (RUN) to the theta oscillations during REM sleep. REM sleep has also been called "paradoxical" sleep because of the very similar electroencephalographic characteristics during the two states (Jouvet 1967). The hippocampal formation exhibits robust theta oscillations during both states, but important differences do surface in detailed characterizations of network activity (Montgomery et al. 2008, Mizuseki et al. 2011). Compared to RUN, except during brief bouts of "phasic REM" (Montgomery et al. 2008), the CA3 pyramidal cells had lower firing rates during REM, whereas the entorhinal population, including pyramidal cells in EC3, was more active (Figure 4.3; Mizuseki & Buzsáki 2013). There was also less powerful slow gamma in CA3 and more powerful medium-fast gamma in EC3 (Figure 4.1). The CA1 interneurons (limited here to those near the pyramidal layer), many of which receive powerful input from CA3 (Gulyás et al. 1999), were less active (Mizuseki & Buzsáki 2013). As a consequence of these changes, the CA1 pyramidal population as a whole maintained similar firing rates, but many of them shifted their firing to the peak of the CA1 theta LFP (Mizuseki et al. 2011), coinciding with the arrival of the strongest EC3 input.

Along with these changes in the afferent and local spiking activity (Figure 4.3), the descending-phase slow gamma was dramatically reduced during REM compared to RUN (Figure 4.1). Following local CA1 spikes, epsilon power became biphasic, increasing at both the theta peak and theta trough (Figure 4.1). Finally, medium gamma power showed a stronger increase at the theta peak during REM compared to RUN, which likely corresponded to both stronger medium-fast gamma input from EC3 and broadband power increases accompanying the greater firing rates at this phase.

4.3.2 CSD and ICA decomposition of LFP generators

The origins of these gamma-band LFP signals were further elucidated by techniques designed to extract source information from linear array recordings. We employed independent component analysis (ICA) to separate LFP components generated by distinct synaptic pathways. ICA is a technique for blind source separation (Comon 1994) and is well-suited for application to LFPs (Makarov et al. 2010, Fernández-Ruiz & Herreras 2013). It is a method of dimensionality reduction that seeks maximally independent components, a more relevant goal in the context of neurophysiology than that of other techniques such as principal component analysis (PCA). The most common ICA algorithms operate by maximizing the joint entropy of the components (Bell & Sejnowski 1995), which is equivalent to minimizing their mutual information. If the resulting components are to correspond to physically meaningful sources, the sources must satisfy the following conditions. (1) For the most part, distinct sources must be activated independently. The technique can deal with some degree of correlated activity,

but this may result in some degree of cross-contamination (Makarova et al. 2011). (2) The spatial profiles should differ between sources, and (3) they remain constant throughout the record. The depth profile of hippocampal LFPs satisfies these criteria relatively well, given the well aligned pyramidal cells and the laminar structure of synaptic projections from afferent regions. (4) The sources should be non-Gaussian in their activations (Bell & Sejnowski 1995), which happens to be a signature feature of brain dynamics (Mizuseki & Buzsáki 2013).

We applied ICA to LFPs recorded from large silicon multielectrode array implanted in the hippocampus of behaving and sleeping rats. The algorithm takes a time series of data with dimension equal to the number of channels, and returns a time series of the same dimensionality, but rotated such at each dimension represents a different 'independent component'. In the context of LFPs, we refer to the components as generators (Makarov et al. 2010). The inverse of the mixing matrix that transforms the LFP data into the generators gives the channel weights of the generators, which correspond to their spatial profiles. We can estimate the relative contribution of each generator to the original (total) LFP data by comparing their back-projected variances. (The largest variance components produced by ICA often have low variances compared to the first few PCA components, as the purpose of ICA is to maximize the independence of components rather than their explained variance.)

The results shown here are for an 8-shank probe with 32 sites per shank, with shanks oriented vertically and covering a transverse section of the dorsal hippocampus (as in Figure 2.3, top panel). Theta oscillations dominate LFP power and are coherent

across the hippocampal formation, but gamma band currents are much more local and independent (Montgomery et al. 2008, Sabolek et al. 2009). By high-pass filtering above 30 Hz (i.e., above theta and its first few harmonics), we were able to extract stable and consistent generators across multiple shanks that were broadly similar to previously characterized generators that correspond to distinct synaptic sources (Makarov et al. 2010, Fernández-Ruiz et al. 2012). Their spatial profiles matched that expected of the synaptic currents elicited by activation of stratum radiatum (RAD), stratum lacunosum-moleculare (SLM), and perisomatic (SOM) synapses (Figure 4.4 A-C). Generators of the same type extracted from different shanks exhibited much greater gamma band (30-100 Hz) coherence than generators of different types, whether from the same or different shanks (Figure 4.4D), and this coherence between like generators decayed monotonically with the separation between them (Figure 4.4E). (Note, however, that low cross-generator coherence is, to a large degree, enforced by the ICA algorithm.)

We next analyzed the power spectra and CFC of each ICA-derived generator's activity. As expected, the RAD generators, which exhibited strong modulation of slow gamma by ongoing theta oscillations, with maximal slow gamma power on the descending phase of CA1 stratum pyramidale theta. Gamma power in the SLM generators was best modulated around 90-100 Hz, with the maximum occurring at the theta peak. The SOM picture was less clear, and this generator did not serve to complete a tripartite explanation of the CA1 gamma bands. It instead behaved similarly to the RAD generator, showing strong gamma modulation that was maximal during the descending phase of theta during both RUN and REM (Figure 4.5). As evidenced by the pyramidale

layer LFPs, a great deal of signal mixing occurs in the perisomatic region. The higher power of lower frequencies, as well as temporal correlations of feedforward excitation and inhibition from CA3 (Sections 4.3.4 and 4.3.5; Zemankovics et al. 2013), may prevent ICA from cleanly separating the gamma sub-bands into exactly three distinct generators (Makarova et al. 2011).

4.3.3 LFP coherence

Rather than attempting to decompose the LFP in one region into its localized sources (the goal of CSD and ICA techniques), a different approach is to measure interactions between LFPs (this section) and units (the following two sections). For RUN, REM, and SWS epochs, we calculated the average Fourier coherence spectra between LFPs recorded in different regions, as well as for surrogate data with random temporal shifts between the compared vectors. Low frequencies were likely affected more by volume conduction, and additional broadband, high-frequency coherence was present during RUN epochs, reflecting some amount of muscle-related signal contamination, which we did not attempt to remove from the data (see Chapter 5). Some channels also contained 60 Hz line noise (and/or its third harmonic at 180 Hz; dashed vertical lines in Figure 6).

All channel pairs had significant theta coherence, so we show only frequencies >20 Hz. To a large degree, however, the coherence reflected previous findings and known anatomical connectivity (Figure 4.6). CA1 LFPs were highly coherent with other CA1 sites, with increases from 100-200 Hz during SWS due to sharp wave-ripples (SWRs)

(Buzsáki et al. 1992). Slow gamma dominated CA1-CA3 coherence, though it decreased from RUN and REM, matching changes in CA3 firing between these states (Figure 4.3). CA1-CA3 coherence from 70-100 Hz was higher during SWS due to fast gamma bursts in CA3 (Csicsvari et al. 1999b). Some slow gamma coherence between CA1 and EC3, as well as EC5 but not EC2, was present during RUN, reflecting the connectivity of these layers with CA1. CA1-EC3 gamma coherence increased during REM, including a peak around 100 Hz. Weak, but significant, coherence between CA1 and EC2 also arose during REM, likely due to coherence and/or volume conduction between EC2 and EC3. Significant ripple-band coherence between CA1 and EC5 appeared during SWS.

In addition to average coherence during RUN or REM epochs, we sought to detect how the coherence depended on the phase of the theta cycle. Using the continuous wavelet transform to calculate the instantaneous phase at each frequency, we calculated the mean wavelet coherence between LFPs at different sites in each theta phase bin. Because the wavelet phase estimation for a given frequency will be affected by the amplitude of that frequency component compared to others at the same time, we did expect to see some modulation in coherence result from the power modulation (Figure 4.1). Aside from this caveat (as well as some 60 Hz line noise), the gamma coherence between CA1 and another CA1 site, a CA3 site, and an EC3 site did depend on theta phase (Figure 4.7). Slow gamma coherence between CA1 and CA3 was highest during the descending theta phase of RUN theta, but remained lower and was less modulated during REM. In addition, some medium/fast gamma coherence appeared near the theta trough, around the time of the most overlap between CA1 and CA3 firing increases

(Figure 4.2). Entorhinal coherence values were quite low, but the medium/fast gamma coherence that did emerge occurred near the peak of REM theta, which is when it is most powerful in EC3. This was also the phase of the strongest medium/fast gamma coherence between CA1 sites during REM, perhaps reflecting this common input source, as opposed to more local inhibition and spiking.

4.3.4 Unit correlation and coherence with LFP spectral features

The LFP is a complicated mixture of currents from a variety of sources, with synaptic currents predominating at low frequencies, and so it is not necessarily a good indicator of how the local network is coordinated. We wished to more directly gauge how well these LFP signals reflected afferent and local spiking activity, and conversely, how well the oscillating synaptic currents reflected in the LFPs entrained spikes in CA1. Previous studies have reported varying degrees of network phase-locking to different spectral bands. The frequency intervals chosen for these bands, however, usually arise from a combination of tradition and somewhat subjectively defined deviations from the expected power spectrum of the LFP (i.e., a monotonic and smooth decay as frequency increases). We therefore measured the phasic modulation of each unit's spikes by the instantaneous LFP phase estimates across a wide range of frequencies, without preselecting particular frequency bands or power thresholds. This produced a measure of the frequency scales at which features of the LFP contained information about the timing of single unit spikes.

To measure power and phase across a broad range of frequencies throughout the recording, we calculated the continuous wavelet transform (CWT) of the LFPs using complex Morlet wavelets scaled logarithmically from 20-240 Hz (see Section 4.2.4). This allowed us to estimate the instantaneous power and phase at the times of single unit spikes, and deviations from uniform phase distributions could then be quantified. We found that putative CA1 pyramidal cell spikes were moderately phase-modulated by slow gamma fluctuations in CA1 stratum pyramidale LFPs recorded 0.4 mm from the unit detection site. These units were poorly modulated by medium gamma LFP features, and were best locked to LFP fluctuations at 140-150 Hz (Figure 4.8). However, while this frequency lies within the ripple band, clear signs of sustained oscillations were not present in the unit spike trains (Section 4.3.5), in contrast to during SWS, when SWRs are frequent (Figure 4.14).

The conspicuously low phase modulation of CA1 pyramidal cell spikes by slow-medium gamma stands in contrast to broad phase-locking of CA1 interneurons (Figure 4.9), as well as the modulation of both principal cells and interneurons in CA3 and EC3 by gamma frequency LFPs recorded within their own respective regions (Figure 4.8 and 4.9). Substantial subgroups of these neuron populations exhibited frequency preferences in the slow, medium, and fast gamma bands, corresponding to similar portions of the LFP power spectra that were coupled to theta phase (Figure 4.1). Specifically, most of the significantly modulated CA3 pyramidal cells preferred slow gamma frequencies recorded from CA3 stratum pyramidale, whereas EC3 pyramidal cells preferred fast gamma frequencies between 100-130 Hz. In general, the interneuron populations were more

broadly tuned than pyramidal cells, with some subpopulations preferring frequencies to which few pyramidal cells were locked (e.g., CA1 interneurons preferring 70-100 Hz fluctuations in CA1 stratum pyramidale).

A recurring problem in neuroscience is to understand which neural activities are reflected in LFP recordings, which are generated by a complicated and variable mix of membrane currents in the vicinity of the electrode (Buzsáki et al. 2012). At frequencies above ~80 Hz, spikes begin to impart significant power to the LFP recording (Ray & Maunsell 2011a, Belluscio et al. 2012, Waldert et al. 2013), especially when their timing is coordinated (Schomburg et al. 2012). By inspecting the phase locking of neurons to LFPs across regions, we found some explanations, as well as new puzzles. For example, EC3 and CA3 units were better locked to CA1 medium gamma frequencies than CA1 pyramidal cells, indicating that these neuron populations, which project to region CA1, are more directly responsible for CA1 LFPs in this frequency band. CA3 pyramidal cells, however, locked poorly to slow gamma phase in CA1 stratum pyramidale, despite prominent CA3 network oscillations in this frequency band (Figures 4.1 and 4.6; Csicsvari et al., 2003). Most of the CA3 to CA1 projections run through the Schaffer collateral pathway and terminate in CA1 stratum radiatum (Li et al. 1994). When compared to LFPs located closer to these projections (i.e., within stratum radiatum, but still close to the pyramidal layer because of small vertical span of the probe), CA3 pyramidal cells were better modulated by the slow gamma phase (Figure 4.10). CA1 pyramidal cells were also better modulated by radiatum slow gamma than in stratum pyramidale. As it turned out, slow gamma oscillations in stratum radiatum LFPs did not

consistently transfer to stratum pyramidale (Montgomery et al. 2008), which helps to explain the poor phase locking of units to this band in stratum pyramidale. However, the large reduction in phase modulation for CA3 units and the appearance of an 80 Hz frequency preference for many of these units, which represents a low point in the phase locking of CA3 units to their own LFPs, still presented a conundrum. One possible explanation is the correlated firing the CA1 interneurons which also lock to this 80 Hz band (Figure 4.10). This subpopulation of putative interneurons was more likely to exhibit monosynaptic timescale increases in firing following spikes of at least one of the CA3 pyramidal units (23% of pairs significant vs. 17% of all pairs; $p < 0.01$ after shuffling pair identities). CA3 units that locked to 80 Hz in CA1 were also more likely to 'monosynaptically' excite (direct monosynaptic connections cannot be confirmed with these recordings) CA1 interneurons (32% significant pairs vs. 17%, $p < 0.001$), and putative monosynaptic connections were more likely between the CA3 pyramidal units and CA1 interneurons when *both* preferred 70-100 Hz frequencies in CA1 stratum pyramidale than when *either* of them did (38% vs. 24%, $p < 0.05$). Therefore, these driven interneurons may add a second wave to the LFP with their IPSCs, which would ride on top of the EPSCs evoked by the CA3 input. Spike train cross-correlograms (Section 4.3.5) also showed 80 Hz rhythmicity for CA3 units, and the coherence analysis of Section 4.3.3 indicated the presence of 80 Hz coupling between CA3 and CA1. It could also be that the CA1 interneurons amplify these medium gamma frequencies in the perisomatic LFP more than slow gamma.

In support of the CA1 interneurons causing this discrepancy, the CA1 and CA3 subpopulations that locked to 80 Hz in CA1 stratum pyramidale were instead better modulated by slow gamma in CA1 stratum radiatum and CA3 stratum pyramidale (Figures 4.10 and 4.11). Furthermore, the 70-100 Hz frequency preferences disappeared during REM sleep (Figures 4.9, 4.10, and 4.11), when the CA3 network becomes less excited and drives fewer CA1 interneuron spikes (Figures 4.3, 4.11, and 4.19). Spike cross-correlations within the CA3 network do also show side peaks 12-13 ms from the central peak of synchronous spikes (Figure 4.14 and 4.15, Section 4.3.5), which precisely fits 80 Hz. So one alternative explanation may be that these units often oscillate at 80 Hz, but this 80 Hz is neither reflected in the CA3 pyramidal layer, nor in CA1 stratum radiatum, where the synaptic currents are widely dispersed and subject to cable filtering.

The paucity of recurrent excitatory synapses within CA1 means that LFPs there contain less information about local pyramidal cell activity than might be expected in CA3 or neocortical areas with greater recurrent connectivity. Consistent with this, putative principal cells in CA3 and EC3 preferred frequencies that overlap with the spectral bands that are theta-modulated (Figures 4.1 and 4.8). The CA1 interneuron network presented a different picture. We found a wider array of frequency preferences and tuning widths within the interneuron population, which as a whole seemed able to respond with greater fidelity to synaptic input patterns. Subpopulations were preferentially modulated by each frequency band (slow and medium gamma, as well as epsilon; Figure 4.9), and a unit's frequency preference often served as an indicator of its theta phase preference (Figure 4.14). Few units, however, preferred the theta phases

during which EC3 input was maximum, though many of the putative interneurons still fired during this phase and were significantly modulated by EC3 LFPs (Figures 4.2 and 4.11).

These results extended to multiunit activity. When the phase distribution for all CA1 pyramidal cell spikes during RUN states, pooled across units, sessions, and animals, was analyzed for non-uniformity, the most significant deviation for CA1 LFPs was at ~150 Hz. Substantial slow gamma modulation was present, with a dip from 45-55 Hz, and a small peak near 70 Hz. Compared to CA3 LFP phases, modulation was much weaker at all frequencies, and dropped below significance at 60 Hz. In comparison to EC3 LFPs, the best modulation was for 35 Hz, with a smaller peak around 55 Hz. Modulation strength dropped rapidly beyond that, falling below the significance threshold (for ~6 million spikes) above 95 Hz.

The above measurements of phase modulation disregarded the power in the wavelet transform at the spike times. We also ran calculations that incorporated power into the modulation index (the power serving as a weight for each phase angle), in addition to calculations on surrogate data sets to assess significance. The results were qualitatively the same.

4.3.5 Detectability of gamma oscillations in spike trains

The most consistent characteristic of LFPs is that they are confusing. The application of complicated transformations in an attempt to extract information from them can introduce distortions that are easily misinterpreted. Spike train analysis, on the

other hand, while having its own set of caveats, at least deals with discrete events that have a simpler and more concrete biophysical correlate. Finding spectrotemporal structure in spike trains similar to that presented above with spikes and LFPs would put these phenomena on firmer footing and facilitate their interpretation. Electrophysiological analysis of high frequency dynamics, interactions, and synchrony can be hampered by the technical difficulty of detecting and properly clustering overlapped spikes (Lewicki 1998). Despite this limitation, we sought to detect short timescale interactions and oscillatory behavior in the single unit spikes in our data set using spike train cross-correlograms (CCGs). The spike train CCGs, combined with a large number of suitably jittered surrogates for detecting significant deviations from chance (Perkel et al. 1967, Stark & Abeles 2009, Amarasingham et al. 2012), can reveal direct interactions or temporal coordination of the detected units (or whichever temporal variables are compared). The CCG for a pair of single units (i.e., putative spiking neurons) is calculated by binning their spike trains and convolving the resulting vectors up to a maximum time lag. Applying the same procedure for one unit to itself gives the autocorrelogram (ACG), which measures bursting and oscillatory behavior of the unit.

Analysis of ACGs has been proposed as an alternative for characterizing network oscillations, if suitable tricks are employed to account for the broadband spectral artifacts introduced by the central (zero time lag) peak in the ACG (proportional to the unit's firing rate, and typically set to zero when visualizing the ACG) (Mureşan et al. 2008). For low-frequency oscillations, the central peak/zero can be adequately removed to assess oscillatory dynamics using the spectral properties of the residual ACG (Mureşan et al.

2008). At high-frequencies, however, the proposed methods for the removal and smoothing of the massive and abrupt fluctuation introduced by the central peak/trough become unreliable and/or subjective. In addition, individual neurons have a limited ability to follow a high frequency oscillation with their spikes, with fast, repetitive spiking being governed by the burst dynamics of the membrane (Izhikevich 2000).

To assess whether spiking across the population was modulated rhythmically, and to detect short timescale interactions between neuron populations, we constructed multiunit CCGs (mCCGs) from single unit CCGs. The mCCG avoids several problems: (1) the zero-lag artifacts associated with ACGs; (2) zero-lag artifacts that result from the inability to detect simultaneous spikes at a single site; and (3) the symmetry inherent in ACGs, which adds artificial periodicity. The mCCG for two different populations of neurons (e.g., different cell types and/or anatomical regions) has a well defined directionality in time. The mCCG for a particular class of cells with itself does not, but the mCCG we use is still not symmetric, as we did not double-count unit pairs. This avoids the artificially enhanced rhythmicity in a two-sided ACG, which makes spike doublets appear on both sides of the central peak.

We calculated mCCGs for all well isolated pyramidal cells and interneurons in CA1, CA3, and EC3. Statistical analysis with randomly jittered surrogate spike trains have yet to be performed, so quantifications of significance are presently unavailable, but the qualitative results are quite informative. In addition to clear theta rhythmicity, the most striking features are the sharp peaks at zero time lag (±0.4 ms) for both pyramidal cells and interneurons in each region, but especially in the hippocampus (Figures 4.14

and 4.15). Synchronous firing between neurons of the same class (not counting SWRs), including pairs shown to not be connected by gap junctions, has been reported before (Csicsvari et al. 1999a, Csicsvari et al. 2003, Hu et al. 2011), but the mechanisms and function of these events are not yet understood. In each region, pyramidal cells showed strong excitatory coupling to interneurons in their own region, with pyramidal spikes followed by a sharp increase in interneuron spiking within a few milliseconds (Csicsvari et al. 1998). CA1 and EC3 interneurons, in turn, inhibited CA1 and EC3 pyramidal cells, respectively (Pouille & Scanziani 2001). Such inhibition was less apparent in the CA3 pyramidal-interneuron mCCG (Figure 4.16), probably because strong recurrent excitation within CA3 results in more synchronous firing of both cell types there. CA1 interneurons also showed a prominent increase in firing roughly 5 ms before pyramidal cells spikes. It is possible that this inhibition serves as a mechanism to induced synchronous pyramidal cell firing, by way of postinhibitory rebound spiking (Kandel & Spencer 1961, Buhl et al. 1995). EC3 pyramidal-interneuron mCCGs did not display such a strong peak, and such firing is present in CA3, it was masked by the more synchronous firing just mentioned.

The phase locking analysis of Section 4.3.4 implied that CA1 pyramidal cells time their spikes in relation to LFP features around 140-160 Hz. Such temporal coordination is evident during SWRs (Buzsáki et al. 1992, Csicsvari et al. 1999a), but it is unclear whether similar mechanisms operate during theta oscillations (Csicsvari et al. 1999a, Ray & Maunsell 2011a, Buzsáki & Silva 2012, Buzsáki & Wang 2012). A crucial test of whether such high-frequency power and/or phase locking reflects true coordinated and/or rhythmic firing is the detection of similar phasic firing in the spikes of the population.

The CA1 pyramidal mCCGs did, in fact, show such coordination during RUN and REM, with side peaks at 5-7 ms. This high frequency rhythmicity was far weaker than during SWRs, but, importantly, it survived when we excluded spikes within bursts (ISIs < 10 ms; lighter lines, Figure 4.14). Furthermore, these 6 ms side peaks were unique to CA1 pyramidal cells, with side troughs and side peaks of other cell types having different sizes and delays. During RUN (and more strongly during SWS), but not REM, CA3 pyramidal cells had side peaks corresponding to ~80 Hz. During REM, but less clearly during RUN, EC3 pyramidal cells and interneurons showed ~130 Hz rhythmicity.

Interregional mCCGs largely reflected the average theta phase distributions of firing, as well as known monosynaptic pathways or correlations due to strong common input, but we will point out several notable features. First is the weakness or absence of monosynaptic excitation onto CA1 pyramidal cells from CA3 and EC3 (Sayer et al. 1989, Levy et al. 1995, Csicsvari et al. 2003, Golding et al. 2005, Jarsky et al. 2005, Fernández-Ruiz et al. 2012, Zemankovics et al. 2013). As can be seen from the theta phase relationships (Figure 4.2), CA1 pyramidal activity did increase following CA3 pyramidal activity, on average. The mCCG shows a robust increase that was precise enough to imply a monosynaptic excitatory pathway between the populations (Figure 4.17). The EC3-CA1 mCCG, however, failed to show a clear excitatory effect of EC3 spikes on CA1 pyramidal spiking. Instead, CA1 pyramidal cell activity peaked before EC3 pyramidal cells (Figure 4.2), though a slight bump may be riding top of the overall decay in CA1 activity (Figure 4.18).

The weak response of CA1 pyramidal cells to CA3 input was likely due to a combination of the synapses themselves being weak (Sayer et al. 1989), as well as strong feedforward inhibition that compensated for it (Buzsàki 1984, Gulyás et al. 1993, Csicsvari et al. 1998, Pouille & Scanziani 2001, Atallah & Scanziani 2009, Zemankovics et al. 2013, Graupner & Reyes 2013). Indeed, the CA1 interneurons we detected were, as a whole, strongly excited at monosynaptic latencies by CA3 pyramidal cells (Figure 4.19). Monosynaptic excitation of CA1 interneurons by EC3 pyramidal cells, however, was not apparent in the mCCGs (Figure 4.17), though this may be due to a smaller number of interneurons with substantially greater firing rates limiting the sensitivity of our analysis.

Finally, CA1 pyramidal cells project many of their axons to the deep layers of EC (Cenquizca & Swanson 2007), and hippocampal SWRs have been shown to propagate to downstream neocortical structures (Chrobak & Buzsáki 1996, Siapas & Wilson 1998, Wierzynski et al. 2009, Peyrache et al. 2009, Mizuseki et al. 2009). Our mCCGs confirmed the direct excitation of EC5 units, especially interneurons, by CA1 pyramidal cells, as well as the entrainment of the EC5 population by SWRs (Figures 4.18 and 4.19). Additionally, despite a lack of innervation of layer 3 in medial EC by CA1 pyramidal cell axons (Cenquizca & Swanson 2007), CA1 SWRs did entrain EC3 interneurons (Figure 4.19). This led to a small dip, with a slight rhythmicity, in what was otherwise a broad increase in EC3 pyramidal cell firing during SWRs (the increase likely being related to the DOWN-UP state transitions that correlate with SWR events; Siapas & Wilson 1998, Battaglia et al. 2004, Sullivan et al. 2011). No short timescale interactions appeared for

EC2 units beyond the broad peri-ripple increase in firing. During RUN and REM, a small wave of extra firing in EC3 interneurons and a possible inhibition response in pyramidal cells can be seen (Figures 4.18 and 4.19).

4.4 Discussion

In our analysis of the temporal organization of network activity in the hippocampal circuit, we report the following principal findings. (1) During theta oscillations, LFPs recorded within the CA1 pyramidal layer had spectral structure in which various portions of the broad 'gamma' band are organized within the theta cycle in a state-dependent manner (Montgomery & Buzsàki 2007, Montgomery et al. 2008, Tort et al. 2008, Montgomery et al. 2009, Colgin et al. 2009, Tort et al. 2009, Belluscio et al. 2012). (2) Up to around 100-140Hz, LFP fluctuations in CA1 could be generated by synaptic input from afferent regions (Ray & Maunsell 2011a, Schomburg et al. 2012). (3) The CA1 interneuron population was more broadly and heterogeneously entrained by local and afferent LFP fluctuations (Buzsàki 1984, Atallah & Scanziani 2009). (4) CA1 pyramidal cells, in general, were poor followers of fast features and rhythms (>30 Hz) of excitatory input, especially those above 80 Hz. (5) Even on slower timescales, our analysis of both spiking activity and the activation of synaptic current generators in the LFP suggests that the CA1 network is a slow integrator of its input, with maximal spiking occurring late in the theta cycle compared to the input from EC that presumably starts the cycle (Mizuseki et al. 2009). The implications of these results run along two lines: (1) uncovering the physiological correlates of LFP signals, and (2) understanding the

operation and function of the hippocampal circuit. With the techniques available to date, we need to address the first problem in order to solve the latter one (though the necessity of doing so is starting to be alleviated with the increasing ability to record from larger numbers of single cells electrically, as well as optically).

4.4.1 The relationship of gamma band signals to spiking

Taken individually, the five main results outlined above have each been commented on before. Taken together, they suggest a picture in which gamma oscillations in CA1 may serve a different purpose than in many other neural networks. Why does CA1 exhibit such poor locking to gamma frequencies and such strong locking to ripple frequencies? Is this a robust property of CA1 network activity, or a consequence of our recordings and analyses?

In vivo studies of hippocampal gamma oscillations have consistently reported low proportions of CA1 pyramidal cells modulated at slow gamma frequencies. Some examples are collected in Table 4.1. Similar proportions of phase-modulated units were found using our methods (Table 4.2) [except for substantially greater slow gamma coupling between EC3 and CA1 compared to that reported by Colgin et al. (2009)]. Controversy exists, however, over how much of the significantly greater phase-locking of pyramidal cells in CA1 to “fast gamma” signals is simply a consequence of spectral leakage from broadband power of spikes into the gamma band (Manning et al. 2009, Zanos et al. 2011, Ray & Maunsell 2011a, Belluscio et al. 2012, Scheffer-Teixeira et al. 2013). Our spike-field coherence measurements, however, used LFPs recorded 400 μm

from the spike detection site, and the phase locking was band-limited. We also know, that CA1 possesses the capability to strongly oscillate at the very frequencies to which we find the strongest phase locking, in the form of SWRs. Does this 150 Hz locking reflect oscillations at that frequency during theta states?

Our unit-unit cross-correlation results argue that tight synchrony and true ripple-frequency coordination of spikes, beyond simple pyramid-interneuron spike pairs, do occur. In addition, the dominance of 140-160 Hz locking was unique to CA1. A possibility that we have not excluded is that miniature SWR-like events do occur in CA3-CA1 during momentary release from theta mechanisms. It could be that some combination of all these possibilities (indirect spike contamination from synchronized action potentials, correlated IPSCs from pyramidal-interneuron connections, coordinated burst firing, fast network oscillations, and aberrant SWRs) could all be contributing to this result. In any case, the SWR appears to be a truly special phenomenon in the brain, and it is seems likely that the CA1 network and physiology is precisely configured in order to generate it. The 150 Hz locking may simply be a reflection of those features, the details of which are still unclear, that endow CA1 with this ability.

4.4.2 Gamma LFPs and oscillations in CA1

In vitro models of gamma oscillations use cholinergic or metabotropic glutamate agonists to induce network oscillations in hippocampal slices (Whittington et al. 1995, Fisahn et al. 1998). These oscillations are typically 30-50 Hz, emerge from CA3, and require perisomatic inhibition (Hájos & Paulsen 2009, Whittington et al. 2010). A larger

portion of CA1 pyramidal cells are entrained by the gamma emanating from CA3 in these models (Zemankovics et al. 2013). The primary reason for this is likely the fact that there are substantially fewer interfering mechanisms at play. But the relatively low frequency of these rhythms is also probably a major factor. A key finding from in vitro studies relevant to the results presented here is the importance of recruiting perisomatic-targeting interneurons for entraining CA1 pyramidal cells. Importantly, Zemankovics et al. (2013) showed that without $GABA_A$-receptors in CA1, the strong gamma arriving from CA3 failed to generate substantial gamma power in stratum pyramidale, pyramidal cell modulation was significantly reduced, and, most importantly, pyramidal cells switched their preferred phase. When inhibition was operational, the CA3 input caused CA1 interneurons to suppress pyramidal cell firing during the excitatory phase, which instead fired just before then, i.e., at the phases when they were least inhibited. Complicating these findings, Pietersen et al. (2013) showed that CA1 mini slices can, in fact, generate its own slow-medium gamma (at around ~50 Hz), but that the stronger gamma emanating from CA3 suppresses these local gamma-generation machanisms.

The weak stratum pyramidale LFP oscillation in the presence of gabazine and the weak modulation of spiking imply that the somatic membrane potential does not oscillate coherently with the CA3 input without concurrent perisomatic inhibition. This hypothesis is supported by other in vitro experiments that measured somatic membrane potential in response to gamma frequency input to the dendrites. These studies, using both synaptic stimulation and current injection, showed that the cable filtering dramatically attenuates gamma frequency input, converting transient gamma input into a slower, theta-timescale

wave (Remondes & Schuman 2002, Golding et al. 2005, Vaidya & Johnston 2013). Additionally, the dendritic input typically either fails to elicit pyramidal cell action potentials (Sayer et al. 1989, Levy et al. 1995), perhaps due partially to feedforward inhibition (Ang et al. 2005), or does so by way of a slow dendritic spike, which may require properly timed input from both EC3 and CA3 (Jarsky et al. 2005, Takahashi et al. 2009).

Dendrite-targeting interneurons may have a similarly imprecise effect on timing spikes, serving more to shunt current, regulate excitation, synaptic plasticity, etc., rather than to synchronize (Koch et al. 1983, Miles et al. 1996, Buzsáki et al. 1996, Lovett-Barron et al. 2012, Royer et al. 2012, Gidon & Segev 2012, Leão et al. 2012, Basu et al. 2013). LFPs in dendrites are generated by synaptic currents, and so reflect modulation of the membrane potential. The cable properties of the dendrites, however, will affect the transformation between the current generating the LFP and the membrane voltage from the synapse site to the electrotonically distant soma. Fast impulses of current lead to slower membrane voltage responses, and these effects are amplified with distance from the site of the current pulse.

So some combination of filtered currents, rhythmically entrained perisomatic IPSCs, and volume conduction generate the measured gamma-frequency LFPs in stratum pyramidale. Moreover, in CA1 this happens for gamma-oscillating input from two separate sources. It may be no wonder then, that the somatic membranes and the spiking output of pyramidal cells do not precisely follow the interfering signals that are contained in the CA1 stratum pyramidale LFP. Methods for LFP decomposition, such as ICA and

CSD, may help in assessing the oscillatory state of the local network, but these techniques are nontrivial and introduce their own set of difficulties.

The key to synchronizing with CA1, then, if this was the purpose of oscillatory input, would appear to be the perisomatic-targeting interneurons (Destexhe 2010). In CA1, basket cells and axo-axonic (chandelier) cells are contacted by EC3 synapses (Kiss et al. 1996). Our spike correlations, however, showed no appreciable effect of EC3 spikes in CA1 interneurons, though pooling spikes across units, lower number of axo-axonic cells, and the proximity of most of our probes to the pyramidale layer all limit our ability to detect these interactions. Still, the absence of any strong signatures of EC3 input coordinating gamma-band activity in CA1 suggests that it serves other roles. Perhaps the fast oscillations in EC serve the purpose of synchronizing its own output in a patterned way on the dendrites of its targets (Takahashi et al. 2012, Makara & Magee 2013, Menon et al. 2013). The modulation of general dendritic excitation, nonlinear dendritic events, and synaptic plasticity, in combination with input from CA3 (Remondes & Schuman 2002, Jarsky et al. 2005, Takahashi & Magee 2009, Müller et al. 2012, Basu et al. 2013, Vaidya & Johnston 2013), seem to be more promising ways for the entorhinal cortex to shape hippocampal connections and influence its output.

Table 4.1 Previously reported values for hippocampal gamma phase-locking in vivo.

Study	freq. (Hz)	% units signif.	signifi. thresh.	other notes
Csicsvari et al. 2003	30-80	CA1p: 43% (local) 13% (distal) CA1i: >80% (local & distal)	$p < 0.05$	
Tukker et al. 2007	30-80	CA1p: 47%	$p < 0.05$	LFP recorded on different shank
Senior et al. 2008	30-80	CA1p: 32% (RUN) 4% (REM)	$p < 0.01$	
Colgin et al. 2009	25-50	CA1p: 25% CA3p: 53% EC3p: 0%	$p < 0.05$	phase-locking to CA1 LFP recorded on different electrode
	65-140	CA1p: 36% CA3p: 32% EC3p: 44%	$p < 0.05$	phase-locking to CA1 LFP recorded on different electrode
Mizuseki et al. 2011	30-80	CA1p: 27% (RUN) 10% (REM)	$p < 0.01$	(data set overlaps with the one analyzed for our analysis)
Belluscio et al. 2012	30-50	CA1p: 18% CA1i: 89%	NR	(data set overlaps with the one analyzed for our analysis)
	30-90	CA1p: 22% CA1i: 90%	NR	(data set overlaps with the one analyzed for our analysis)
	90-150	CA1p: 75% CA1i: 94%	NR	(data set overlaps with the one analyzed for our analysis)

Table 4.2 Our results for hippocampal gamma phase-locking in vivo.

Comparison	freq.(Hz)	% units signif.	Notes
CA1p - CA1 LFP	30-50	RUN: 31%, REM: 8%	% with at least one significantly ($p < 0.01$) modulated frequency in specified band. LFP site 400 μm from unit detection site.
	60-90	RUN: 22%, REM: 11%	
	100-200	RUN: 51%, REM: 42%	
CA3p - CA1 LFP	30-50	RUN: 17%, REM: 3%	
	60-90	RUN: 32%, REM: 1%	
	100-200	RUN: 28%, REM: 5%	
EC3p - CA1 LFP	30-50	RUN: 23%, REM: 22%	
	60-90	RUN: 26%, REM: 22%	
	100-200	RUN: 24%, REM: 25%	

4.5 Figures for Chapter 4

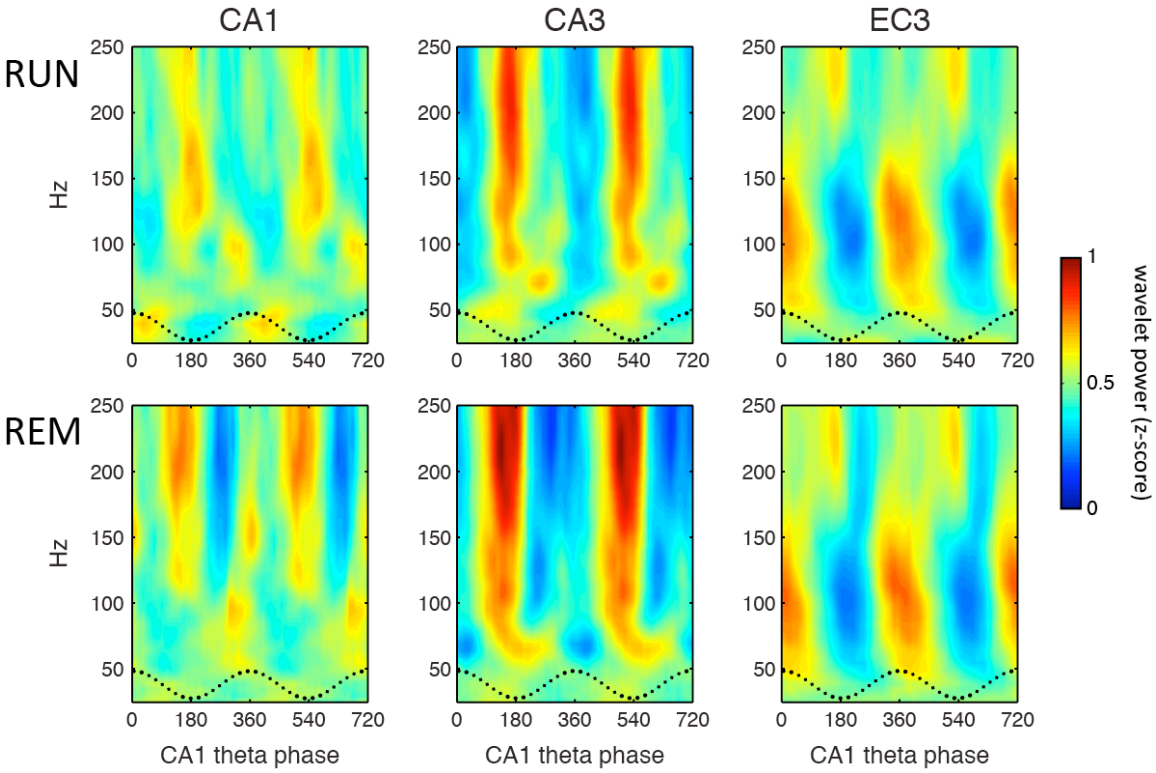

Figure 4.1. Theta oscillations modulated power in the gamma band and above in a state-dependent manner for CA1. Both CA3 and EC3 maintained similar theta-gamma profiles during RUN and REM, but the differential change in activity level of the two regions (Figure 4.3) resulted in a reorganization of CA1 activity within the theta cycle (Figure 4.2). Hot and cold colors indicate mean wavelet power at each frequency for times in each theta phase bin. Theta phase was measured from the angular mean of the CA1 stratum pyramidale sites available that session.

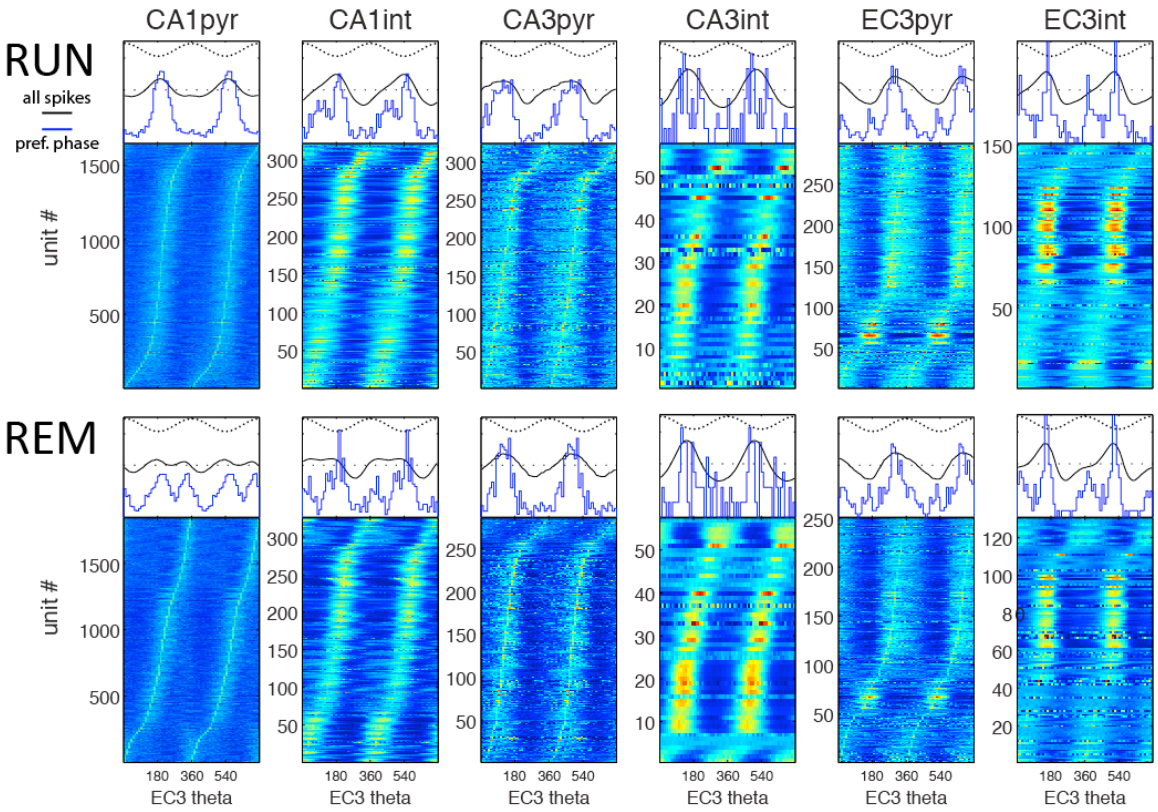

Figure 4.2. Firing rate modulation for each significantly modulated unit ($p < 0.01$, Rayleigh test) in CA1, CA3, and EC3 is shown as a color-coded line in the heat plots (ordered by preferred phase). Black lines above color plots show histogram of theta phases for all spikes, blue lines show the distribution of preferred phases for all significantly modulated units (scaled by 0.5 for visualization). EC3 theta (which is in phase with CA1 stratum pyramidale theta; Mizuseki et al., 2009) was more often available as a reference, was less sensitive to position than CA1 theta. (EC3 has larger amplitude theta, and CA1 theta phase is sensitive to the exact position of the electrode relative to the middle of the pyramidal layer; Lubenov and Siapas, 2009).

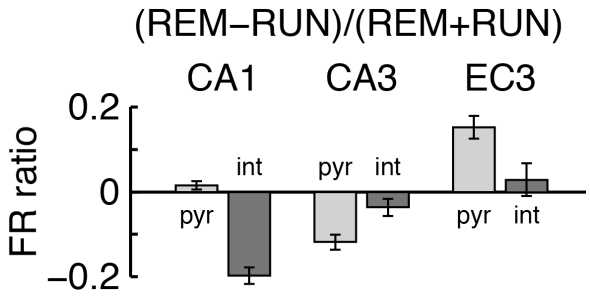

Figure 4.3. Mean +/- sem of firing rate changes for single units recorded during both RUN and REM.

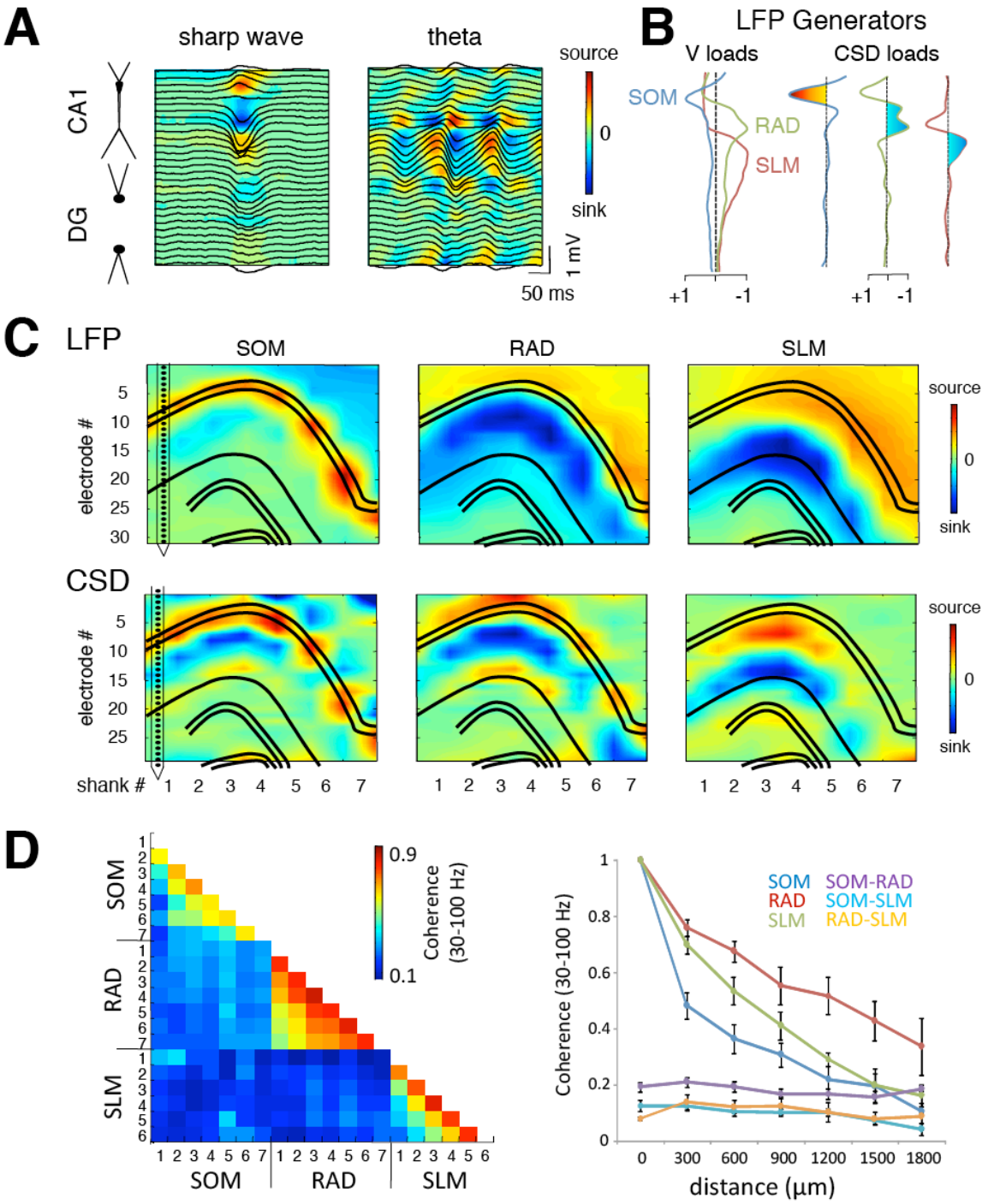

Figure 4.4. ICA-extracted generators correspond to anatomical synaptic pathways. ***A,*** SWR and theta LFP and CSD profiles along one shank the recording. The schematic on the left illustrates the approximate anatomical position of each electrode relative to the principal cells in CA1 and the dentate gyrus (DG). ***B,*** The voltage loadings and

corresponding CSDs for the three main CA1 synaptic generators extracted by ICA decomposition of one shank's LFPs during a concatenated segments of awake and sleep recordings. ***C,*** Maps of the LFP generators (and their CSDs) of the CA1 generators. Each generator was extracted by application of ICA to the individual shanks, and the two dimensional maps were constructed by linearly interpolating between electrodes. ***D,*** The coherence matrix (as measured by the the phase locking value of the 30-100 Hz bandpass-filtered activations) between pairs of generators from each shank. Note the high coherence between like generators on different shanks. This is in contrast to the low coherence from different generators on the same shank, though this low cross-generator coherence is, to large degree, enforced by the ICA algorithm. ***E,*** The coherence between like generators on different shanks decreased monotonically with separation distance.

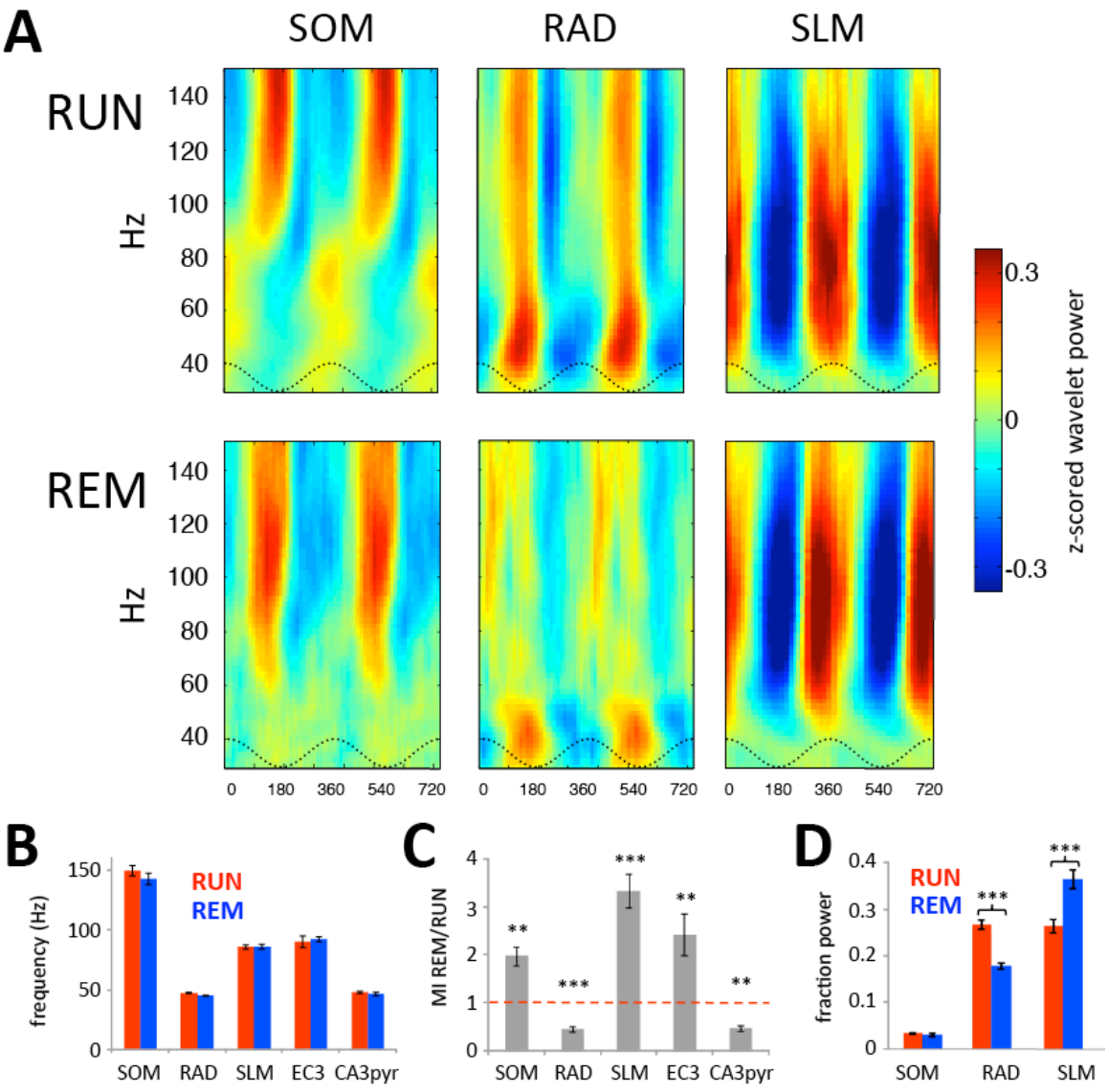

Figure 4.5. Theta-gamma properties of the ICA generators. ***A,*** The wavelet spectra of each component were theta-modulated during RUN and REM. Coloring indicates the z-score normalized changes in power at each frequency. ***B,*** Group data (across shanks and animals) indicating the maximally modulated frequencies (mean ± s.e.m.) of each generator and the LFP in the afferent regions (EC3 and CA3 stratum pyramidale). ***C,*** Changes (as measured by the ratio; mean ± s.e.m.) in the modulation indices (at the maximally modulated frequencies) between RUN and REM for the generators and LFPs

in *B*. ***D,*** The strength of each generator (mean ± s.e.m.) during RUN and REM epochs, as measured by the proportion of total signal variance explained by each. Asterisks denote significance: **, $p < 0.01$; ***, $p < 0.001$.

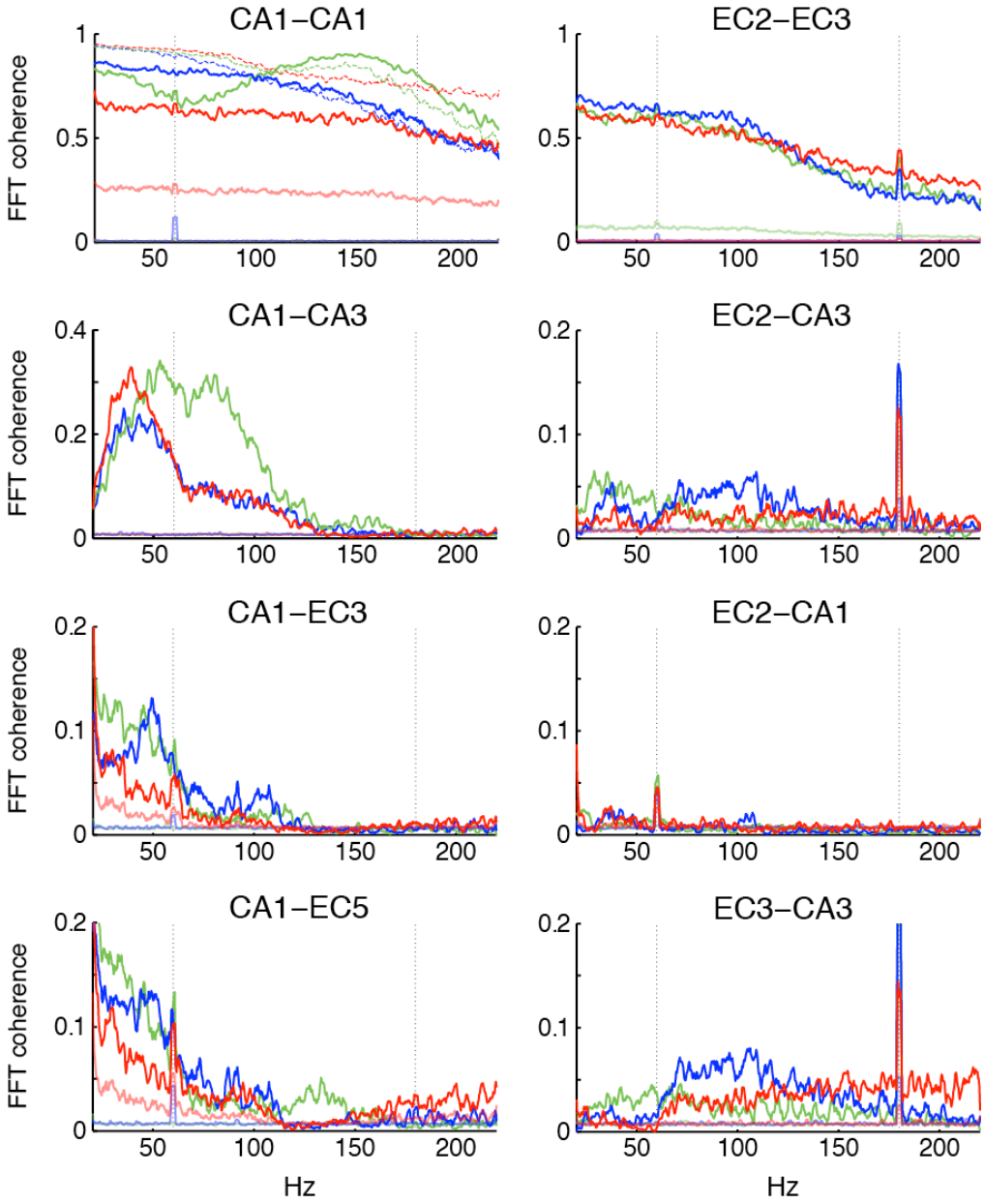

Figure 4.6. Coherence spectra between sites in two animals during RUN (red), REM (blue), and SWS (green), compared to the 99th percentile values (light traces) for 200

surrogate data sets with LFPs of different channels randomly shifted with respect to each other. CA1-CA1 coherence is given for each of the two animals (light and dark traces). Dotted vertical lines mark 60 and 180 Hz, the first and third harmonic of the power line frequency, which were present in a subset of channels in the recordings.

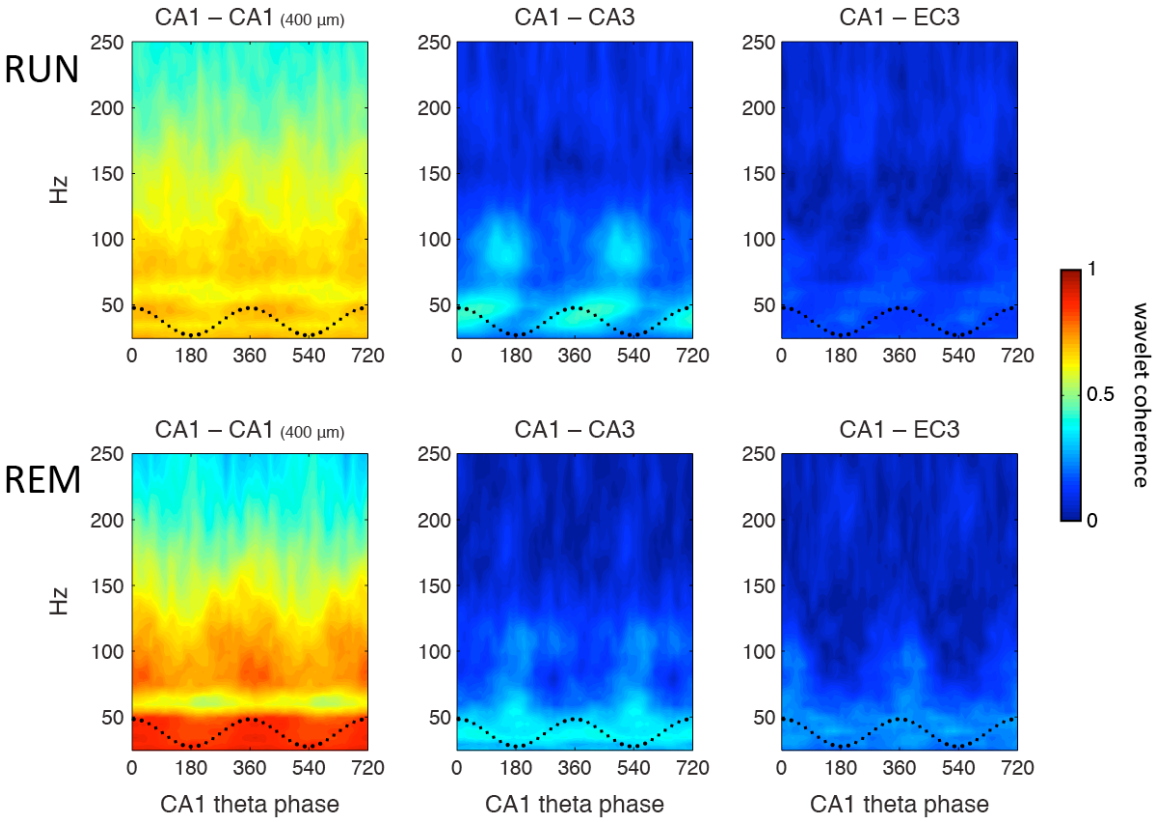

Figure 4.7. Wavelet coherence spectra between CA1 and its afferent regions for time points in each of 32 theta phase bins during RUN and REM. One of the CA1 channels in the CA1-EC recording had 60 Hz line noise, which made 60 Hz less (arrowhead) coherent than surrounding frequencies.

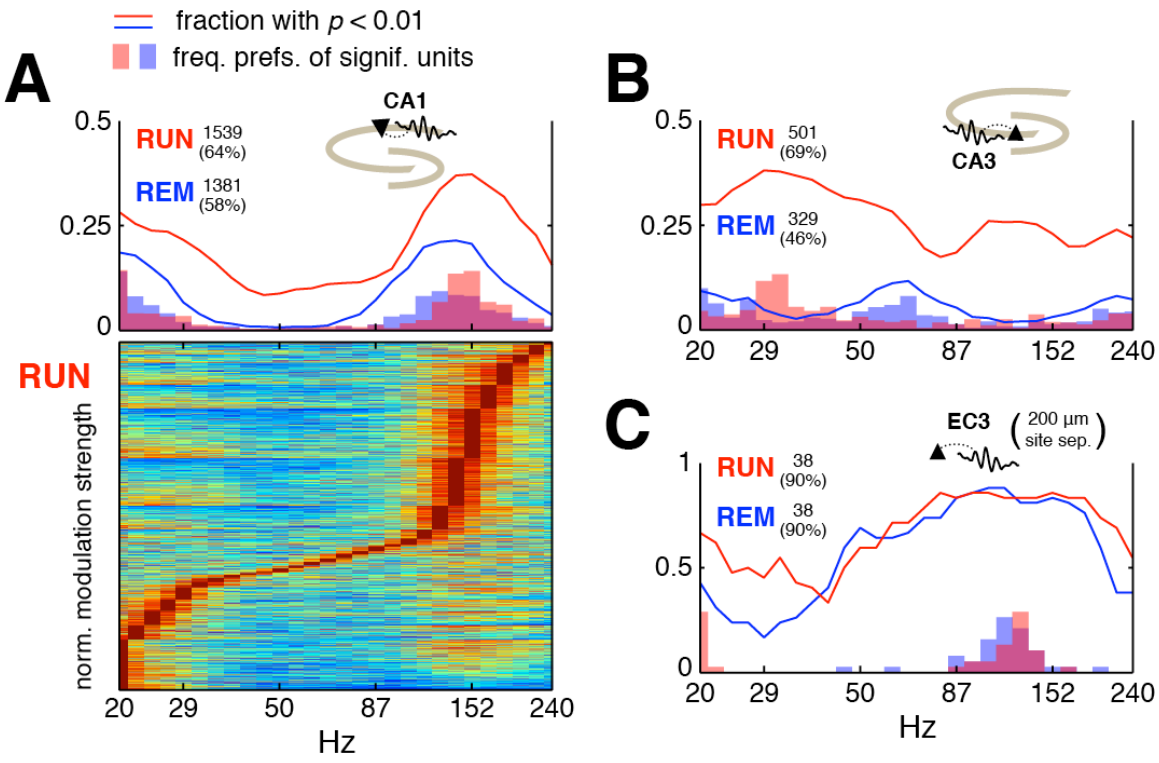

Figure 4.8. Unit-LFP phase locking for putative pyramidal cells in CA1, CA3, and EC3, compared to wavelet phases of the LFP on a different shank in the same region. Unit-LFP site separation was 400 µm for CA1 and CA3, 200 µm for EC3. ***A,*** Color plot (bottom) shows the normalized modulation strengths (to the maximum value) versus frequency for each CA1 unit that was significantly modulated ($p < 0.01$) by the CA1 stratum pyramidle LFP for at least one frequency. 1539 units shown, 64% of all pyramidal units. The line and bar plots (top) summarize the group results. Lines indicate the fraction of the population significantly modulated at each frequency (a single unit can be significantly modulated at multiple frequencies). Bars indicate the fraction of significantly modulated units that preferred each frequency (adding up to 100%). Numbers next to RUN and REM indicate the number of units that were significantly modulated by any frequency (from 20-240 Hz) during each state, and the percentage of

the total population this accounted for. ***B,*** Same as *A*, but for CA3 unit modulation by CA3 stratum pyramidale LFPs. ***C,*** Same as *A*, but for EC3 unit modulation by EC3 LFPs.

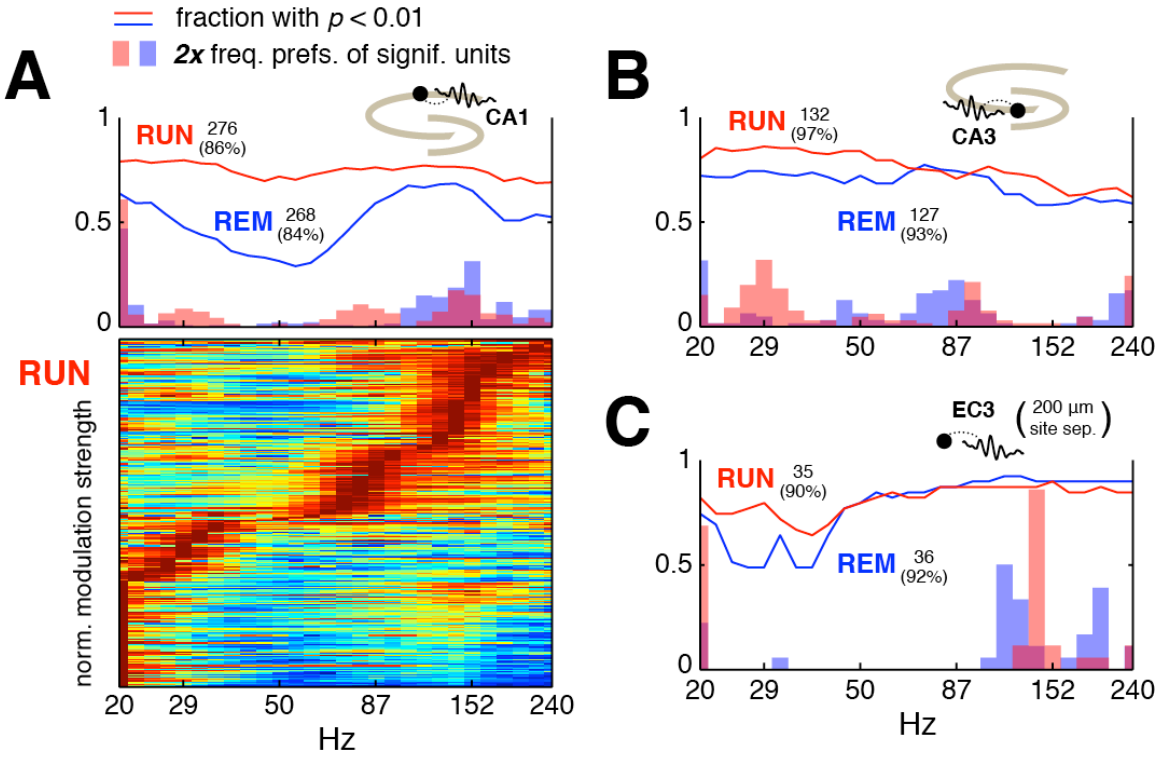

Figure 4.9. Same layout as Figure 4.8, but for putative interneurons.

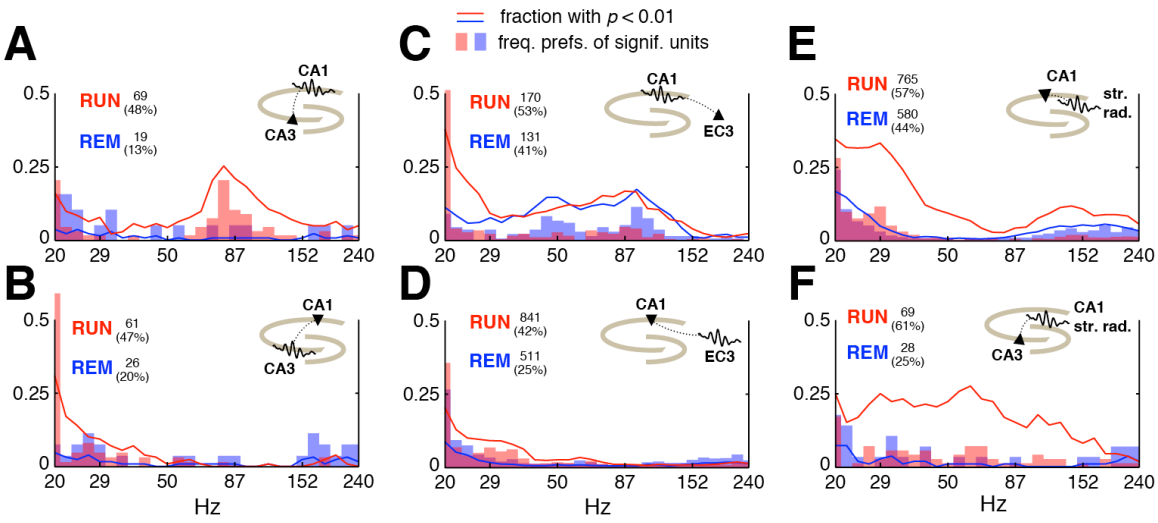

Figure 4.10. Unit-LFP phase locking for putative pyramidal cells in CA1, CA3, and EC3, compared to wavelet phases of LFPs in different regions/layers. Same layout as group data plots in Figure 4.8. ***A,*** CA3 pyramidal unit modulation by CA1 stratum pyramidale LFP phase. ***B,*** CA1 pyramidal unit modulation by CA3 stratum pyramidale LFP phase. ***C,*** EC3 pyramidal unit modulation by CA1 stratum pyramidale LFP phase. ***D,*** CA1 pyramidal unit modulation by EC3 LFP phase. ***E,*** CA1 pyramidal unit modulation by CA1 stratum radiatum LFP phase (~400 μm away). ***F,*** CA3 pyramidal unit modulation by CA1 stratum radiatum LFP phase.

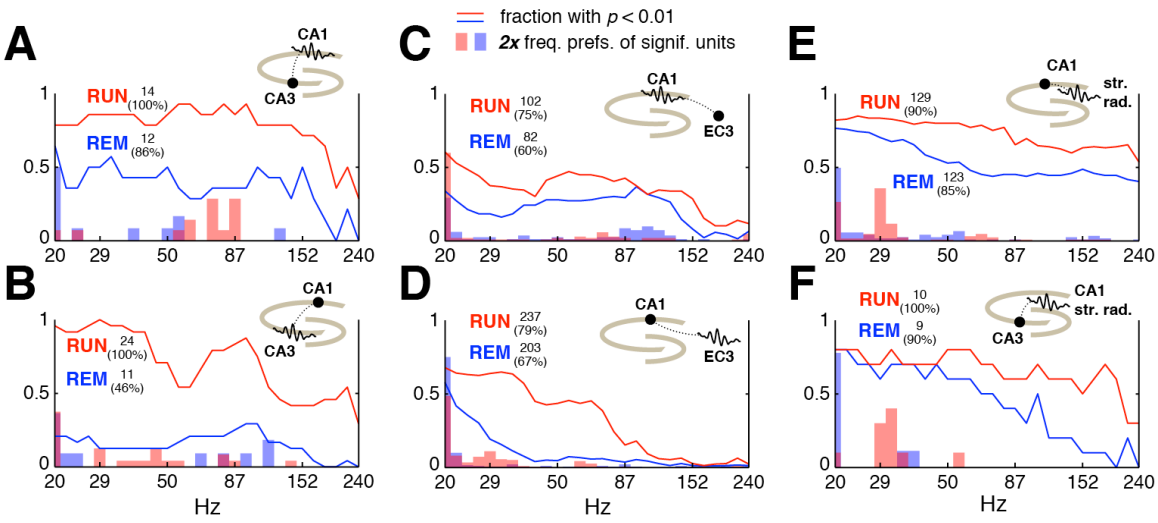

Figure 4.11. Same layout as Figure 4.10, but for putative interneurons.

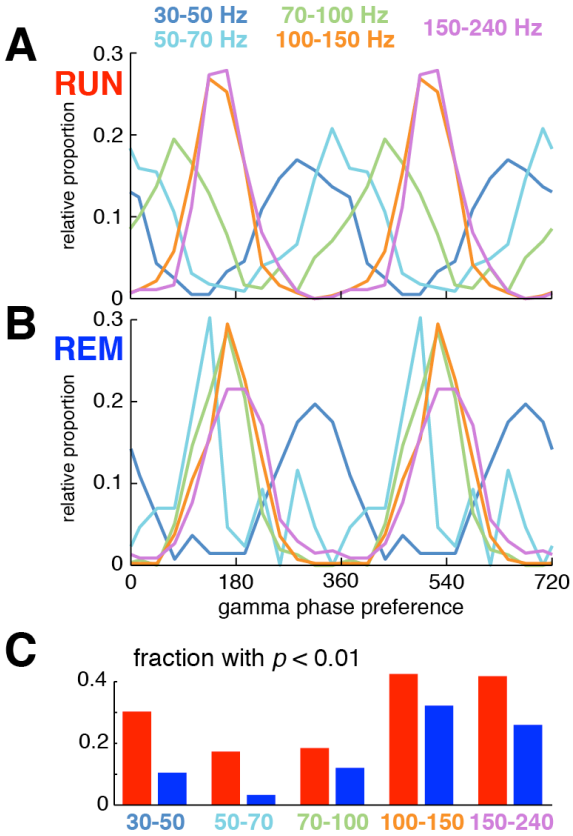

Figure 4.12. ***A, B,*** 'Gamma' phase preferences for pyramidal units that were maximally modulated (i.e., 'prefer') frequencies in the color-coded spectral bands. Note the change

in phase preferences between RUN (*A*) and REM (*B*) for 50-100 Hz frequencies, perhaps indicating the increased relative contribution of spike waveforms to the gamma LFP (Schomburg et al. 2012, Waldert et al. 2013) without strong gamma input from CA3. ***C,*** Fraction of pyramidal units during RUN (red) and REM (blue) that were significantly modulated in each frequency band.

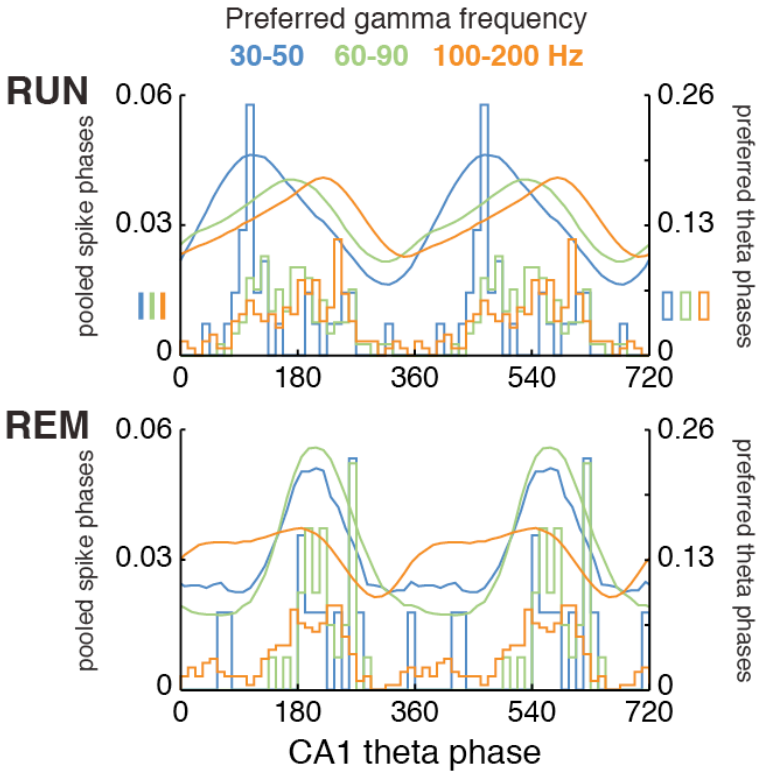

Figure 4.13. CA1 interneurons preferring different theta phases could be segregated by their gamma frequency preferences. Smooth lines show spike phase distributions for all spikes, pooled across units that preferred frequencies within each indicated band,. Stepped lines show the distribution of theta phase preferences for the units that preferred each band.

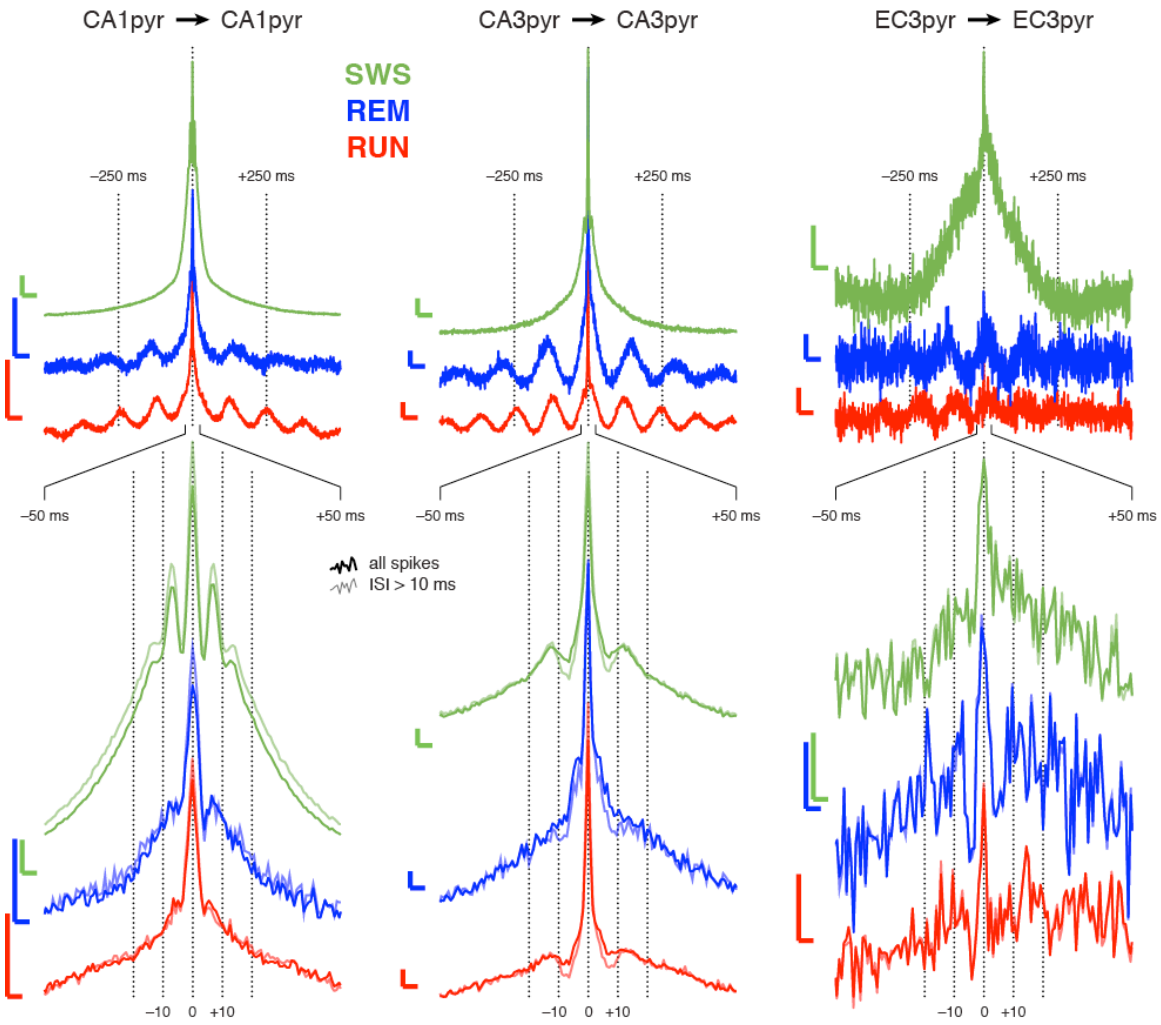

Figure 4.14. Some spike phase-locking features can be seen in mCCGs (i.e., pooled CCGs across particular cell pair categories; Section 4.2.5). During RUN, REM, and SWS, the mCCGs for pyramidal-pyramidal unit pairs within the same region (from different shanks) show strong theta and SWR characteristics. During both RUN and REM, CA1 pyramidal unit mCCGs showed side-peaks at 5-6 ms, whether or not burst spikes, liberally defined here as groups of 2 or more spikes with ISIs <10 ms, were included. (Note, however, that bursts could still be present through the misclassification of burst spikes during clustering; Harris et al. 2000.) CA3 pyramidal units showed side-

peaks during RUN at ~12 ms, and EC3 pyramidal units had some during REM at 8-10 ms.

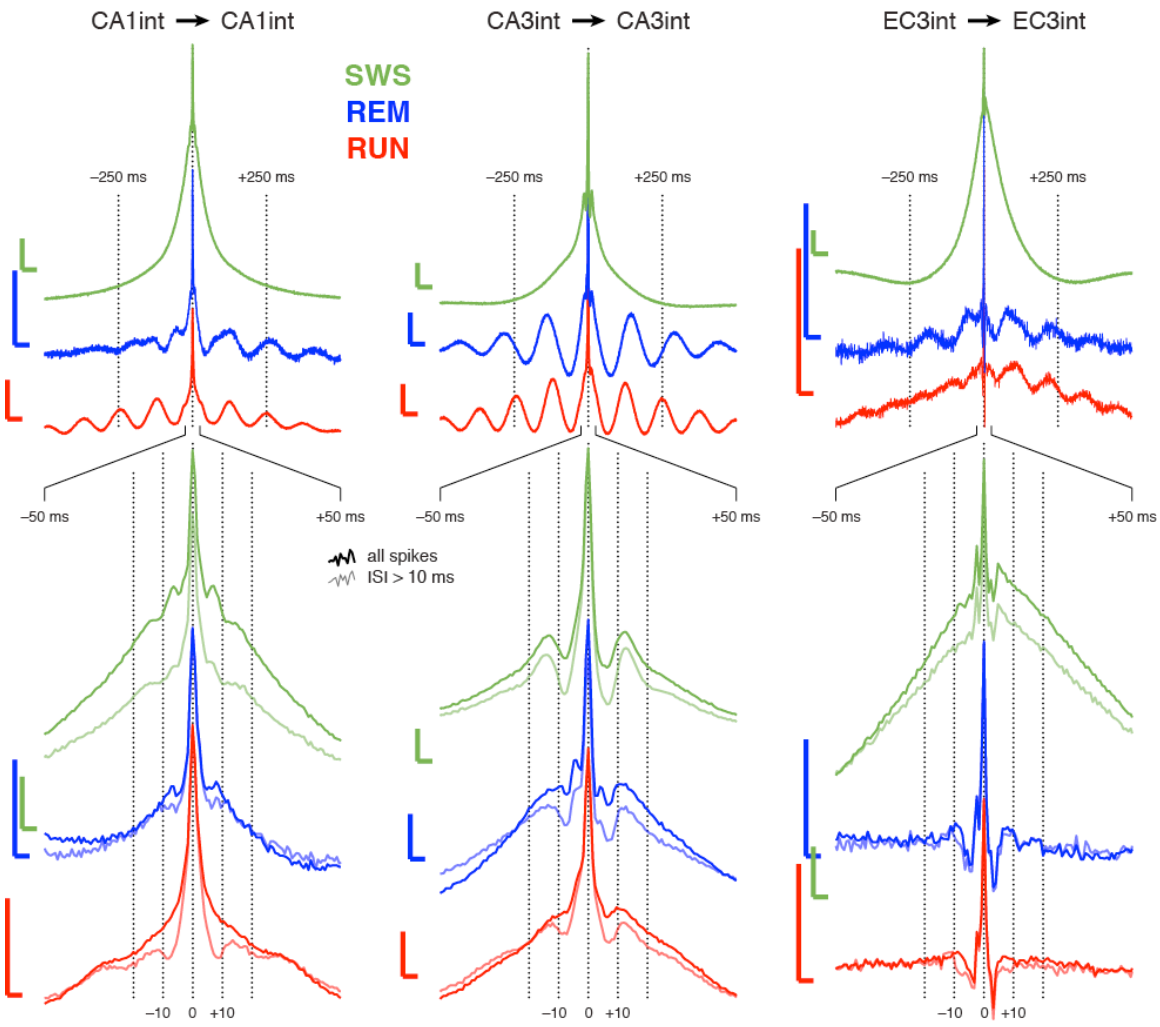

Figure 4.15. Same as in Figure 4.14, but for interneurons. Here the first side-peaks could potentially be consequences of the 10 ms ISI spike-exclusion rule. Despite this however, CA1 interneurons during RUN the 'burst' exclusion actually reveals second side-peaks. This hints at a possible reason for the poor gamma entrainment of CA1 pyramidal cells: even individual interneurons may fire 'doublets' (i.e., spike twice within a single gamma wave) (Traub et al. 1996; but see Penttonen et al. 1998), both affecting the measured LFP

phase and destabilizing the phase-locking of pyramidal cells. As in EC3 pyramidal cells, EC3 interneurons exhibit stronger fast gamma oscillations during REM than RUN.

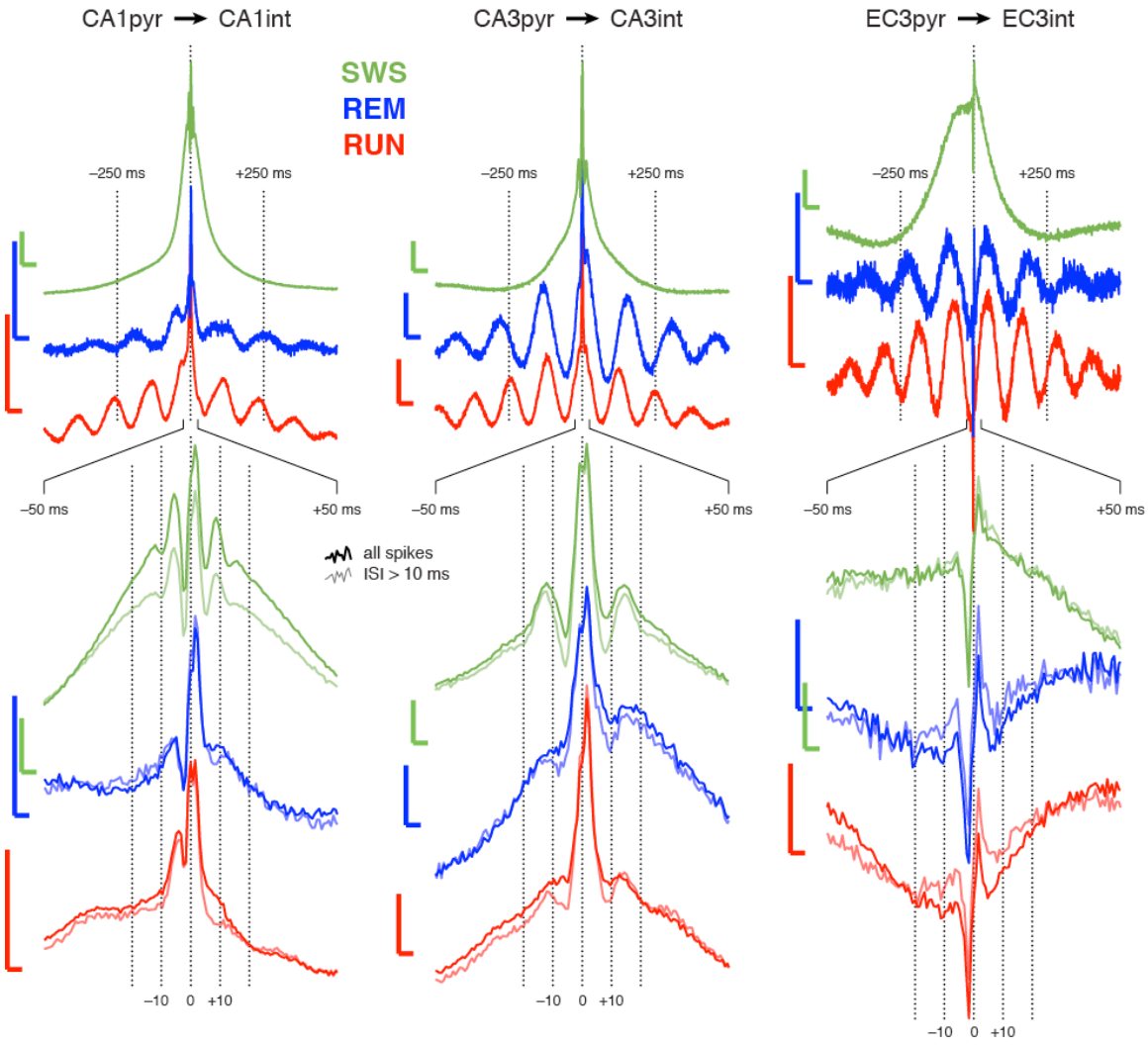

Figure 4.16. Same as in 4.14, but for pyramidal-interneuron unit pairs within the same region (but at different shanks). In CA1, increases in interneuron firing precede, coincide with, and follow pyramidal unit spikes. CA3 also shows strong synchronous firing, whereas EC3 pyramidal-interneuron pairs display a more classical inhibition-excitation profile (Moore et al. 1970).

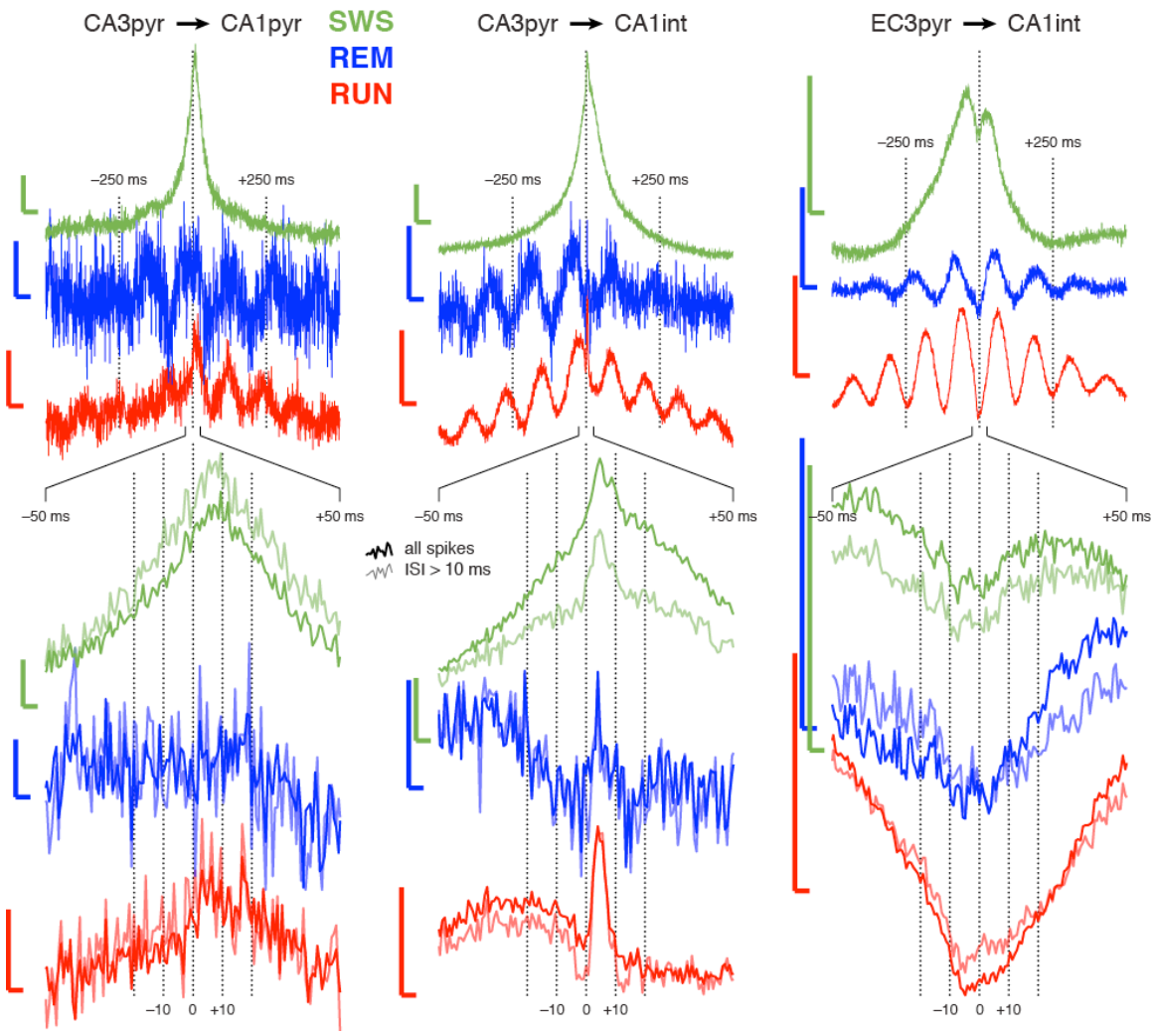

Figure 4.17. Same as in 4.14, but for CA3 pyramidal units to CA1 pyramidal and interneuron units, and for EC3 pyramidal units to CA1 interneurons. Monosynaptic excitation from CA3 is weak but visible for CA1 pyramidal units. It is much more distinct (especially during RUN) for CA1 interneurons. Monosynaptic excitation of CA1 interneurons by EC3 pyramidal units is not apparent in these mCCGs, though such connections are known to exist (Kiss et al. 1996, Gulyás et al. 1999), and evidence of feedforward inhibition from EC3 has been reported (Ang et al. 2005).

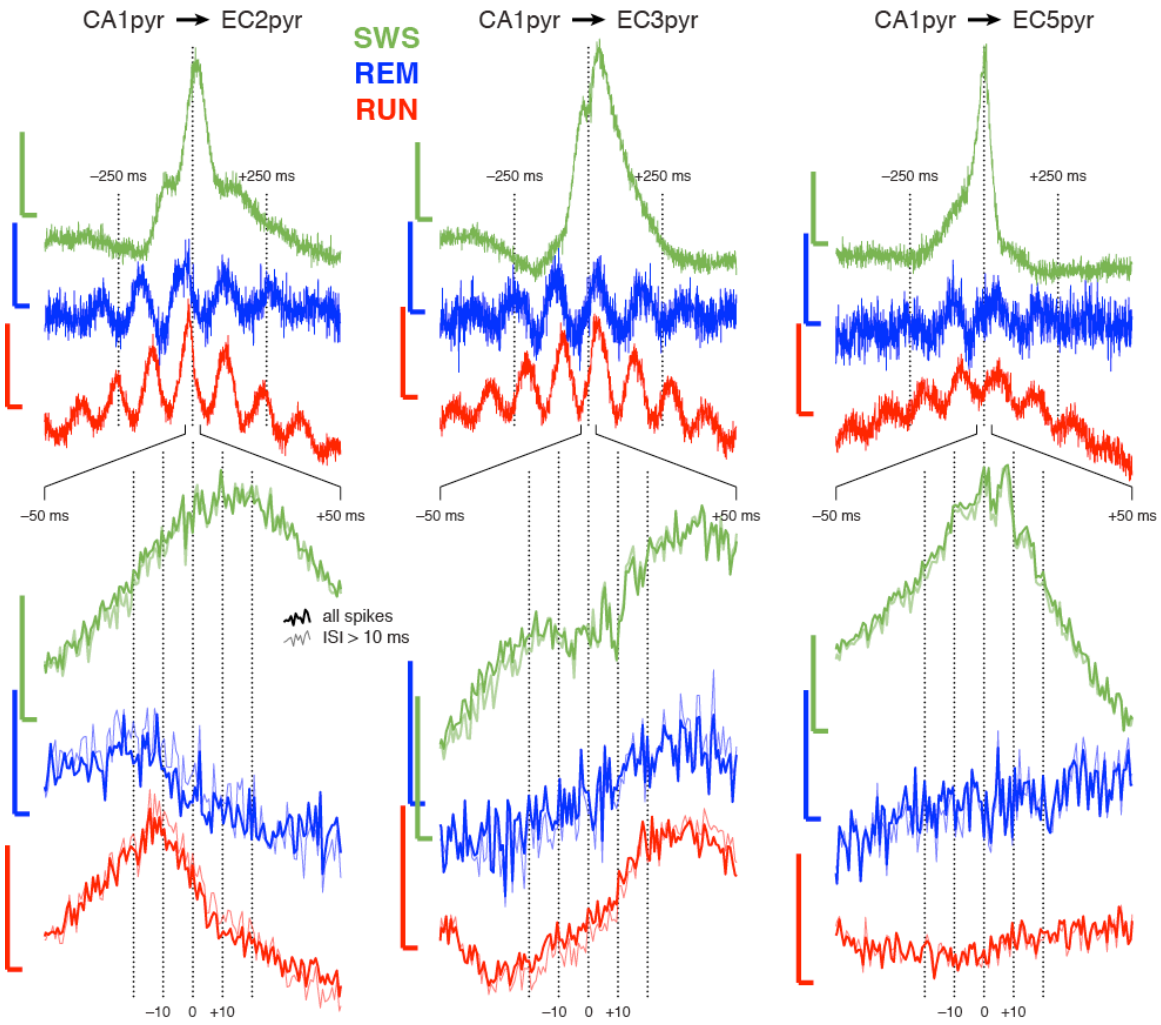

Figure 4.18. Same as in Figure 4.14, but for CA1 pyramidal to EC pyramidal units. Monosynaptic interactions between are not convincingly apparent, in either direction, except potentially for CA1-to-EC5, though the ripple-frequency EC5 pyramidal unit modulation during SWS may also be mediated by the strongly entrained EC5 interneurons (Figure 4.19). A mild dip (perhaps with some ripple-frequency rhythmicity) of EC3 pyramidal units from their otherwise elevated firing during ripples is also visible.

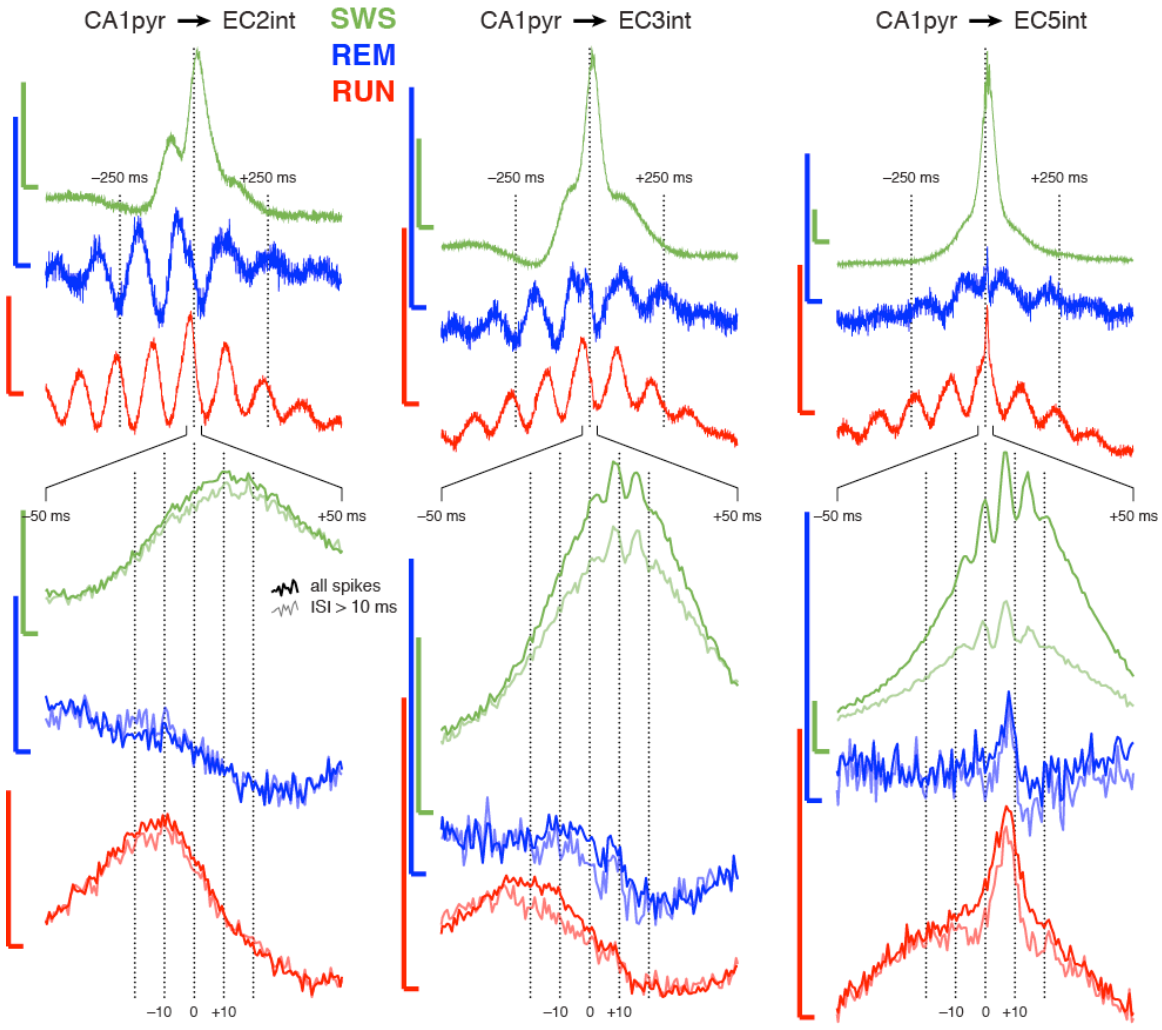

Figure 4.19. Same as in Figure 4.14, but for CA1 pyramidal units to EC interneurons. Monosynaptic excitation of EC5 interneurons is apparent, and EC3 interneurons are mildly entrained during ripples.

5. EMG leakage into intracranial recordings

5.1 Introduction

A number of recent studies have shown that high frequency LFP and ECoG signals can be informative about neural processing (Ray et al. 2008a, Jacobs & Kahana 2009, Gaona et al. 2011), though the mechanisms underlying these signals and what they reflect is still being debated (Chapter 4; Colgin et al. 2009, Miller 2010, Ray & Maunsell 2011a, Jackson et al. 2011, Belluscio et al. 2012, Buzsáki & Silva 2012, Schomburg et al. 2012, Scheffer-Teixeira et al. 2013). It has become clear that localized spikes can generate substantial power in the high gamma and epsilon bands (Zanos et al. 2011, Ray & Maunsell 2011a, Belluscio et al. 2012, Scheffer-Teixeira et al. 2013), yet true fast oscillations do exist (Buzsáki & Silva 2012), and specific functional roles for this band in network communication have been hypothesized based on the appearance of coherent signals in distant hippocampal-neocortical regions (Colgin et al. 2009, Colgin & Moser 2010, Scheffzük et al. 2011). We have seen in several of our own recordings, however, signs that many features that would normally be included in an analysis of high frequency LFPs is actually more characteristic of muscle contamination, i.e., electromyographic (EMG) signals.

Electrophysiologists are already well aware that movement-related activity can contaminate neural recordings (O'Donnell et al. 1974, Matsuo et al. 1975, Goncharova et al. 2003, Muthukumaraswamy 2013). Indeed, oculo-motor artifact identification or removal is common practice in electroencephalography measurements (Gao et al. 2010, Muthukumaraswamy 2013), and large amplitude, high frequency, broadband, and

spatially widespread signals regularly appear when an implanted rodent is chewing (Sasaki et al. 1983). Apart from these seemingly discrete events, however, the signal is assumed to reflect predominantly electrical activity in nearby brain structures. The problem arises when investigators include high frequency parts of the spectrum in their analysis. Extracellular recordings generally exhibit a 1/f decay in spectral density (Freeman et al. 2000), and myoelectric potentials are broadband, extending down to ~10 Hz (O'Donnell et al. 1974, Goncharova et al. 2003).

Here we characterize the putative EMG signal component in multisite recordings in rats, which is relatively low amplitude and tonic, and we present data linking it to muscle activity. We also suggest ways to mitigate this contamination so that true neural signals may be more reliably isolated. The identification and, ideally, the removal of such external signal components is important for the analysis and interpretation of neural data.

5.1 Methods

5.1.1 Surgery, behavioral testing, and recording

Recordings were performed in male Long-Evans rats (250-400 g) implanted with silicon-based multielectrode arrays during waking behavior and sleep. Behavioral tasks included running on a linear track and a hippocampus-dependent delayed spatial alternation task (Montgomery & Buzsàki 2007). Animals with three recording configurations were analyzed: (i) a 96-site probe with 8 shanks, separated by 200 μm, each with 16 contacts spaced at 100 μm, oriented in a transverse plane of the dorsal hippocampus in the right hemisphere (Montgomery & Buzsàki 2007); (ii) one 4-shank

silicon probe in the right dorsocaudal medial entorhinal cortex for recording up to three layers simultaneously, and a 4- or 8-shank probe (300 μm between shanks, 20 μm contact spacing) in the right dorsal hippocampus oriented along the septotemporal direction to record from within or near a single layer (CA1, CA3, or DG) at most sites (Mizuseki et al. 2009); (iii) bilateral implantation of two 8-shank probes (20×300 μm spacing) into the dorsal hippocampi along the septotemporal direction, with all sites in or near the CA1 pyramidal layer. In all animals, two stainless steel screws in the skull above the cerebellum served as the ground and voltage reference .

During the recording sessions, neurophysiological signals were amplified, bandpass-filtered (1 Hz - 5 kHz), and acquired continuously at 20 kHz. After recording, local field potential (LFP) was down-sampled to 1250 Hz for additional analysis.

5.1.2 Data analysis

Behavioral and sleep states were detected based on experimenter notes, video tracking, and LFP patterns. RUN epochs included locomotion during behavioral tasks, with periods of immobility (<5 cm/s) and consummatory behaviors excluded from the analysis. During sleep recordings, REM periods were detected using the ratio of power in the theta band (4-12 Hz) to power in the surrounding bands (1-4 Hz, 12-30 Hz) in the hippocampus (Csicsvari et al. 1999a, Montgomery et al. 2008), or a similar measure in layer 3 of the entorhinal cortex (EC3) (Mizuseki et al. 2009).

Theta power and phase were measured using the Hilbert transform of the theta band-filtered (5-10 Hz) LFP. Power and coherence spectra were calculated using

continuous wavelet transforms with complex Morlet wavelets and Hilbert transforms on narrow-band-filtered data (Le Van Quyen et al. 2001). Filters were designed for at least 60 dB stopband attenuation using the Matlab DSP Systems Toolbox.

Current source densities (CSD) were estimated using the second spatial derivative of the LFP on consecutive channels (Nicholson & Freeman 1975, Mitzdorf 1985). Bad channels (e.g., dead channels, excessive noise, crosstalk) and sites adjacent to bad channels were excluded from the analysis. Independent component analysis (ICA) was performed using the *runica()* function from the EEGLAB toolbox (Delorme & Makeig 2004), which is a Matlab implementation of the infomax ICA decomposition algorithm (Bell & Sejnowski 1995, Makeig et al. 1997).

5.2 Results

5.2.1 Detection and characterization of muscle-related signal components when EMG recordings are unavailable

Over long timescales, the power spectral density of in vivo LFP recordings decays inversely with frequency (Freeman et al. 2000). In many of the recordings we analyzed, however, the power spectrum plateaued above 100 Hz during locomotion (RUN), resulting substantially more power than during rapid eye movement (REM) sleep and slow-wave sleep (SWS). This difference in spectral power density could not be explained by differences in spiking activity, because average firing rates in CA1 were similar between REM and RUN, and higher during SWS compared to RUN (Figure 5.1B, D). Firing rates increased from RUN to REM for principal cells in layer 3 of the entorhinal

cortex (EC3) (Figure 5.1D), which projects to CA1 stratum lacunosum-moleculare (Andersen et al. 2007), in contrast to the substantially greater high-frequency power in both stratum lacunosum-moleculare and EC3 during RUN (Figure 5.1A).

The additional high-frequency power was not only present on all channels, but was, to a large degree, modulated synchronously across all of them. Figure 5.2 shows power correlations and phase synchrony between signal components at many different frequencies from pairs of recording sites through a transverse plane of the right dorsal hippocampus. Most of the pairs exhibit theta-frequency coupling, but spectral comodulation and coherence should be more localized at higher frequencies and dependent on either direct synaptic connections or spatial proximity (for volume conduction) (Lindén et al. 2011, Łęski et al. 2013). During RUN, however, all of the site pairs were strongly comodulated at frequencies greater than 100 Hz (Figure 5.2B). Even more striking, these high-frequency signal components were coherent and synchronous across channels. Figure 5.2C shows the correlation coefficients for each frequency of the product of power in a channel pair and the phase difference between the channels. Regions without direct connections or common input (or volume conduction) would be expected to have uncorrelated phases, and more strongly connected regions may be coherent, but will usually have a nonzero phase difference, depending on the connection directionality, signal delay, the physiology within each structure, the geometry of the neurons and the recording location, etc. Such variation in phase relationships were evident during REM sleep and at low frequencies during RUN, but all sites became

uniformly synchronized across a broad range of frequencies once both sites have high power above 100 Hz.

The above correlational measures suggest the presence of an external, high-frequency contaminating source in the LFP signal, but they do not indicate when the contaminating events occurred. For a time- and frequency-resolved estimate of the intrusion of this synchronous component, we took the Pearson correlation coefficient *r* for 100 ms segments of two channels' signals at each time point, first filtering the signals in different frequency bands, and averaged this across many different channel pairs (red squares in Figure 5.2A) from the electrode array. The distributions of these channel pair-averaged *r* values for different frequency bands during RUN, REM, and SWS epochs are shown in Figure 5.2D. The *r* values of traditional LFP bands (theta, beta, gamma) stayed relatively low and were similarly distributed in all brain states. The higher frequency signals, however, diverged during RUN to become consistently much more synchronous. The *r* values remained low and were similarly distributed for all frequencies during REM and SWS.

Similar high-frequency signal components were found in three other animals with the same probe and recording system. Other data sets and/or recording setups displayed less of this contaminating signal, though it is rarely completely absent. For instance, in several simultaneous hippocampal-entorhinal recordings from our lab, the suspicious high-frequency power was more limited to the EC probe (Figures 5.1C and 5.3), perhaps because it is closer to muscles, or perhaps for technical reasons related to the characteristics or connections of that probe. The power covariations and synchrony

between sites were less prominent, though still apparent in the power and coherence spectra. The mean *r* value distribution differences between RUN and sleep was also smaller than in the large array recordings (compare Figures 5.2D and 5.4), though we would expect the *r* values for these recordings to be different because the electrode sites were all near cell body layers. In general, variations in recording configurations, behavioral tasks, and animals will all produce different recording characteristics, and we would like a more direct way to determine a link between this signal contamination to behavior.

5.2.2 Comparison of EMG recordings to intracranial recordings

We next implanted an EMG electrode in neck muscles of a rat with bilateral silicon probes in the hippocampus, and recorded during home-cage sleep and as the animal learned to run along a linear track for water reward. As in the entorhinal-hippocampal preparation described above, the probes had 8 shanks separated by 300 μm, with 8 contacts per probe spanning 140 μm vertically. Consequently, the recordings did not extend across multiple somatic-dendritic layers, so large phase changes and sink-source reversals that may be absent. Because electromyographic contamination would likely have multiple muscle sources, we could not expect clearly coherent signals between the intracranial and EMG probes, but this recording still allowed for a much more direct comparison of the intracranial signal to muscle activity.

Physiological high-frequency signals generated within the brain should be relatively local, rather than highly coherent across many shanks. Despite this, we again

found that substantial portions of the recording had high frequency components that were synchronous across all channels, even across hemispheres, especially during waking behavior. The strength of this component, as measured by the sliding-window correlations between the high-frequency signals (Section 5.2.1), was much more strongly correlated to EMG activity (measured by the 100-point-smoothed amplitude of the time derivative of EMG voltage, which we label $\Delta EMG/\Delta t$) than the animal's running speed ($r = 0.64$, $p < 10^{-4}$; Figure 5.5). Both cross-channel correlations and the EMG activity were also weakly theta-modulated (Figure 5.6) (Ledberg & Robbe 2011). Spectral power and average coherence between channels at high frequencies (>100 Hz) were also well correlated to $\Delta EMG/\Delta t$ (Figure 5.7). The correlation coefficient was higher for high-frequency power than for coherence, perhaps because any EMG contamination was strongly coherent, and more power did not make it proportionally more coherent.

5.2.3 Removal of EMG-related signal components

If pervasive artifactual signal components contaminate the upper spectral bands of LFPs, how can we properly detect true neural oscillations at high frequencies? With silicon electrode arrays that have a fixed geometry, we can use current source density (CSD) analysis, a common technique for estimating local membrane currents (Nicholson & Freeman 1975, Mitzdorf 1985, Pettersen et al. 2006, Montgomery et al. 2009, Łęski et al. 2011). In theory, the CSD provides a more reliable measure of coherence, because it removes volume conducted currents that can often contaminate LFP recordings (Sirota et al. 2008, Montgomery et al. 2009, Fernández-Ruiz et al. 2013). Applying CSD to the

large array hippocampal recordings (Figure 5.2) removed the major spectral differences between waking and sleeping states (Figure 5.8). Traditional CSD estimates are not perfect, however. They are inaccurate if: (i) the distance separating electrodes along the dimension of the CSD calculation is not fixed or uniform, or it is too large to obtain adequate spatial resolution; (ii) electrode impedances are inconsistent; (iii) the neural tissue and membrane currents are not approximately laminar in the recorded region (Nicholson & Freeman 1975). In general, the CSD is much more sensitive to recording anomalies and fluctuations in the distribution of current sources surrounding the electrodes, which results in substantially lower average coherence and correlations between sites (Figure 5.8 and 5.9C). It may be argued that this is a feature, giving more conservative estimates, but the results can be frustratingly obscure and/or inconsistent.

Most laboratories use wire bundles and tetrodes for neural recordings, making CSD estimation impractical. If the EMG component is synchronous on all channels, then perhaps simply re-referencing the recording to a local electrode will do the trick. In the hippocampus, the alveus is a relatively quiet site compared to the somatic and dendritic layers. Indeed, re-referencing our hippocampal recordings to the quietest electrode in the alveus did remove the EMG-related signal. But volume conducted LFPs or signals from passing axons will be introduced into the data, however, and re-referencing caused substantial amounts of spurious correlation and coherence throughout the gamma bands and higher (Figure 5.9B).

Another promising technique is independent component analysis (ICA) of LFPs from multielectrode arrays (Bell & Sejnowski 1995, Delorme & Makeig 2004, Makarov

et al. 2010, Fernández-Ruiz et al. 2012). This technique can identify and separate signal sources that are independently activated (though not necessarily uncorrelated) and have different spatial profiles, which is often the case for neural processes. If the spatial structure of a specific source is known, it may allow for the identification and characterization, and perhaps subtraction, of that component (Muthukumaraswamy 2013). We applied a common ICA algorithm (Makeig et al. 1997) to the wideband LFP signal over the entire electrode array shown in Figure 5.2. The fourth strongest component (as measured by the proportion of signal variance it accounts for) was uniquely spatially uniform and, consistent with our previous results, showed much stronger activity at high frequencies during RUN compared to either sleep state (Figure 5.10). Interestingly, below 5 Hz, this component had its highest power during SWS, most likely reflecting volume conduction of the slow oscillation from neocortex. In principle, and as is common practice in many EEG applications, one could apply ICA, remove this contaminating component from the signal, and proceed to analyze the remaining data. Alternatively, one can just analyze the other components. Unfortunately, without a high-density array of electrodes with a straightforward and rigid geometry, as well as some prior knowledge of the anatomy and physiology of the structure in which the probes are embedded, interpretation of the components can be very difficult (Fernández-Ruiz & Herreras 2013).

5.4 Discussion

Unsurprising to anyone who has recorded electrophysiological signals from awake, behaving animals (including humans), we have demonstrated that artifacts due to muscle activity are present in our data. What *is* surprising is the constancy with which an apparently muscle-related signal was present during waking behavior in several animals. Key features of this EMG component are: (1) broadband spectral power; (2) synchrony across large distances; (3) a close correspondence to activity in neck muscles. Our voltage references in each animal were skull screws located above the cerebellums. A better reference site, for the prevention of EMG contamination at least, may be somewhere deeper in the brain, such as the corpus callosum.

These results further illustrate the danger inherent in using LFPs to investigate high-frequency neural dynamics and communication. Above the traditional gamma band (30-80 Hz), the signal to noise ratio (SNR) becomes rather low, especially during waking behavior. Single unit analysis has a well-developed set of methods and criteria for extracting physiologically meaningful events (Lewicki 1998, Harris et al. 2000, Bartho et al. 2004, Schmitzer-Torbert et al. 2005, Quian Quiroga 2007, Hill et al. 2011). High-frequency oscillations can clearly be significant in the brain, perhaps during both normal or pathological events, (e.g., Buzsáki et al. 1992, Grenier et al. 2001, Staba et al. 2002, Barth 2003), and it is important to better understand their mechanisms of generation and their consequences. In this low SNR regime, however, pitfalls of recordings, analysis, and interpretation can arise (Bénar et al. 2010, Zanos et al. 2011, Muthukumaraswamy 2013).

We assume that the presence of low amplitude EMG contamination in intracranial recordings is not unique to our laboratory. While we do not presume to discount the main conclusions of previous studies, we wish to furnish a few examples in which EMG contamination does provide a simple explanation for some aspects of published results from our lab and others. First, Belluscio et al. (2012) showed depth profiles of each kind of gamma sub-band event, in addition to the sharp wave-ripple profile (Ylinen et al. 1995b). While it is possible for a local current source/sink distribution to generate non-reversing extracellular potentials (Mitzdorf 1985), most hippocampal LFP patterns do show phase changes and reversals along the somatodendritic axis (Ylinen et al. 1995b, Schomburg et al. 2012), which also occurs in the ripples and slow-medium gamma LFPs in (Belluscio et al. 2012). The triggered average of 90-150 Hz epsilon (fast gamma) events in (Belluscio et al. 2012), however, show nearly perfect phase synchrony along the entire depth of the recording (Figure 4). This is precisely what we would expect if many of the detected events, which are indeed detected during RUN in this case, are in fact volume-conducted EMG signals. Furthermore, in both that study and one of neocortical fast gamma signals in another laboratory (Scheffzük et al. 2011), the modulation of high frequency power by theta oscillations is greater during REM sleep than during running behavior. In the case of the hippocampal network investigated by Belluscio et al. (2012), this stands in contrast to the spiking activity within CA1, which they report is more theta modulated during RUN (Figure 2) [see also Section 4.3.1 and Mizuseki et al. (2011)]. So while the fast gamma activity during REM analyzed by Scheffzuk et al. (2011) and Belluscio et al. (2012) is legitimate, the degree of theta-coupling during REM compared

to RUN may in fact be biased by the presence of relatively tonic EMG contamination of this spectral band. Finally, the fast gamma (60-140 Hz) coherence between hippocampal CA1 and layer 3 of entorhinal cortex (EC3) reported by Colgin et al. (2009) is flat within this entire band [Figure 3 of Colgin et al. (2009)]. They do not show whether or not this coherence continues at the same level, or if it even increases, at higher frequencies than this. The CA1-EC3 coherence furthermore reflects synchronous voltage fluctuations in the two regions [Figure 2 of Colgin et al. (2009)]. Moreover, similar fast gamma coherence between CA1 and CA3 was found in at least one animal [Supplementary Figure 9 of Colgin et al. (2009)] and between CA3 and EC2 in three animals (Supplementary Figure 13 of Colgin et al.(2009)].

It will be important to gain a better understanding of how different recording configurations, from electrode design and placement to amplifier hardware, affect different parts of the spectrum, and to optimize these factors for the purposes of the study. Postprocessing techniques, such as ICA and CSD analysis, for the identification and removal of noise and artifacts may prove useful. But optimization of all these factors, and using electrodes (e.g., silicon probes) that enable straightforward application of ICA and CSD techniques, may be impractical for many studies. Using high-frequency extracellular features in addition to well isolated spikes therefore requires extensive validation. As we improve our ability to record from larger numbers of cells simultaneously, fine temporal coordination of neural activity will likely be better investigated with single units, recorded either electrophysiologically or optically.

Though we have focused here on EMG contamination of intracranial recordings, many of the concepts and methods for detection and removal that we suggested are also generally relevant for any volume-conducted signal component. Indeed, volume conduction of neural current is the basis of extracellular and extracranial electrical recording to begin with, and it was the motivation for developing CSD methods. As in much of modern science, from neurophysiology to gravitational wave interferometry, the fundamental challenge is to identify, isolate, and understand which aspects of the phenomena we measure are relevant and what physical processes underlie them. Only then can we use these quantifications to test our hypotheses and build a reliable theory.

5.5 Figures for Chapter 5

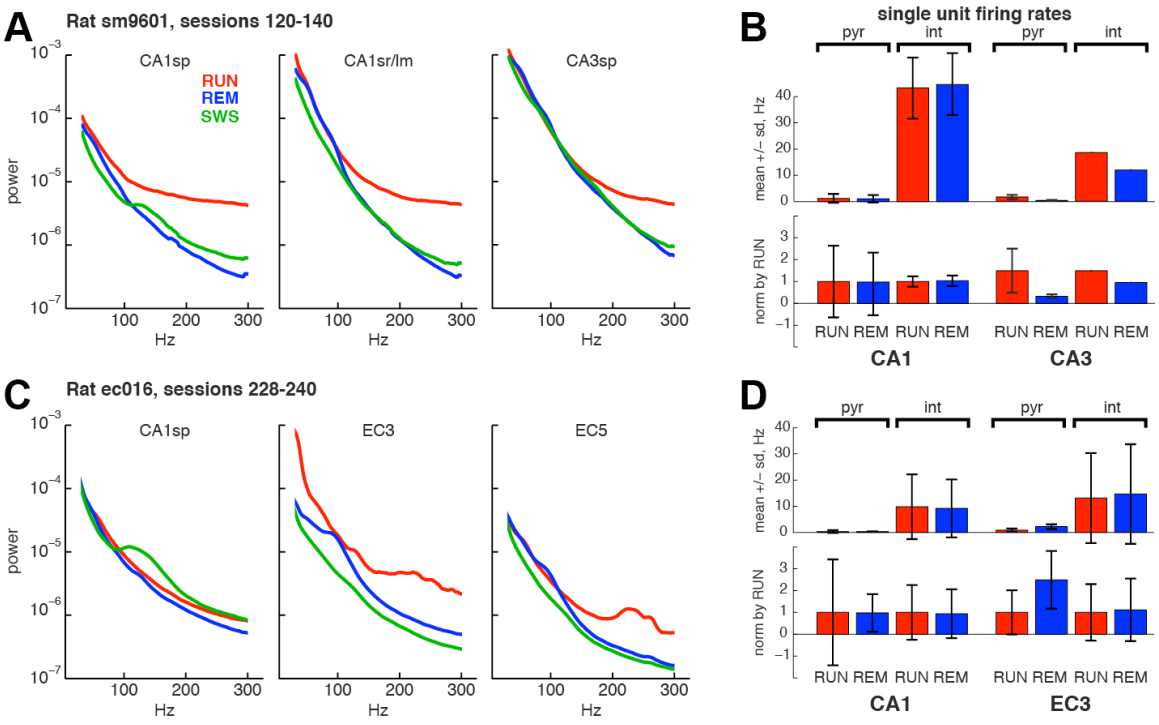

Figure 5.1. *Increases in high frequency power during locomotion cannot be explained by and single unit firing rates.* ***A,*** Power spectral densities (PSD) of LFPs recorded at three sites of a rectangular electrode array spanning CA1 to CA3 and DG of dorsal hippocampus in rat sm9601. Slow-wave sleep (SWS) exhibits a hump in the ripple band (120-200 Hz), but power above 100 Hz is substantially greater in all layers during RUN. ***B,*** Average firing rates of single units classified as pyramidal neurons (pyr) and interneurons (int) in CA1 and CA3 during RUN and REM for the same recording sessions as in *A*. ***C,*** PSDs in CA1 and layers 3 and 5 of entorhinal cortex (EC3 and EC5, respectively) recorded from rat ec016. The locomotion-related high frequency component appears to be largely absent from this CA1 site, but is present in the entorhinal cortex. ***D,*** Average single unit firing rates in CA1 and EC3 during the same sessions.

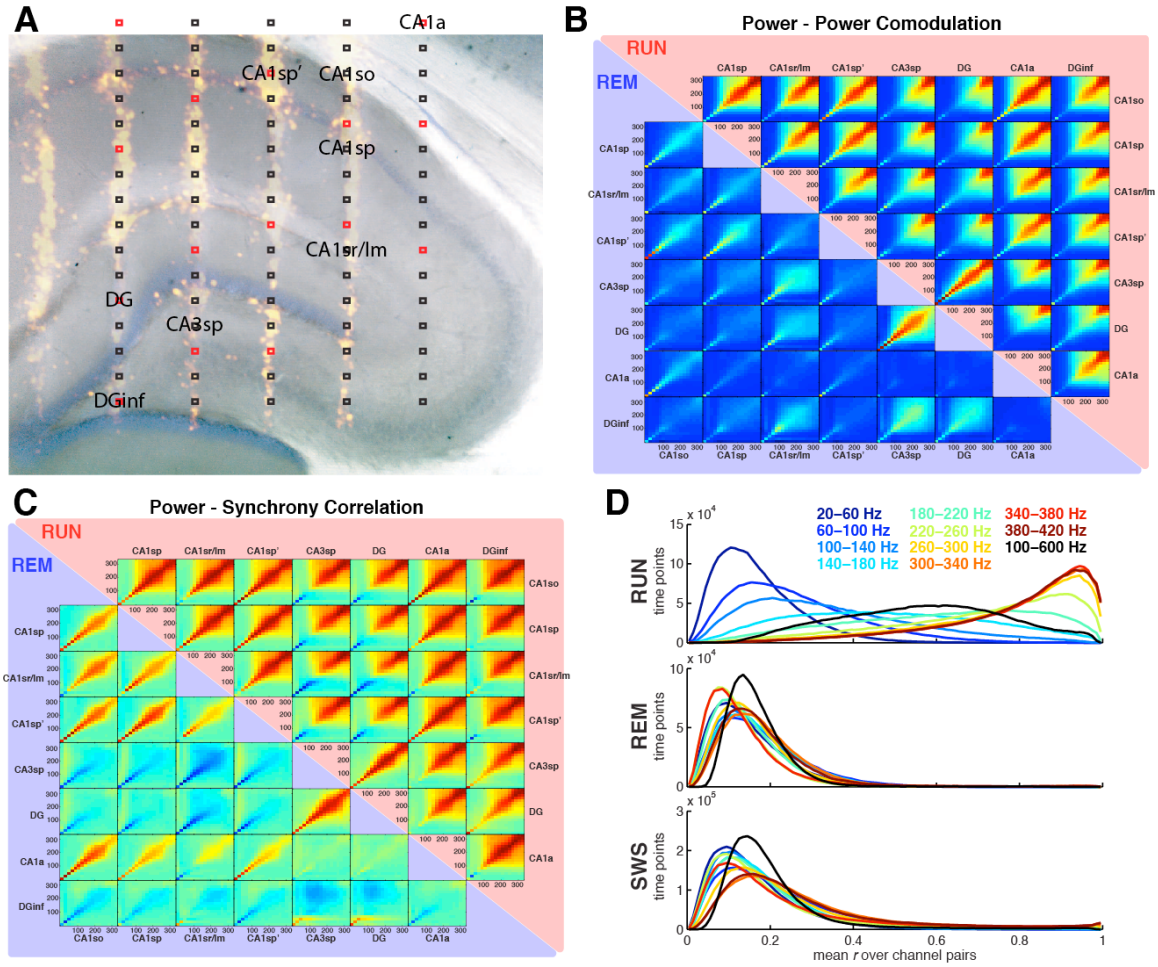

Figure 5.2. *Multilayer electrode arrays can be used to estimate the frequency- and time-resolved contamination of intracranial recording by external sources.* ***A,*** Schematic of the electrode locations within the dorsal hippocampus of rat sm9601. Red squares, channels used to calculate the mean correlations between channel pairs in sliding windows (panel *D*), which we used to estimate the instantaneous strength of the EMG signal component (Figure 5.5). ***B,*** Power-power correlation coefficients between wavelet powers at each frequency for several channel pairs (sites labeled in *A*), shown during RUN and REM. ***C,*** Power-synchrony correlation coefficients during RUN and REM for the same channel

pairs as in ***B***. ***D,*** The pair-averaged, sliding-window correlation coefficient distributions of all time points during RUN, REM, and SWS, calculated after bandpass filtering the raw LFP in the indicated frequency ranges.

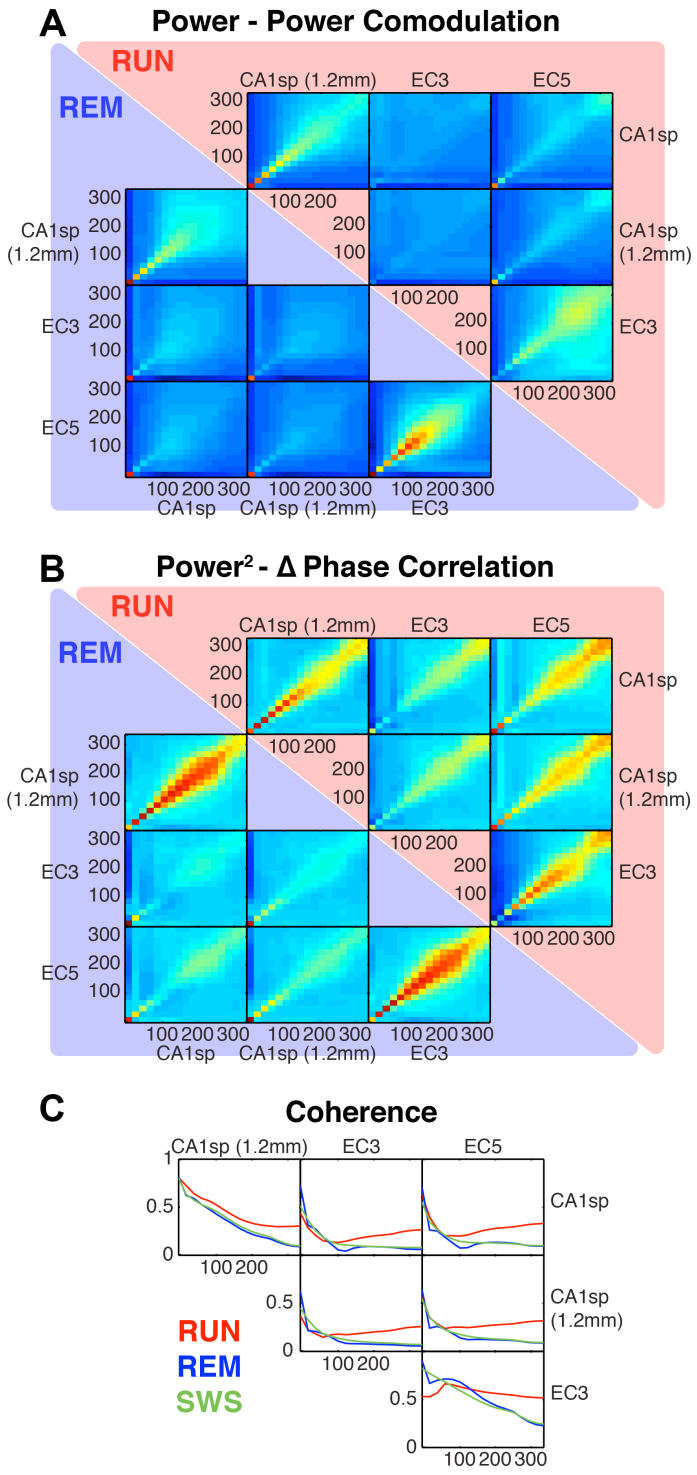

Figure 5.3. *EMG contamination is less pervasive in some recordings.* In several simultaneous CA1-EC recordings (rat ec016, Mizuseki et al. 2009), the EMG-component is less powerful, especially in the hippocampal probe. It is not absent, however, as

increases in high-frequency power (Figure 5.1), power-power correlations (*A*), power-synchrony correlations (*B*), and coherence (*C*). Again, the extra power and coherence is primarily above ~100 Hz.

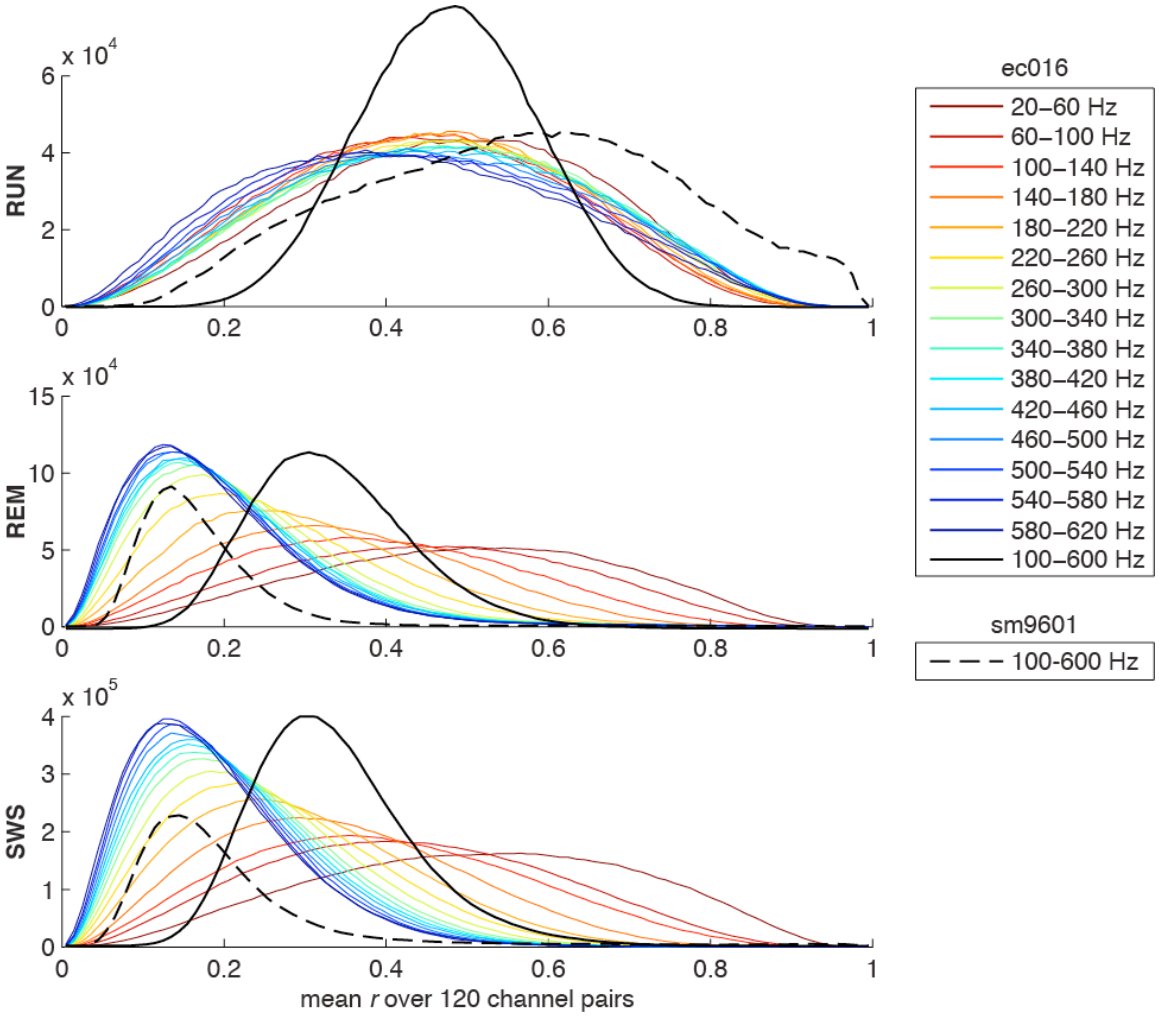

Figure 5.4. *Channel correlation values depend on recording configuration, but still exhibit qualitative differences between waking and sleep.* Distribution of mean correlation coefficient (*r*) values between channel pairs for 8 hippocampal (CA1) and 8 entorhinal channels (layers 3-5). Correlations were calculated over a sliding 50 ms window for bandpass filtered LFPs across a wide range of frequency bands. The distributions of high-

frequency *r* values from rat sm9601 (Figure 5.2) are included for comparison (dashed line).

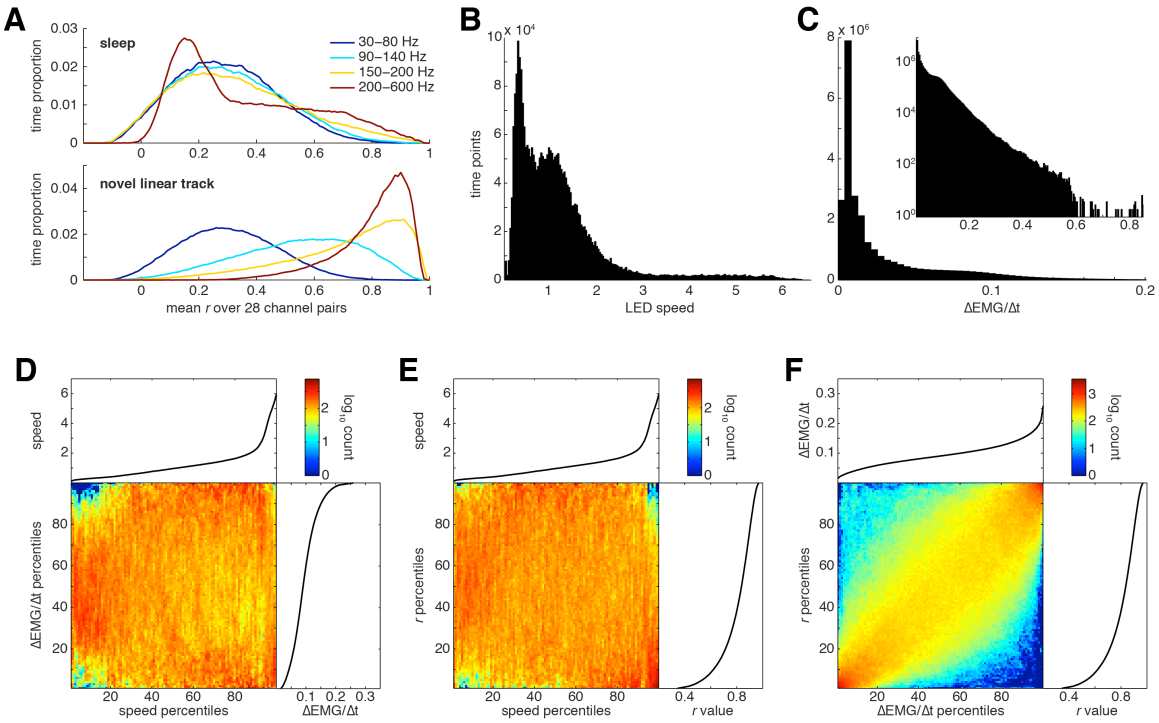

Figure 5.5. *Relationship of EMG to running and correlated high-frequency signal components.* ***A,*** Temporal distributions of sliding-window mean *r* values between 26 channel pairs (8 channels, 4 from each hemisphere) for bandpass-filtered LFPs during sleep and a linear track training session. ***B,*** Distribution of LED speed (units not yet converted to true speed) during the behavioral session. The distribution is bimodal, with many times of little head motion, periods of locomotion, and small bouts of higher speed head movements. ***C,*** Distribution of neck EMG activity, as measured by the smoothed amplitude (100-point running average of the absolute value) of the EMG derivative (ΔEMG/Δt). *Inset,* Counts shown on a log scale, and including all ΔEMG/Δt values. ***D,***

Relationship between speed and ΔEMG/Δt, shown using percentile rankings of speed and ΔEMG/Δt at each time point. The correlation coefficient between the actual speed and ΔEMG/Δt values is low, though highly significant ($r = 0.012$, $p < 10^{-4}$), but this value is less meaningful than the distribution shown here. ***E,*** Relationship between percentile rankings of speed and mean high-frequency (200-600 Hz) channel-pair correlations ($r = -0.20$, $p < 10^{-4}$). ***F,*** Relationship between percentile rankings of ΔEMG/Δt and mean high-frequency channel-pair correlations ($r = 0.64$, $p < 10^{-4}$).

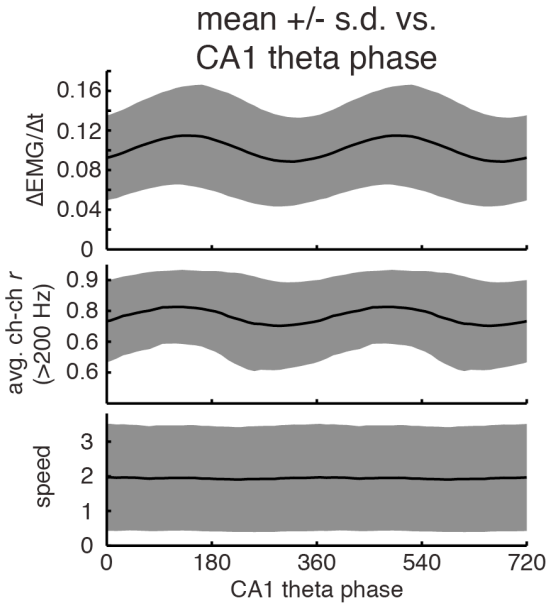

Figure 5.6. *Theta modulation of EMG signal.* Mean ± s.d. of ΔEMG/Δt, mean high-frequency channel-pair correlations, and speed, binned by theta phase. Neck muscle activity is theta-phase-modulated (Ledberg & Robbe 2011), and the EMG correlation with synchronous high-frequency signal components (Figure 5.5F) results in similar modulation of the mean *r* value. Horizontal LED motion (speed) is not theta modulated.

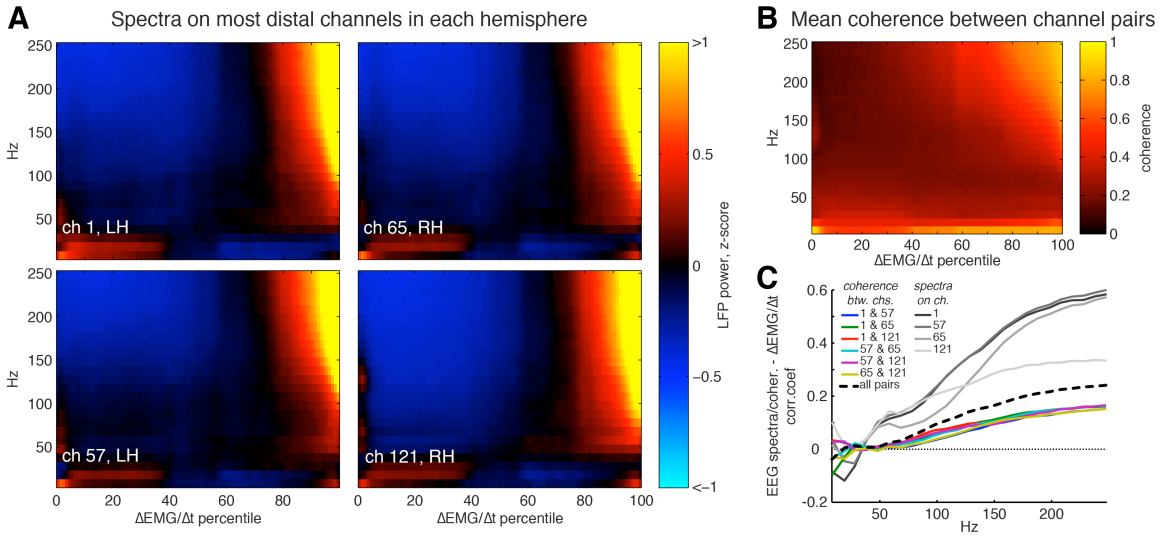

Figure 5.7. *Activity in neck muscles correlates with increased high frequency synchrony in intracranial recordings, even across hemispheres.* ***A,*** Broadband, high-frequency power in distal channels of both hemispheres (RH, right hemisphere; LF, left hemisphere) is greater for larger values of ΔEMG/Δt. ***B,*** Cross-channel coherence, averaged over the pairs in *A* also increases at high-frequencies for increasing ΔEMG/Δt. Higher coherence at theta frequencies (the bottom row in the plot is centered at 5 Hz) is related to EMG increasing during many periods of locomotion or exploration (e.g., rearing behaviors are accompanied by theta; Vanderwolf 1969). ***C,*** The correlation coefficients between ΔEMG/Δt and both power (on individual channels) and coherence (between channel pairs) increase with frequency.

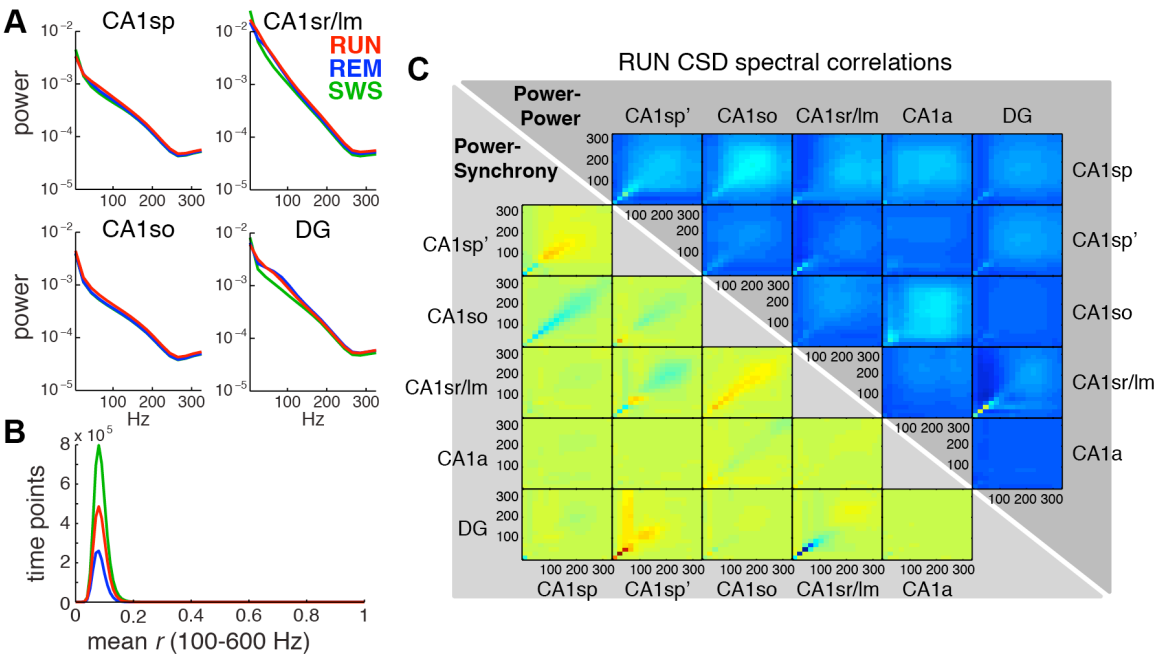

Figure 5.8. *Taking the CSD removes the common EMG component, but is susceptible to other measurement artifacts.* ***A,*** Average power spectra over each brain state show no significant difference at high frequencies. A problem is already apparent, however, because of the lack of a ripple-frequency bump in the SWS spectrum. ***B,*** The distributions of mean *r* values for the 100-600 Hz bandpass-filtered signal in each state are clustered around the same mean value. ***C,*** Power and coherence comodugrams during RUN no longer show ubiquitous coupling at high frequencies (compare with Figure 5.2B). Theta and gamma coherence is also dramatically reduced.

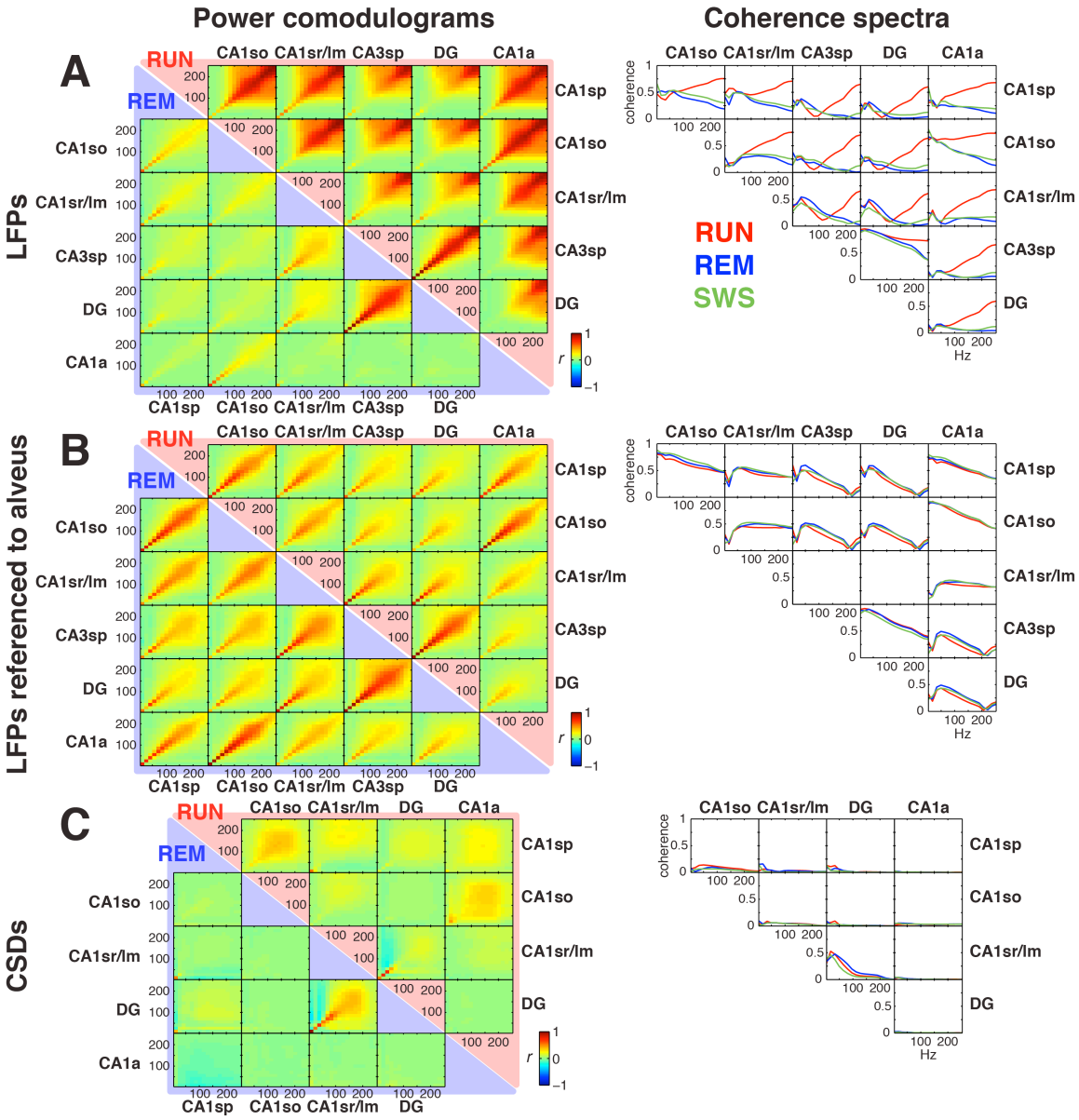

Figure 5.9. *Local referencing removes the EMG component but introduces spurious coherence and correlations.* Power comodulograms (left) and coherence spectra (right) between sites using the original LFPs (*A*), LFPs re-referenced to the alveus (just above the CA1a site) (*B*), and CSDs (*C*). The re-referenced LFPs no longer have the broadband EMG contamination, but instead pick up additional correlations and coherence throughout the gamma bands (in both RUN and REM). Applying the CSD formula also

removed EMG contamination, but the resulting CSDs likely have artificially low degrees of coherence and correlation between sites.

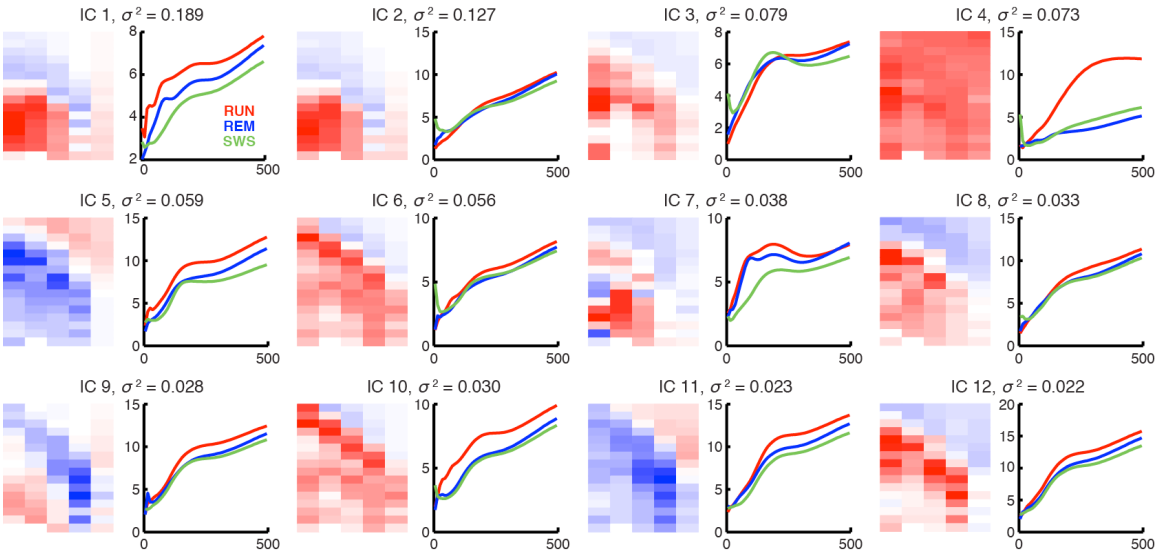

Figure 5.10. *ICA can separate EMG from local sources.* The 12 strongest independent components extracted from the broadband LFPs over the entire electrode array by an independent component analysis (ICA) algorithm (Makeig et al. 1997). A component's strength is defined as the proportion of the total variance σ^2 in the original data that it accounts for. The static spatial loading over the electrode array for each component is shown in the blue-red colormaps (blue = negative, red = positive; note, however, that the spatial loadings extracted by ICA can vary by a sign, in conjunction with the sign of the activation time series), alongside its normalized power spectra in each brain state. Normalization involves dividing the mean power at each frequency for a given component by the average power at that frequency for all channels in the original data. The fourth strongest component here (IC4) has a nearly uniform spatial profile, and is

substantially more powerful during RUN than during sleep for all frequencies greater than ~100 Hz.

IV. General discussion of broader implications

6. What high frequency signals may teach us about hippocampal physiology

Gamma oscillations have been observed in many brain regions, arise in slices with pharmacological excitation, and emerge in numerous network models. Persuasive evidence has been found that gamma coherence within sensory systems is important for integrating and attending to sensory stimuli (Fries 2009). In the hippocampus, gamma-band coherence has been shown to depend on behavior (Montgomery & Buzsàki 2007) and development (Shinohara et al. 2013). Yet, the hippocampus also exhibits a tendency towards self-organized internal dynamics (Pastalkova et al. 2008, Mizuseki et al. 2009). It receives sensory, contextual, and location-dependent information (Andersen et al. 2007, Moser et al. 2008, Eichenbaum et al. 2012, Krupic et al. 2012), and sends out a temporally compressed representation of location, heading, and context (O'Keefe & Recce 1993, Skaggs et al. 1996, Frank et al. 2000, Harris et al. 2002, Dragoi & Buzsáki 2006, Huxter et al. 2008, Manns & Eichenbaum 2009, Pfeiffer & Foster 2013, Komorowski et al. 2013, Kelemen & Fenton 2013). Our current understanding of spatial representation in the brain has the entorhinal cortex providing the hippocampus with a coordinate system and heading information (Hafting et al. 2005, Sargolini et al. 2006, Solstad et al. 2008, Krupic et al. 2012). This information is then used by the hippocampus

to refine the animal's estimate of its position, and tie objects, locations, and contexts into episodic and semantic memories (Eichenbaum et al. 2012, Buzsáki & Moser 2013, Kelemen & Fenton 2013). Place-specific firing is observed in both CA3 and CA1 (Muller et al. 1987, Barnes et al. 1990, Lee et al. 2004, Mizuseki et al. 2012), but CA3 input is not required for the formation of a place code in CA1 (Brun 2002, Leutgeb et al. 2004, Nakashiba et al. 2008). Instead, the highly recurrent network of CA3 thought to be critical for the associative role (memory recall) often ascribed to the hippocampus (Marr 1971, Hasselmo et al. 2002, Leutgeb & Leutgeb 2007).

In this conceptual model, then, we might expect intermittent events of strong CA3 input (CA3 pyramidal cells are more sparsely activated and more bursty, compared to CA1 pyramidal cells; Barnes et al. 1990, Leutgeb et al. 2004, Mizuseki et al. 2012), in which several activated cell assemblies initiate memory recall processes. Such an event might appear in CA1 as a strong increase in slow gamma power. In contrast, the more tonic EC3 input (Barnes et al. 1990) providing spatial reference information to CA1 seems less likely to take the form of events with especially strong fast gamma power or coupling. Rather, fast gamma/epsilon power is a good indicator of local network activation (Ray & Maunsell 2011a), and increases in these bands lines up in phase with most CA1 pyramidal cell spikes and out of phase with EC3 pyramidal cell spikes (Figures 4.1 and 4.2). Both EC3 and CA3 input to CA1 are important for spatial learning (Brun 2002, Remondes & Schuman 2004, Brun et al. 2008, Nakashiba et al. 2008, 2009, Suh et al. 2011), and somatic depolarization and various plasticity mechanisms are best engaged by cooperative activation of the two inputs (Remondes & Schuman 2002, Ang et

al. 2005, Jarsky et al. 2005, Takahashi & Magee 2009, Basu et al. 2013). These dendritic activation mechanisms are also slower, allowing for the diverse local interneuron population to shape the pyramidal cell response by modulating the strength and spread of depolarization (Koch et al. 1983, Miles et al. 1996, Buzsáki et al. 1996, Ang et al. 2005, Hao et al. 2009, Lovett-Barron et al. 2012, Gidon & Segev 2012), as well as the timing of somatic action potentials (Pouille & Scanziani 2001, Destexhe 2010, Renart et al. 2010, Losonczy et al. 2010, Royer et al. 2012).

Cell assemblies in the hippocampus have been shown to group their spikes into gamma-wave timescales, i.e., within 15-20 ms (Harris et al. 2003). Why then did we find such poor phase locking with gamma LFPs? First, assuming that the 15-20 ms assembly timescale represents the portion of the gamma cycle with increased excitability, this does corresponds to the slow gamma frequencies to which we did find phase-locking (Figure 8). The precise timing of pyramidal cells within each gamma cycle and the phase relationship with the LFP waves may be variable and dependent on the co-active pyramidal cells and interneurons, thereby reducing their modulation indices. In support of this hypothesis, even during in vitro gamma oscillations, which have fewer interfering LFP contributions, pyramidal cells in CA1 are subject to competition between excitation and inhibition, resulting in weak phase-locking of spikes (Zemankovics et al. 2013, Pietersen et al. 2013).

In general, LFPs typically reflect input at low frequencies, output at high frequencies, and a complicated combination in the middle. CA1 appears to lack circuit and cellular resonance properties that would allow it to respond coherently to medium/

fast gamma input (Pouille & Scanziani 2001, Vaidya & Johnston 2013), which may be by design. Its most important roles appear to be: (1) to integrate spatial, contextual, and internally generated input from EC3, CA3, and its other cortical and subcortical afferents; and (2) to transfer and consolidate memories into the neocortex with strong, synchronous, tetanus-like bursts in the form of sharp wave-ripples (SWR). The first role is best achieved if the network can listen to its afferents' inputs, allow them to interact and subject them to local computations in the pyramidal cell dendrites with the aid of feed-forward and feedback inhibition, and resist operating in an entrained or exclusive fashion with respect to these afferents. Having the inputs multiplexed in time and frequency, avoiding network properties that resonate with either input, and employing integration mechanisms that are either slower or tuned for the proper delays are all consistent with this function. For the second role, CA1 responds to large, internally generated population bursts from CA3 by synchronizing its output into a series of "mini population spikes" (Buzsáki 1986) that have a strong effect on their targets (Chrobak & Buzsáki 1996, Wierzynski et al. 2009, Peyrache et al. 2009). Mechanisms resulting in synchronized bursting of pyramidal cells (Figure 14) would facilitate this role. The fact that these spikes can collectively generate large, high-frequency LFP signatures (Chapter 3) allows for an easy way to recognize the CA1 pyramidal layer (Mizuseki et al. 2011, Berényi et al. 2014), as well as to detect significant memory-related events (Logothetis et al. 2012).

Moving forward, while gamma-band spectral profiles of CA1 LFPs may offer useful indicators of the occurrence of strong CA3 input, they can be sensitive to

the location of the electrodes, the characteristics of the recording circuit (e.g., electrical noise, EMG contamination), and spectral contamination across bands or by broadband events (e.g., spikes, chewing artifacts). More effective approaches will likely be to apply PCA or ICA decomposition (Delorme & Makeig 2004, Fernández-Ruiz & Herreras 2013, Lopes-dos-Santos et al. 2013), Bayesian decoders (Davidson et al. 2009, Kloosterman et al. 2014), support vector machine classifiers (Horikawa et al. 2013), or other techniques in a similar vein, to large-scale neural recordings to reduce the dimensionality of the data in a more meaningful manner. The analyses of neural population dynamics and interactions within the hippocampus, between the hippocampus and its afferents, and between CA1 and its efferents are sure to yield tremendous insights into the mechanisms of cell assembly coordination, the modification of neural circuits, the formation of long-term memories, and the role of the hippocampus in memory recall.

References

Acsády L, Kamondi A, Sik A, Freund T, Buzsàki G (1998) GABAergic cells are the major postsynaptic targets of mossy fibers in the rat hippocampus. J Neurosci 18:3386–3403

Ahrens MB, Orger MB, Robson DN, Li JM, Keller PJ (2013) Whole-brain functional imaging at cellular resolution using light-sheet microscopy. Nat Meth 10:413–420

Aika Y, Ren JQ, Kosaka K, Kosaka T (1994) Quantitative analysis of GABA-like-immunoreactive and parvalbumin-containing neurons in the CA1 region of the rat hippocampus using a stereological method, the disector. Exp Brain Res 99:267–276

Alonso A, García-Austt E (1987) Neuronal sources of theta rhythm in the entorhinal cortex of the rat. I. Laminar distribution of theta field potentials. Exp Brain Res 67:493–501

Amarasingham A, Harrison MT, Hatsopoulos NG, Geman S (2012) Conditional modeling and the jitter method of spike resampling. J Neurophysiol 107:517–531

Anastassiou CA, Montgomery SM, Barahona M, Buzsáki G, Koch C (2010) The effect of spatially inhomogeneous extracellular electric fields on neurons. J Neurosci 30:1925–1936

Anastassiou CA, Perin R, Markram H, Koch C (2011) Ephaptic coupling of cortical neurons. Nat Neurosci 14:217–223

Andersen P, Holmqvist B, Voorhoeve PE (1966) Excitatory synapses on hippocampal apical dendrites activated by entorhinal stimulation. Acta Physiol Scand 66:461–472

Andersen P, Morris RG, Amaral D, Bliss T, O'Keefe J (2007) The hippocampus book. New York: Oxford UP

Ang CW, Carlson GC, Coulter DA (2005) Hippocampal CA1 circuitry dynamically gates direct cortical inputs preferentially at theta frequencies. J Neurosci 25:9567–9580

Araque A, Navarrete M (2010) Glial cells in neuronal network function. Philos Trans R Soc Lond, B, Biol Sci 365:2375–2381

Atallah BV, Scanziani M (2009) Instantaneous modulation of gamma oscillation frequency by balancing excitation with inhibition. Neuron 62:566–577

Axmacher N, Henseler MM, Jensen O, Weinreich I, Elger CE, Fell J (2010) Cross-frequency coupling supports multi-item working memory in the human hippocampus. Proc Natl Acad Sci USA 107:3228–3233

Barnes CA, McNaughton BL, Mizumori SJ, Leonard BW, Lin LH (1990) Comparison of spatial and temporal characteristics of neuronal activity in sequential stages of hippocampal processing. Prog Brain Res 83:287–300

Barth DS (2003) Submillisecond synchronization of fast electrical oscillations in neocortex. J Neurosci 23:2502–2510

Bartho P, Hirase H, Monconduit L, Zugaro M, Harris KD, Buzsàki G (2004) Characterization of neocortical principal cells and Interneurons by network interactions and extracellular features. J Neurophysiol 92:600–608

Basu J, Srinivas KV, Cheung SK, Taniguchi H, Huang ZJ, Siegelbaum SA (2013) A cortico-hippocampal learning rule shapes inhibitory microcircuit activity to enhance hippocampal information flow. Neuron 79:1208–1221

Battaglia FP, Sutherland GR, McNaughton BL (2004) Hippocampal sharp wave bursts coincide with neocortical “up-state” transitions. Learning & Memory 11:697–704

Bazelot M, Dinocourt C, Cohen I, Miles R (2010) Unitary inhibitory field potentials in the CA3 region of rat hippocampus. J Physiol 588:2077–2090

Bell AJ, Sejnowski TJ (1995) An information-maximization approach to blind separation and blind deconvolution. Neural Comput 7:1129–1159

Belluscio MA, Mizuseki K, Schmidt R, Kempter R, Buzsáki G (2012) Cross-frequency phase-phase coupling between θ and γ oscillations in the hippocampus. J Neurosci 32:423–435

Berens P (2009) CircStat: a MATLAB toolbox for circular statistics. Journal of Statistical Software 31

Berényi A, Somogyvari Z, Nagy AJ, Roux L, Long JD, Fujisawa S, Stark E, Leonardo A, Harris TD, Buzsáki G (2014) Large-scale, high-density (up to 512 channels) recording of local circuits in behaving animals. J Neurophysiol 111:1132–1149

Bezaire MJ, Soltesz I (2013) Quantitative assessment of CA1 local circuits: Knowledge base for interneuron-pyramidal cell connectivity. Hippocampus:n–a–n–a

Bédard C, Rodrigues S, Roy N, Contreras D, Destexhe A (2010) Evidence for frequency-dependent extracellular impedance from the transfer function between extracellular and intracellular potentials: intracellular-LFP transfer function. J Comp Neurosci 29:389–403

Bénar CG, Chauvière L, Bartolomei F, Wendling F (2010) Pitfalls of high-pass filtering for detecting epileptic oscillations: a technical note on “false” ripples. Clin Neurophysiol 121:301–310

Bi G, Poo M (2001) Synaptic modification by correlated activity: Hebb's postulate revisited. Annu Rev Neurosci 24:139–166

Bliss TV, Lomo T (1973) Long-lasting potentiation of synaptic transmission in the dentate area of the anaesthetized rabbit following stimulation of the perforant path. J Physiol 232:331–356

Blumenfeld H (2005) Cellular and network mechanisms of spike-wave seizures. Epilepsia 46 Suppl 9:21–33

Bock DD, Lee W-CA, Kerlin AM, Andermann ML, Hood G, Wetzel AW, Yurgenson S, Soucy ER, Kim HS, Reid RC (2011) Network anatomy and in vivo physiology of visual cortical neurons. Nature 471:177–182

Boss BD, Turlejski K, Stanfield BB, Cowan WM (1987) On the numbers of neurons in fields CA1 and CA3 of the hippocampus of Sprague-Dawley and Wistar rats. Brain Res 406:280–287

J. M. Bower and D. Beeman (1998) The Book of GENESIS: Exploring Realistic Neural Models with the GEneral NEural SImulation System, 2nd Ed. New York: Springer-Verlag.

Bragin A, Benassi SK, Kheiri F, Engel J (2011) Further evidence that pathologic high-frequency oscillations are bursts of population spikes derived from recordings of identified cells in dentate gyrus. Epilepsia 52:45–52

Bragin A, Engel J, Wilson CL, Fried I, Buzsáki G (1999) High-frequency oscillations in human brain. Hippocampus 9:137–142

Bragin A, Jandó G, Nádasdy Z, Hetke J, Wise K, Buzsáki G (1995) Gamma (40-100 Hz) oscillation in the hippocampus of the behaving rat. J Neurosci 15:47–60

Brankack J, Stewart M, Fox SE (1993) Current source density analysis of the hippocampal theta rhythm: associated sustained potentials and candidate synaptic generators. Brain Res 615:310–327

Broicher T, Malerba P, Dorval AD, Borisyuk A, Fernandez FR, White JA (2012) Spike Phase Locking in CA1 Pyramidal Neurons Depends on Background Conductance and Firing Rate. J Neurosci 32:14374–14388

Brun VH (2002) Place Cells and Place Recognition Maintained by Direct Entorhinal-Hippocampal Circuitry. Science 296:2243–2246

Brun VH, Leutgeb S, Wu H-Q, Schwarcz R, Witter MP, Moser EI, Moser M-B (2008) Impaired spatial representation in CA1 after lesion of direct input from entorhinal cortex. Neuron 57:290–302

Brunel N, Wang X (2003) What determines the frequency of fast network oscillations with irregular neural discharges? I. Synaptic dynamics and excitation-inhibition balance. J Neurophysiol 90:415–430

Buhl DL, Buzsáki G (2005) Developmental emergence of hippocampal fast-field “ripple” oscillations in the behaving rat pups. Neuroscience 134:1423–1430

Buhl DL, Harris KD, Hormuzdi SG, Monyer H, Buzsàki G (2003) Selective impairment of hippocampal gamma oscillations in connexin-36 knock-out mouse in vivo. J Neurosci 23:1013–1018

Buhl EH, Cobb SR, Halasy K, Somogyi P (1995) Properties of unitary IPSPs evoked by anatomically identified basket cells in the rat hippocampus. Eur J Neurosci 7:1989–2004

Buzsàki G (1984) Feed-forward inhibition in the hippocampal formation. Prog Neurobiol 22:131–153

Buzsáki G (1986) Hippocampal sharp waves: their origin and significance. Brain Res 398:242–252

Buzsáki G (1989) Two-stage model of memory trace formation: a role for “noisy” brain states. Neuroscience 31:551–570

Buzsáki G (2002) Theta oscillations in the hippocampus. Neuron 33:325–340

Buzsáki G (2004) Large-scale recording of neuronal ensembles. Nat Neurosci 7:446–451

Buzsáki G (2006) Rhythms of the brain. New York: Oxford UP

Buzsáki G (2010) Neural syntax: cell assemblies, synapsembles, and readers. Neuron 68:362–385

Buzsáki G, Draguhn A (2004) Neuronal oscillations in cortical networks. Science 304:1926–1929

Buzsáki G, Moser EI (2013) Memory, navigation and theta rhythm in the hippocampal-entorhinal system. Nat Neurosci 16:130–138

Buzsáki G, Silva FLD (2012) High frequency oscillations in the intact brain. Prog Neurobiol

Buzsáki G, Wang X-J (2012) Mechanisms of Gamma Oscillations. Annu Rev Neurosci

Buzsáki G, Anastassiou CA, Koch C (2012) The origin of extracellular fields and currents - EEG, ECoG, LFP and spikes. Nat Rev Neurosci 13:407–420

Buzsáki G, Czopf J, Kondákor I, Kellényi L (1986) Laminar distribution of hippocampal rhythmic slow activity (RSA) in the behaving rat: current-source density analysis, effects of urethane and atropine. Brain Res 365:125–137

Buzsáki G, Horváth Z, Urioste R, Hetke J, Wise K (1992) High-frequency network oscillation in the hippocampus. Science 256:1025–1027

Buzsáki G, Leung L-WS, Vanderwolf CH (1983) Cellular bases of hippocampal EEG in the behaving rat. Brain Res 287:139–171

Buzsáki G, Logothetis N, Singer W (2013) Scaling brain size, keeping timing: evolutionary preservation of brain rhythms. Neuron 80:751–764

Buzsáki G, Penttonen M, Nádasdy Z, Bragin A (1996) Pattern and inhibition-dependent invasion of pyramidal cell dendrites by fast spikes in the hippocampus in vivo. Proc Natl Acad Sci USA 93:9921–9925

Calvin WH (1969) Dendritic spikes revisited. Science 166:637–638

Canolty RT, Knight RT (2010) The functional role of cross-frequency coupling. Trends in Cognitive Sciences 14:506–515

Canolty RT, Edwards E, Dalal SS, Soltani M, Nagarajan SS, Kirsch HE, Berger MS, Barbaro NM, Knight RT (2006) High gamma power is phase-locked to theta oscillations in human neocortex. Science 313:1626–1628

Cardin JA, Carlén M, Meletis K, Knoblich U, Zhang F, Deisseroth K, Tsai L-H, Moore CI (2009) Driving fast-spiking cells induces gamma rhythm and controls sensory responses. Nature 459:663–667

Carnevale NT, Hines ML (2006) The NEURON book. Cambridge, UK: Cambridge UP

Carr MF, Jadhav SP, Frank LM (2011) Hippocampal replay in the awake state: a potential substrate for memory consolidation and retrieval. Nat Neurosci 14:147–153

Cenquizca LA, Swanson LW (2007) Spatial organization of direct hippocampal field CA1 axonal projections to the rest of the cerebral cortex. Brain Res Rev 56:1–26

Chemla S, Chavane F (2010) Journal of Physiology - Paris. Journal of Physiology - Paris 104:40–50

Chen T-W, Wardill TJ, Sun Y, Pulver SR, Renninger SL, Baohan A, Schreiter ER, Kerr RA, Orger MB, Jayaraman V, Looger LL, Svoboda K, Kim DS (2013) Ultrasensitive fluorescent proteins for imaging neuronal activity. Nature 499:295–300

Chevaleyre V, Siegelbaum SA (2010) Strong CA2 pyramidal neuron synapses define a powerful disynaptic cortico-hippocampal loop. Neuron 66:560–572

Chrobak JJ, Buzsáki G (1996) High-frequency oscillations in the output networks of the hippocampal-entorhinal axis of the freely behaving rat. J Neurosci 16:3056–3066

Chrobak JJ, Buzsáki G (1998) Gamma oscillations in the entorhinal cortex of the freely behaving rat. J Neurosci 18:388–398

Clark J, Plonsey R (1966) A mathematical evaluation of the core conductor model. Biophys J 6:95–112

Clark J, Plonsey R (1968) The extracellular potential field of the single active nerve fiber in a volume conductor. Biophys J 8:842–864

Cohen SD, Hindmarsh AC (1996) CVODE, a stiff/nonstiff ODE solver in C. Computers in physics 10:138–143

Colgin LL, Moser EI (2010) Gamma oscillations in the hippocampus. Physiology (Bethesda) 25:319–329

Colgin LL, Denninger T, Fyhn M, Hafting T, Bonnevie T, Jensen O, Moser M-B, Moser EI (2009) Frequency of gamma oscillations routes flow of information in the hippocampus. Nature 462:353–357

Comon P (1994) Independent component analysis, a new concept? Signal processing 36:287–314

Csicsvari J, Hirase H, Czurko A, Buzsáki G (1998) Reliability and state dependence of pyramidal cell-interneuron synapses in the hippocampus: an ensemble approach in the behaving rat. Neuron 21:179–189

Csicsvari J, Hirase H, Czurkó A, Mamiya A, Buzsáki G (1999a) Oscillatory coupling of hippocampal pyramidal cells and interneurons in the behaving Rat. J Neurosci 19:274–287

Csicsvari J, Hirase H, Czurkó A, Mamiya A, Buzsáki G (1999b) Fast network oscillations in the hippocampal CA1 region of the behaving rat. J Neurosci 19:RC20

Csicsvari J, Hirase H, Mamiya A, Buzsáki G (2000) Ensemble patterns of hippocampal CA3-CA1 neurons during sharp wave-associated population events. Neuron 28:585–594

Csicsvari J, Jamieson B, Wise KD, Buzsáki G (2003) Mechanisms of gamma oscillations in the hippocampus of the behaving rat. Neuron 37:311–322

Davidson TJ, Kloosterman F, Wilson MA (2009) Hippocampal replay of extended experience. Neuron 63:497–507

Delorme A, Makeig S (2004) EEGLAB: an open source toolbox for analysis of single-trial EEG dynamics including independent component analysis. J Neurosci Methods 134:9–21

Deshmukh SS, Yoganarasimha D, Voicu H, Knierim JJ (2010) Theta Modulation in the Medial and the Lateral Entorhinal Cortices. J Neurophysiol 104:994–1006

Destexhe A (2010) Inhibitory “noise.” Front Cell Neurosci 4:9

Destexhe A, Rudolph M, Paré D (2003) The high-conductance state of neocortical neurons in vivo. Nat Rev Neurosci 4:739–751

Diba K, Buzsáki G (2007) Forward and reverse hippocampal place-cell sequences during ripples. Nat Neurosci 10:1241–1242

Diba K, Buzsáki G (2008) Hippocampal network dynamics constrain the time lag between pyramidal cells across modified environments. J Neurosci 28:13448–13456

Dougherty KA, Islam T, Johnston D (2012) Intrinsic excitability of CA1 pyramidal neurones from the rat dorsal and ventral hippocampus. J Physiol 590:5707–5722

Dragoi G, Buzsáki G (2006) Temporal encoding of place sequences by hippocampal cell assemblies. Neuron 50:145–157

Draguhn A, Traub RD, Schmitz D, Jefferys JG (1998) Electrical coupling underlies high-frequency oscillations in the hippocampus in vitro. Nature 394:189–192

Eichenbaum H, Sauvage M, Fortin N, Komorowski R, Lipton P (2012) Towards a functional organization of episodic memory in the medial temporal lobe. Neuroscience and biobehavioral reviews 36:1597–1608

Einevoll GT, Kayser C, Logothetis NK, Panzeri S (2013) Modelling and analysis of local fieldpotentials for studying the function ofcortical circuits. Nat Rev Neurosci 14:770–785

Engel AK, Fries P, Singer W (2001) Dynamic predictions: Oscillations and synchrony in top–down processing. Nat Rev Neurosci 2:704–716

Fanselow MS, Dong H-W (2010) Are the dorsal and ventral hippocampus functionally distinct structures? Neuron 65:7–19

Fernández-Ruiz A, Herreras O (2013) Identifying the synaptic origin of ongoing neuronal oscillations through spatial discrimination of electric fields. Front Comput Neurosci 7:5

Fernández-Ruiz A, Makarov VA, Benito N, Herreras O (2012) Schaffer-Specific Local Field Potentials Reflect Discrete Excitatory Events at Gamma Frequency That May Fire Postsynaptic Hippocampal CA1 Units. J Neurosci 32:5165–5176

Fernández-Ruiz A, Muñoz S, Sancho M, Makarova J, Makarov VA, Herreras O (2013) Cytoarchitectonic and dynamic origins of giant positive local field potentials in the dentate gyrus. J Neurosci 33:15518–15532

Fisahn A, Pike FG, Buhl EH, Paulsen O (1998) Cholinergic induction of network oscillations at 40 Hz in the hippocampus in vitro. Nature 394:186–189

Foffani G, Uzcategui YG, Gal B, Menendez de la Prida L (2007) Reduced spike-timing reliability correlates with the emergence of fast ripples in the rat epileptic hippocampus. Neuron 55:930–941

Forro T, Valenti O, Lasztoczi B, Klausberger T (2013) Temporal Organization of GABAergic Interneurons in the Intermediate CA1 Hippocampus During Network Oscillations. Cereb Cortex

Fox SE, Ranck JB (1975) Localization and anatomical identification of theta and complex spike cells in dorsal hippocampal formation of rats. Exp Neurol 49:299–313

Fox SE, Wolfson S, Ranck JB (1986) Hippocampal theta rhythm and the firing of neurons in walking and urethane anesthetized rats. Exp Brain Res 62:495–508

Frank LM, Brown EN, Wilson M (2000) Trajectory encoding in the hippocampus and entorhinal cortex. Neuron 27:169–178

Freeman WJ, Rogers LJ, Holmes MD, Silbergeld DL (2000) Spatial spectral analysis of human electrocorticograms including the alpha and gamma bands. J Neurosci Methods 95:111–121

Freund TF, Buzsáki G (1996) Interneurons of the hippocampus. Hippocampus 6:347–470

Freund TF, Katona I (2007) Perisomatic inhibition. Neuron 56:33–42

Fries P (2009) Neuronal gamma-band synchronization as a fundamental process in cortical computation. Annu Rev Neurosci 32:209–224

Gao J, Yang Y, Sun J, Yu G (2010) Automatic removal of various artifacts from EEG signals using combined methods. J Clin Neurophysiol 27:312–320

Gaona CM, Sharma M, Freudenburg ZV, Breshears JD, Bundy DT, Roland J, Barbour DL, Schalk G, Leuthardt EC (2011) Nonuniform high-gamma (60-500 Hz) power changes dissociate cognitive task and anatomy in human cortex. J Neurosci 31:2091–2100

Gerstner W, Sprekeler H, Deco G (2012) Theory and simulation in neuroscience. Science 338:60–65

Gidon A, Segev I (2012) Principles governing the operation of synaptic inhibition in dendrites. Neuron 75:330–341

Girardeau G, Benchenane K, Wiener SI, Buzsáki G, Zugaro MB (2009) Selective suppression of hippocampal ripples impairs spatial memory. Nat Neurosci 12:1222–1223

Glickfeld LL, Roberts JD, Somogyi P, Scanziani M (2009) Interneurons hyperpolarize pyramidal cells along their entire somatodendritic axis. Nat Neurosci 12:21–23

Gold C (2007) Biophysics of Extracellular Action Potentials. PhD Thesis. Pasadena, CA: Caltech.

Gold C, Henze DA, Koch C (2007) Using extracellular action potential recordings to constrain compartmental models. J Comp Neurosci 23:39–58

Gold C, Henze DA, Koch C, Buzsáki G (2006) On the origin of the extracellular action potential waveform: A modeling study. J Neurophysiol 95:3113–3128

Golding NL, Mickus TJ, Katz Y, Kath WL, Spruston N (2005) Factors mediating powerful voltage attenuation along CA1 pyramidal neuron dendrites. J Physiol 568:69–82

Goncharova II, McFarland DJ, Vaughan TM, Wolpaw JR (2003) EMG contamination of EEG: spectral and topographical characteristics. Clin Neurophysiol 114:1580–1593

Goto T, Hatanaka R, Ogawa T, Sumiyoshi A, Riera J, Kawashima R (2010) An evaluation of the conductivity profile in the somatosensory barrel cortex of Wistar rats. J Neurophysiol 104:3388–3412

Goutagny R, Jackson J, Williams S (2009) Self-generated theta oscillations in the hippocampus. Nat Neurosci

Graupner M, Reyes AD (2013) Synaptic Input Correlations Leading to Membrane Potential Decorrelation of Spontaneous Activity in Cortex. J Neurosci 33:15075–15085

Grenier F, Timofeev I, Steriade M (2001) Focal synchronization of ripples (80-200 Hz) in neocortex and their neuronal correlates. J Neurophysiol 86:1884–1898

Gulyás AI, Markram H, Emri Z, Freund TF (1999) Total number and ratio of excitatory and inhibitory synapses converging onto single interneurons of different types in the CA1 area of the rat hippocampus. J Neurosci 19:10082–10097

Gulyás AI, Miles R, Sík A, Tóth K, Tamamaki N, Freund TF (1993) Hippocampal pyramidal cells excite inhibitory neurons through a single release site. Nature 366:683–687

Gustafsson B, Wigström H (1981) Evidence for two types of afterhyperpolarization in CA1 pyramidal cells in the hippocampus. Brain Res 206:462–468

Hafting T, Fyhn M, Bonnevie T, Moser M-B, Moser EI (2008) Hippocampus-independent phase precession in entorhinal grid cells. Nature 453:1248–1252

Hafting T, Fyhn M, Molden S, Moser M-B, Moser EI (2005) Microstructure of a spatial map in the entorhinal cortex. Nature 436:801–806

Han X, Chen M, Wang F, Windrem M, Wang S, Shanz S, Xu Q, Oberheim NA, Bekar L, Betstadt S, Silva AJ, Takano T, Goldman SA, Nedergaard M (2013) Forebrain engraftment by human glial progenitor cells enhances synaptic plasticity and learning in adult mice. Cell Stem Cell 12:342–353

Hao J, Wang X-D, Dan Y, Poo M-M, Zhang X-H (2009) An arithmetic rule for spatial summation of excitatory and inhibitory inputs in pyramidal neurons. Proc Natl Acad Sci USA 106:21906–21911

Harris KD, Csicsvari J, Hirase H, Dragoi G, Buzsáki G (2003) Organization of cell assemblies in the hippocampus. Nature 424:552–556

Harris KD, Henze DA, Csicsvari J, Hirase H, Buzsáki G (2000) Accuracy of tetrode spike separation as determined by simultaneous intracellular and extracellular measurements. J Neurophysiol 84:401–414

Harris KD, Henze DA, Hirase H, Leinekugel X, Dragoi G, Czurkó A, Buzsáki G (2002) Spike train dynamics predicts theta-related phase precession in hippocampal pyramidal cells. Nature 417:738–741

Hartley T, Lever C, Burgess N, O'Keefe J (2014) Space in the brain: how the hippocampal formation supports spatial cognition. Philosophical Transactions of the Royal Society B: Biological Sciences 369:20120510

Hasenstaub A, Shu Y, Haider B, Kraushaar U, Duque A, McCormick DA (2005) Inhibitory postsynaptic potentials carry synchronized frequency information in active cortical networks. Neuron 47:423–435

Hasselmo ME, Bodelón C, Wyble BP (2002) A proposed function for hippocampal theta rhythm: separate phases of encoding and retrieval enhance reversal of prior learning. Neural Comput 14:793–817

Hazan L, Zugaro M, Buzsáki G (2006) Klusters, NeuroScope, NDManager: a free software suite for neurophysiological data processing and visualization. J Neurosci Methods 155:207–216

Hájos N, Paulsen O (2009) Network mechanisms of gamma oscillations in the CA3 region of the hippocampus. Neural Netw 22:1113–1119

Hebb DO (1949) The organization of behaviour. New York: Wiley.

Hellerstein D (1969) Cable theory and gross potential analysis. Science 166:638–639

Henze DA, Borhegyi Z, Csicsvari J, Mamiya A, Harris KD, Buzsáki G (2000) Intracellular features predicted by extracellular recordings in the hippocampus in vivo. J Neurophysiol 84:390–400

Hestrin S, Nicoll RA, Perkel DJ, Sah P (1990) Analysis of excitatory synaptic action in pyramidal cells using whole-cell recording from rat hippocampal slices. J Physiol 422:203–225

Hill DN, Mehta SB, Kleinfeld D (2011) Quality metrics to accompany spike sorting of extracellular signals. J Neurosci 31:8699–8705

Hines ML, Morse T, Migliore M, Carnevale NT, Shepherd GM (2004) ModelDB: A database to support computational neuroscience. J Comp Neurosci 17:7–11

Hock BJ, Bunsey MD (1998) Differential effects of dorsal and ventral hippocampal lesions. J Neurosci 18:7027–7032

Hodgkin A, Huxley AF (1952) A quantitative description of membrane current and its application to conduction and excitation in nerve. J Physiol 117:500–544

Holsheimer J, Boer J, Lopes da Silva FH, van Rotterdam A (1982) The double dipole model of theta rhythm generation: simulation of laminar field potential profiles in dorsal hippocampus of the rat. Brain Res 235:31–50

Holt G (1998) A Critical Reexamination of Some Assumptions and Implications of Cable Theory in Neurobiology. PhD Thesis:1–132

Holt GR, Koch C (1999) Electrical interactions via the extracellular potential near cell bodies. J Comp Neurosci 6:169–184

Horikawa T, Tamaki M, Miyawaki Y, Kamitani Y (2013) Neural decoding of visual imagery during sleep. Science 340:639–642

Hu H, Ma Y, Agmon A (2011) Submillisecond Firing Synchrony between Different Subtypes of Cortical Interneurons Connected Chemically But Not Electrically. J Neurosci 31:3351–3361

Hu H, Martina M, Jonas P (2010) Dendritic mechanisms underlying rapid synaptic activation of fast-spiking hippocampal interneurons. Science 327:52–58

Huxter JR, Senior TJ, Allen K, Csicsvari J (2008) Theta phase–specific codes for two-dimensional position, trajectory and heading in the hippocampus. Nat Neurosci 11:587–594

Hyman JM, Wyble BP, Goyal V, Rossi CA, Hasselmo ME (2003) Stimulation in hippocampal region CA1 in behaving rats yields long-term potentiation when delivered to the peak of theta and long-term depression when delivered to the trough. J Neurosci 23:11725–11731

Izhikevich EM (2000) Neural excitability, spiking and bursting. International Journal of Bifurcation and Chaos 10:1171–1266

Jackson J, Goutagny R, Williams S (2011) Fast and slow gamma rhythms are intrinsically and independently generated in the subiculum. J Neurosci 31:12104–12117

Jacobs J, Kahana MJ (2009) Neural representations of individual stimuli in humans revealed by gamma-band electrocorticographic activity. J Neurosci 29:10203–10214

Jadhav SP, Kemere C, German PW, Frank LM (2012) Awake hippocampal sharp-wave ripples support spatial memory. Science 336:1454–1458

Jarsky T, Roxin A, Kath WL, Spruston N (2005) Conditional dendritic spike propagation following distal synaptic activation of hippocampal CA1 pyramidal neurons. Nat Neurosci 8:1667–1676

Jensen O, Colgin LL (2007) Cross-frequency coupling between neuronal oscillations. Trends in Cognitive Sciences 11:267–269

Jensen O, Lisman JE (2005) Hippocampal sequence-encoding driven by a cortical multi-item working memory buffer. Trends Neurosci 28:67–72

Jensen O, Mazaheri A (2010) Shaping functional architecture by oscillatory alpha activity: gating by inhibition. Front Hum Neurosci 4:186

Ji D, Wilson MA (2007) Coordinated memory replay in the visual cortex and hippocampus during sleep. Nat Neurosci 10:100–107

Jonas P, Major G, Sakmann B (1993) Quantal components of unitary EPSCs at the mossy fibre synapse on CA3 pyramidal cells of rat hippocampus. J Physiol 472:615–663

Jones RS (1994) Synaptic and intrinsic properties of neurons of origin of the perforant path in layer II of the rat entorhinal cortex in vitro. Hippocampus 4:335–353

Jouvet M (1967) Neurophysiology of the states of sleep. Physiol Rev 47:117–177

Juergens E, Guettler A, Eckhorn R (1999) Visual stimulation elicits locked and induced gamma oscillations in monkey intracortical- and EEG-potentials, but not in human EEG. Exp Brain Res 129:247–259

Jung MW, Wiener SI, McNaughton BL (1994) Comparison of spatial firing characteristics of units in dorsal and ventral hippocampus of the rat. J Neurosci 14:7347–7356

Kamondi A, Acsády L, Buzsáki G (1998) Dendritic spikes are enhanced by cooperative network activity in the intact hippocampus. J Neurosci 18:3919–3928

Kamondi A, Acsády L, Wang X-J, Buzsáki G (1998) Theta oscillations in somata and dendrites of hippocampal pyramidal cells in vivo: activity-dependent phase-precession of action potentials. Hippocampus 8:244–261

Kandel ER, Spencer WA (1961) Electrophysiology of hippocampal neurons. II. After-potentials and repetitive firing. J Neurophysiol 24:243–259

Katzner S, Nauhaus I, Benucci A, Bonin V, Ringach DL, Carandini M (2009) Local Origin of Field Potentials in Visual Cortex. Neuron 61:35–41

Kelemen E, Fenton AA (2013) Key Features of Human Episodic Recollection in the Cross-Episode Retrieval of Rat Hippocampus Representations of Space (HB Eichenbaum, Ed.). PLoS Biology 11:e1001607

Kiss J, Buzsàki G, Morrow JS, Glantz SB, Leranth C (1996) Entorhinal cortical innervation of parvalbumin-containing neurons (Basket and Chandelier cells) in the rat Ammon's horn. Hippocampus 6:239–246

Klausberger T, Somogyi P (2008) Neuronal diversity and temporal dynamics: the unity of hippocampal circuit operations. Science 321:53–57

Klausberger T, Magill PJ, Márton LF, Roberts JDB, Cobden PM, Buzsáki G, Somogyi P (2003) Brain-state- and cell-type-specific firing of hippocampal interneurons in vivo. Nature 421:844–848

Klausberger T, Márton LF, Baude A, Roberts JDB, Magill PJ, Somogyi P (2004) Spike timing of dendrite-targeting bistratified cells during hippocampal network oscillations in vivo. Nat Neurosci 7:41–47

Kloosterman F, Layton SP, Chen Z, Wilson MA (2014) Bayesian decoding using unsorted spikes in the rat hippocampus. J Neurophysiol 111:217–227

Koch C, Segev I (1998) Methods in neuronal modeling: from ions to networks . :671

Koch C, Poggio T, Torre V (1983) Nonlinear interactions in a dendritic tree: localization, timing, and role in information processing. Proc Natl Acad Sci USA 80:2799–2802

Kocsis B, Bragin A, Buzsáki G (1999) Interdependence of multiple theta generators in the hippocampus: a partial coherence analysis. J Neurosci 19:6200–6212

Kocsis B, Thinschmidt JS, Kinney GG, Vertes RP (1994) Separation of hippocampal theta dipoles by partial coherence analysis in the rat. Brain Res 660:341–345

Kohara K, Pignatelli M, Rivest AJ, Jung H-Y, Kitamura T, Suh J, Frank D, Kajikawa K, Mise N, Obata Y, Wickersham IR, Tonegawa S (2013) Cell type–specific genetic and optogenetic tools reveal hippocampal CA2 circuits. Nat Neurosci

Komorowski RW, Garcia CG, Wilson A, Hattori S, Howard MW, Eichenbaum H (2013) Ventral hippocampal neurons are shaped by experience to represent behaviorally relevant contexts. J Neurosci 33:8079–8087

Konnerth A, Orkand RK (1986) Voltage-sensitive dyes measure potential changes in axons and glia of the frog optic nerve. Neurosci Lett 66:49–54

Konopacki J, Maciver MB, Bland BH, Roth SH (1987) Carbachol-induced EEG “theta” activity in hippocampal brain slices. Brain Res 405:196–198

Korovaichuk A, Makarova J, Makarov VA, Benito N, Herreras O (2010) Minor contribution of principal excitatory pathways to hippocampal LFPs in the anesthetized rat: a combined independent component and current source density study. J Neurophysiol 104:484–497

Kramis R, Vanderwolf CH, Bland BH (1975) 2 Types of Hippocampal Rhythmical Slow Activity in Both Rabbit and Rat - Relations to Behavior and Effects of Atropine, Diethyl-Ether, Urethane, and Pentobarbital. Exp Neurol 49:58–85

Krupic J, Burgess N, O'Keefe J (2012) Neural representations of location composed of spatially periodic bands. Science 337:853–857

Lapray D, Lasztoczi B, Lagler M, Viney TJ, Katona L, Valenti O, Hartwich K, Borhegyi Z, Somogyi P, Klausberger T (2012) Behavior-dependent specialization of identified hippocampal interneurons. Nat Neurosci

Larkum ME, Waters J, Sakmann B, Helmchen F (2007) Dendritic spikes in apical dendrites of neocortical layer 2/3 pyramidal neurons. J Neurosci 27:8999–9008

Laurent G (1996) Dynamical representation of odors by oscillating and evolving neural assemblies. Trends Neurosci 19:489–496

Le Van Quyen M, Bragin A, Staba R, Crepon B, Wilson CL, Engel J (2008) Cell Type-Specific Firing during Ripple Oscillations in the Hippocampal Formation of Humans. J Neurosci 28:6104–6110

Le Van Quyen M, Foucher J, Lachaux J, Rodriguez E, Lutz A, Martinerie J, Varela FJ (2001) Comparison of Hilbert transform and wavelet methods for the analysis of neuronal synchrony. J Neurosci Methods 111:83–98

Le Van Quyen M, Staba R, Bragin A, Dickson C, Valderrama M, Fried I, Engel J (2010) Large-scale microelectrode recordings of high-frequency gamma oscillations in human cortex during sleep. J Neurosci 30:7770–7782

Leão RN, Mikulovic S, Leão KE, Munguba H, Gezelius H, Enjin A, Patra K, Eriksson A, Loew LM, Tort ABL, Kullander K (2012) OLM interneurons differentially modulate CA3 and entorhinal inputs to hippocampal CA1 neurons. Nat Neurosci 15:1524–1530

Ledberg A, Robbe D (2011) Locomotion-Related Oscillatory Body Movements at 6–12 Hz Modulate the Hippocampal Theta Rhythm. PLoS ONE 6:e27575

Lee I, Yoganarasimha D, Rao G, Knierim JJ (2004) Comparison of population coherence of place cells in hippocampal subfields CA1 and CA3. Nature 430:456–459

Łęski S, Lindén H, Tetzlaff T, Pettersen KH, Einevoll GT (2013) Frequency dependence of signal power and spatial reach of the local field potential. PLoS Comput Biol 9:e1003137

Łęski S, Pettersen KH, Tunstall B, Einevoll GT, Gigg J, Wójcik DK (2011) Inverse current source density method in two dimensions: inferring neural activation from multielectrode recordings. Neuroinformatics 9:401–425

Leung L, Yu H (1998) Theta-frequency resonance in hippocampal CA1 neurons in vitro demonstrated by sinusoidal current injection. J Neurophysiol 79:1592–1596

Leung L-WS (1984) Model of gradual phase shift of theta rhythm in the rat. J Neurophysiol 52:1051–1065

Leung L-WS (1991) Field Potentials in the Central Nervous System (first 4 pages). Neuromethods 15:277–312

Leung LS (1998) Generation of theta and gamma rhythms in the hippocampus. Neuroscience and biobehavioral reviews 22:275–290

Leung LW, Lopes da Silva FH, Wadman WJ (1982) Spectral characteristics of the hippocampal EEG in the freely moving rat. Electroencephalogr Clin Neurophysiol 54:203–219

Leutgeb S, Leutgeb JK (2007) Pattern separation, pattern completion, and new neuronal codes within a continuous CA3 map. Learning & Memory 14:745–757

Leutgeb S, Leutgeb JK, Treves A, Moser M-B, Moser EI (2004) Distinct ensemble codes in hippocampal areas CA3 and CA1. Science 305:1295–1298

Lever C, Burton S, Jeewajee A, Wills TJ, Cacucci F, Burgess N, O'Keefe J (2010) Environmental novelty elicits a later theta phase of firing in CA1 but not subiculum. Hippocampus 20:229–234

Levy WB, Colbert CM, Desmond NL (1995) Another network model bites the dust: entorhinal inputs are no more than weakly excitatory in the hippocampal CA1 region. Hippocampus 5:137–140

Lewicki MS (1998) A review of methods for spike sorting: the detection and classification of neural action potentials. Network 9:R53–78

Li XG, Somogyi P, Ylinen A, Buzsáki G (1994) The hippocampal CA3 network: an in vivo intracellular labeling study. J Comp Neurol 339:181–208

Lichtman JW, Denk W (2011) The Big and the Small: Challenges of Imaging the Brain's Circuits. Science 334:618–623

Lindén H, Pettersen KH, Einevoll GT (2010) Intrinsic dendritic filtering gives low-pass power spectra of local field potentials. J Comp Neurosci 29:423–444

Lindén H, Tetzlaff T, Potjans TC, Pettersen KH, Grün S, Diesmann M, Einevoll GT (2011) Modeling the Spatial Reach of the LFP. Neuron 72:859–872

Lisman JE, Jensen O (2013) The theta-gamma neural code. Neuron 77:1002–1016

Llinás R, Nicholson C (1971) Electrophysiological properties of dendrites and somata in alligator Purkinje cells. J Neurophysiol 34:532–551

Logothetis NK (2003) The underpinnings of the BOLD functional magnetic resonance imaging signal. J Neurosci 23:3963–3971

Logothetis NK, Eschenko O, Murayama Y, Augath M, Steudel T, Evrard HC, Besserve M, Oeltermann A (2012) Hippocampal-cortical interaction during periods of subcortical silence. Nature 491:547–553

Logothetis NK, Kayser C, Oeltermann A (2007) In vivo measurement of cortical impedance spectrum in monkeys: implications for signal propagation. Neuron 55:809–823

London M, Häusser M (2005) Dendritic computation. Annu Rev Neurosci 28:503–532

Lopes-dos-Santos V, Ribeiro S, Tort ABL (2013) Detecting cell assemblies in large neuronal populations. J Neurosci Methods

Losonczy A, Zemelman BV, Vaziri A, Magee JC (2010) Network mechanisms of theta related neuronal activity in hippocampal CA1 pyramidal neurons. Nat Neurosci 13:967–972

Lovett-Barron M, Turi GF, Kaifosh P, Lee PH, Bolze F, Sun X-H, Nicoud J-F, Zemelman BV, Sternson SM, Losonczy A (2012) Regulation of neuronal input transformations by tunable dendritic inhibition. Nat Neurosci 15:423–30– S1–3

López-Aguado L, Ibarz JM, Herreras O (2001) Activity-dependent changes of tissue resistivity in the CA1 region in vivo are layer-specific: modulation of evoked potentials. Neuroscience 108:249–262

Lubenov EV, Siapas AG (2009) Hippocampal theta oscillations are travelling waves. Nature 459:534–539

Maccaferri G, Roberts JD, Szucs P, Cottingham CA, Somogyi P (2000) Cell surface domain specific postsynaptic currents evoked by identified GABAergic neurones in rat hippocampus in vitro. J Physiol 524 Pt 1:91–116

Maier N, Tejero-Cantero A, Dorrn AL, Winterer J, Beed PS, Morris G, Kempter R, Poulet JFA, Leibold C, Schmitz D (2011) Coherent Phasic Excitation during Hippocampal Ripples. Neuron 72:137–152

Makara JK, Magee JC (2013) Variable Dendritic Integrationin Hippocampal CA3 Pyramidal Neurons. Neuron 80:1438–1450

Makarov VA, Makarova J, Herreras O (2010) Disentanglement of local field potential sources by independent component analysis. J Comp Neurosci 29:445–457

Makarova J, Ibarz JM, Makarov VA, Benito N, Herreras O (2011) Parallel readout of pathway-specific inputs to laminated brain structures. Front Sys Neurosci 5:77

Makeig S, Jung TP, Bell AJ, Ghahremani D, Sejnowski TJ (1997) Blind separation of auditory event-related brain responses into independent components. Proc Natl Acad Sci USA 94:10979–10984

Mann EO, Mody I (2010) Control of hippocampal gamma oscillation frequency by tonic inhibition and excitation of interneurons. Nat Neurosci 13:205–212

Manning JR, Jacobs J, Fried I, Kahana MJ (2009) Broadband Shifts in Local Field Potential Power Spectra Are Correlated with Single-Neuron Spiking in Humans. J Neurosci 29:13613–13620

Manns JR, Eichenbaum H (2009) A cognitive map for object memory in the hippocampus. Learn Mem 16:616–624

Marder E, Bucher D (2007) Understanding circuit dynamics using the stomatogastric nervous system of lobsters and crabs. Annu Rev Physiol 69:291–316

Markram H (2012) The human brain project. Scientific American 306:50–55

Marr D (1971) Simple memory: a theory for archicortex. Philos Trans R Soc Lond, B, Biol Sci 262:23–81

Matsuo F, Peters JF, Reilly EL (1975) Electrical phenomena associated with movements of the eyelid. Electroencephalogr Clin Neurophysiol 38:507–511

Megías A, Emri Z, Freund TF, Gulyás AI (2001) Total number and distribution of inhibitory and excitatory synapses on hippocampal CA1 pyramidal cells. Neuroscience 102:527–540

Menon V, Musial TF, Liu A, Katz Y, Kath WL, Spruston N, Nicholson DA (2013) Balanced Synaptic Impact via Distance-Dependent Synapse Distribution and Complementary Expression of AMPARs and NMDARs in Hippocampal Dendrites. Neuron 80:1451–1463

Middleton S, Jalics J, Kispersky T, LeBeau FEN, Roopun AK, Kopell NJ, Whittington MA, Cunningham MO (2008) NMDA receptor-dependent switching between different gamma rhythm-generating microcircuits in entorhinal cortex. Proc Natl Acad Sci USA 105:18572–18577

Miles R, Tóth K, Gulyás AI, Hájos N, Freund TF (1996) Differences between somatic and dendritic inhibition in the hippocampus. Neuron 16:815–823

Miller KJ (2010) Broadband spectral change: evidence for a macroscale correlate of population firing rate? J Neurosci 30:6477–6479

Mitchell SJ, Ranck JB (1980) Generation of theta rhythm in medial entorhinal cortex of freely moving rats. Brain Res 189:49–66

Mitzdorf U (1985) Current source-density method and application in cat cerebral cortex: investigation of evoked potentials and EEG phenomena. Physiol Rev 65:37–100

Mizuseki K, Buzsáki G (2013) Preconfigured, skewed distribution of firing rates in the hippocampus and entorhinal cortex. Cell Rep 4:1010–1021

Mizuseki K, Buzsáki G (2014) Theta oscillations decrease spike synchrony in the hippocampus and entorhinal cortex. Philosophical Transactions of the Royal Society B: Biological Sciences 369:20120530

Mizuseki K, Diba K, Pastalkova E, Buzsáki G (2011) Hippocampal CA1 pyramidal cells form functionally distinct sublayers. Nat Neurosci 14:1174–1181

Mizuseki K, Royer S, Diba K, Buzsáki G (2012) Activity dynamics and behavioral correlates of CA3 and CA1 hippocampal pyramidal neurons. Hippocampus

Mizuseki K, Sirota A, Pastalkova E, Buzsáki G (2009) Theta oscillations provide temporal windows for local circuit computation in the entorhinal-hippocampal loop. Neuron 64:267–280

Moca VV, Nikolic D, Singer W, Muresan RC (2013) Membrane Resonance Enables Stable and Robust Gamma Oscillations. Cereb Cortex 24:119–142

Montgomery SM, Buzsàki G (2007) Gamma oscillations dynamically couple hippocampal CA3 and CA1 regions during memory task performance. Proc Natl Acad Sci USA 104:14495–14500

Montgomery SM, Betancur MI, Buzsáki G (2009) Behavior-dependent coordination of multiple theta dipoles in the hippocampus. J Neurosci 29:1381–1394

Montgomery SM, Sirota A, Buzsáki G (2008) Theta and gamma coordination of hippocampal networks during waking and rapid eye movement sleep. J Neurosci 28:6731–6741

Moore BR (1980) A Modification of the Rayleigh Test for Vector Data. Biometrika 67:175–180

Moore GP, Segundo JP, Perkel DH, Levitan H (1970) Statistical signs of synaptic interaction in neurons. Biophys J 10:876–900

Moore JD, Deschênes M, Furuta T, Huber D, Smear MC, Demers M, Kleinfeld D (2013) Hierarchy of orofacial rhythms revealed through whisking and breathing. Nature

Mori M, Gähwiler BH, Gerber U (2007) Recruitment of an inhibitory hippocampal network after bursting in a single granule cell. Proc Natl Acad Sci USA 104:7640–7645

Mormann F, Fell J, Axmacher N, Weber B, Lehnertz K, Elger CE, Fernández G (2005) Phase/amplitude reset and theta-gamma interaction in the human medial temporal lobe during a continuous word recognition memory task. Hippocampus 15:890–900

Moser EI, Kropff E, Moser M-B (2008) Place cells, grid cells, and the brain's spatial representation system. Annu Rev Neurosci 31:69–89

Moser EI, Moser MB, Andersen P (1993) Spatial-Learning Impairment Parallels the Magnitude of Dorsal Hippocampal-Lesions, but Is Hardly Present Following Ventral Lesions. J Neurosci 13:3916–3925

Muller RU, Kubie JL, Ranck JB (1987) Spatial firing patterns of hippocampal complex-spike cells in a fixed environment. J Neurosci 7:1935–1950

Mureşan RC, Jurjuţ OF, Moca VV, Singer W, Nikolić D (2008) The oscillation score: an efficient method for estimating oscillation strength in neuronal activity. J Neurophysiol 99:1333–1353

Muthukumaraswamy SD (2013) High-frequency brain activity and muscle artifacts in MEG/EEG: a review and recommendations. Front Hum Neurosci 7:138

Müller C, Beck H, Coulter D, Remy S (2012) Inhibitory Control of Linear and Supralinear Dendritic Excitation in CA1 Pyramidal Neurons. Neuron 75:851–864

Nakashiba T, Buhl DL, McHugh TJ, Tonegawa S (2009) Hippocampal CA3 Output Is Crucial for Ripple- Associated Reactivation and Consolidation of Memory. Neuron 62:781–787

Nakashiba T, Young JZ, McHugh TJ, Buhl DL, Tonegawa S (2008) Transgenic inhibition of synaptic transmission reveals role of CA3 output in hippocampal learning. Science 319:1260–1264

Nguyen DP, Layton SP, Hale G, Gomperts SN, Davidson TJ, Kloosterman F, Wilson MA (2009) Micro-drive array for chronic in vivo recording: tetrode assembly. J Vis Exp

Nicholson C (1973) Theoretical analysis of field potentials in anisotropic ensembles of neuronal elements. IEEE transactions on bio-medical engineering 20:278–288

Nicholson C, Freeman JA (1975) Theory of current source-density analysis and determination of conductivity tensor for anuran cerebellum. J Neurophysiol 38:356–368

Nicholson C, Llinás R (1971) Field potentials in the alligator cerebellum and theory of their relationship to Purkinje cell dendritic spikes. J Neurophysiol 34:509–531

Nörenberg A, Hu H, Vida I, Bartos M, Jonas P (2010) Distinct nonuniform cable properties optimize rapid and efficient activation of fast-spiking GABAergic interneurons. Proc Natl Acad Sci USA 107:894–899

O'Donnell RD, Berkhout J, Adey WR (1974) Contamination of scalp EEG spectrum during contraction of cranio-facial muscles. Electroencephalogr Clin Neurophysiol 37:145–151

O'Keefe J, Nadel L (1978) The Hippocampus as a Cognitive Map. Clarendon Press

O'Keefe J, Recce ML (1993) Phase relationship between hippocampal place units and the EEG theta rhythm. Hippocampus 3:317–330

Olbrich HG, Braak H (1985) Ratio of pyramidal cells versus non-pyramidal cells in sector CA1 of the human Ammon's horn. Anat Embryol 173:105–110

Orr G, Rao G, Houston FP, McNaughton BL, Barnes CA (2001) Hippocampal synaptic plasticity is modulated by theta rhythm in the fascia dentata of adult and aged freely behaving rats. Hippocampus 11:647–654

Pastalkova E, Itskov V, Amarasingham A, Buzsáki G (2008) Internally generated cell assembly sequences in the rat hippocampus. Science 321:1322–1327

Pastoll H, Ramsden HL, Nolan MF (2012) Intrinsic electrophysiological properties of entorhinal cortex stellate cells and their contribution to grid cell firing fields. Front Neural Circuits 6:1–21

Patel J, Fujisawa S, Berényi A, Royer S, Buzsáki G (2012) Traveling Theta Waves along the Entire Septotemporal Axis of the Hippocampus. Neuron 75:410–417

Patel J, Schomburg EW, Berényi A, Fujisawa S, Buzsáki G (2013) Local Generation and Propagation of Ripples along the Septotemporal Axis of the Hippocampus. J Neurosci 33:17029–17041

Pavlides C, Greenstein YJ, Grudman M, Winson J (1988) Long-term potentiation in the dentate gyrus is induced preferentially on the positive phase of theta-rhythm. Brain Res 439:383–387

Penttonen M, Kamondi A, Acsády L, Buzsàki G (1998) Gamma frequency oscillation in the hippocampus of the rat: intracellular analysis in vivo. Eur J Neurosci 10:718–728

Percival DB, Walden AT (1993) Spectral analysis for physical applications: multitaper and conventional univariate techniques. Cambridge, UK: Cambridge UP

Perkel DH, Gerstein GL, Moore GP (1967) Neuronal spike trains and stochastic point processes. II. Simultaneous spike trains. Biophys J 7:419–440

Pernía-Andrade AJ, Jonas P (2013) Theta-Gamma-Modulated Synaptic Currents in Hippocampal Granule Cells In Vivo Define a Mechanism for Network Oscillations. Neuron:1–13

Pettersen KH, Einevoll GT (2008) Amplitude variability and extracellular low-pass filtering of neuronal spikes. Biophys J 94:784–802

Pettersen KH, Devor A, Ulbert I, Dale AM, Einevoll GT (2006) Current-source density estimation based on inversion of electrostatic forward solution: effects of finite extent of neuronal activity and conductivity discontinuities. J Neurosci Methods 154:116–133

Peyrache A, Khamassi M, Benchenane K, Wiener SI, Battaglia FP (2009) Replay of rule-learning related neural patterns in the prefrontal cortex during sleep. Nat Neurosci 12:919–926

Pfeiffer BE, Foster DJ (2013) Hippocampal place-cell sequences depict future paths to remembered goals. Nature 497:74–79

Pietersen ANJ, Ward PD, Hagger-Vaughan N, Wiggins J, Jefferys JGR, Vreugdenhil M (2014) Transition between fast and slow gamma modes in rat hippocampus area CA1 in vitro is modulated by slow CA3 gamma oscillations. J Physiol 592:605–620

Plonsey R, Heppner DB (1967) Considerations of quasi-stationarity in electrophysiological systems. Bull Math Biophys 29:657–664

Poe GR, Nitz DA, McNaughton BL, Barnes CA (2000) Experience-dependent phase-reversal of hippocampal neuron firing during REM sleep. Brain Res 855:176–180

Pouille F, Scanziani M (2001) Enforcement of temporal fidelity in pyramidal cells by somatic feed-forward inhibition. Science 293:1159–1163

Quian Quiroga R (2007) Spike sorting. Scholarpedia 2(12):3583

Quian Quiroga R, Panzeri S (2009) Extracting information from neuronal populations: information theory and decoding approaches. Nat Rev Neurosci 10:173–185

Quilichini P, Sirota A, Buzsáki G (2010) Intrinsic circuit organization and theta-gamma oscillation dynamics in the entorhinal cortex of the rat. J Neurosci 30:11128–11142

Rall W (1962) Electrophysiology of a dendritic neuron model. Biophys J 2:145–167

Rall W (1967) Distinguishing theoretical synaptic potentials computed for different soma-dendritic distributions of synaptic input. J Neurophysiol 30:1138–1168

Rall W, Shepherd GM (1968) Theoretical reconstruction of field potentials and dendrodendritic synaptic interactions in olfactory bulb. J Neurophysiol 31:884–915

Rall W, Shepherd GM, Reese TS, Brightman MW (1966) Dendrodendritic synaptic pathway for inhibition in the olfactory bulb. Exp Neurol 14:44–56

Ray S, Maunsell JHR (2011a) Different origins of gamma rhythm and high-gamma activity in macaque visual cortex. PLoS Biology 9:e1000610–

Ray S, Maunsell JHR (2011b) Network Rhythms Influence the Relationship between Spike-Triggered Local Field Potential and Functional Connectivity. J Neurosci 31:12674–12682

Ray S, Niebur E, Hsiao SS, Sinai A, Crone NE (2008a) High-frequency gamma activity (80-150Hz) is increased in human cortex during selective attention. Clin Neurophysiol 119:116–133

Ray S, Hsiao SS, Crone NE, Franaszczuk PJ, Niebur E (2008b) Effect of stimulus intensity on the spike-local field potential relationship in the secondary somatosensory cortex. J Neurosci 28:7334–7343

Ray S, Crone NE, Niebur E, Franaszczuk PJ, Hsiao SS (2008c) Neural correlates of high-gamma oscillations (60-200 Hz) in macaque local field potentials and their potential implications in electrocorticography. J Neurosci 28:11526–11536

Reichinnek S, Künsting T, Draguhn A, Both M (2010) Field potential signature of distinct multicellular activity patterns in the mouse hippocampus. J Neurosci 30:15441–15449

Remondes M, Schuman EM (2002) Direct cortical input modulates plasticity and spiking in CA1 pyramidal neurons. Nature 416:736–740

Remondes M, Schuman EM (2004) Role for a cortical input to hippocampal area CA1 in the consolidation of a long-term memory. Nature 431:699–703

Renart A, la Rocha de J, Bartho P, Hollender L, Parga N, Reyes A, Harris KD (2010) The asynchronous state in cortical circuits. Science 327:587–590

Roitbak AI, Fanardjian VV, Melkonyan DS, Melkonyan AA (1987) Contribution of glia and neurons to the surface-negative potentials of the cerebral cortex during its electrical stimulation. Neuroscience 20:1057–1067

Royer S, Sirota A, Patel J, Buzsáki G (2010) Distinct representations and theta dynamics in dorsal and ventral hippocampus. J Neurosci 30:1777–1787

Royer S, Zemelman BV, Losonczy A, Kim J, Chance F, Magee JC, Buzsáki G (2012) Control of timing, rate and bursts of hippocampal place cells by dendritic and somatic inhibition. Nat Neurosci 15:769–775

Sabolek HR, Penley SC, Hinman JR, Bunce JG, Markus EJ, Escabi M, Chrobak JJ (2009) Theta and gamma coherence along the septotemporal axis of the hippocampus. J Neurophysiol 101:1192–1200

Sargolini F, Fyhn M, Hafting T, McNaughton BL, Witter MP, Moser M-B, Moser EI (2006) Conjunctive representation of position, direction, and velocity in entorhinal cortex. Science 312:758–762

Sasaki K, Ono T, Nishino H, Fukuda M, Muramoto KI (1983) A method for long-term artifact-free recording of single unit activity in freely moving, eating and drinking animals. J Neurosci Methods 7:43–47

Sayer RJ, Redman SJ, Andersen P (1989) Amplitude fluctuations in small EPSPs recorded from CA1 pyramidal cells in the guinea pig hippocampal slice. J Neurosci 9:840–850

Scheffer-Teixeira R, Belchior H, Leão RN, Ribeiro S, Tort ABL (2013) On high-frequency field oscillations (>100 Hz) and the spectral leakage of spiking activity. J Neurosci 33:1535–1539

Scheffzük C, Kukushka VI, Vyssotski AL, Draguhn A, Tort ABL, Brankack J (2011) Selective coupling between theta phase and neocortical fast gamma oscillations during REM-sleep in mice. PLoS ONE 6:e28489

Schmidt B, Hinman JR, Jacobson TK, Szkudlarek E, Argraves M, Escabí MA, Markus EJ (2013) Dissociation between Dorsal and Ventral Hippocampal Theta Oscillations during Decision-Making. J Neurosci 33:6212–6224

Schmitzer-Torbert N, Jackson J, Henze D, Harris K, Redish AD (2005) Quantitative measures of cluster quality for use in extracellular recordings. Neuroscience 131:1–11

Schomburg EW, Anastassiou CA, Buzsáki G, Koch C (2012) The spiking component of oscillatory extracellular potentials in the rat hippocampus. J Neurosci 32:11798–11811

Senior TJ, Huxter JR, Allen K, O'Neill J, Csicsvari J (2008) Gamma oscillatory firing reveals distinct populations of pyramidal cells in the CA1 region of the hippocampus. J Neurosci 28:2274–2286

Shinohara Y, Hosoya A, Hirase H (2013) Experience enhances gamma oscillations and interhemispheric asymmetry in the hippocampus. Nat Commun 4:1652

Siapas AG, Wilson MA (1998) Coordinated interactions between hippocampal ripples and cortical spindles during slow-wave sleep. Neuron 21:1123–1128

Sik A, Ylinen A, Penttonen M, Buzsàki G (1994) Inhibitory CA1-CA3-hilar region feedback in the hippocampus. Science 265:1722–1724

Singer W, Gray CM (1995) Visual feature integration and the temporal correlation hypothesis. Annu Rev Neurosci 18:555–586

Sirota A, Montgomery S, Fujisawa S, Isomura Y, Zugaro M, Buzsáki G (2008) Entrainment of neocortical neurons and gamma oscillations by the hippocampal theta rhythm. Neuron 60:683–697

Skaggs WE, McNaughton BL (1996) Replay of neuronal firing sequences in rat hippocampus during sleep following spatial experience. Science 271:1870–1873

Skaggs WE, McNaughton BL, Wilson MA, Barnes CA (1996) Theta phase precession in hippocampal neuronal populations and the compression of temporal sequences. Hippocampus 6:149–172

Solstad T, Boccara CN, Kropff E, Moser M-B, Moser EI (2008) Representation of geometric borders in the entorhinal cortex. Science 322:1865–1868

Soltesz I, Deschênes M (1993) Low- and high-frequency membrane potential oscillations during theta activity in CA1 and CA3 pyramidal neurons of the rat hippocampus under ketamine-xylazine anesthesia. J Neurophysiol 70:97–116

Spruston N (2008) Pyramidal neurons: dendritic structure and synaptic integration. Nat Rev Neurosci 9:206–221

Squire LR (1992) Memory and the hippocampus: a synthesis from findings with rats, monkeys, and humans. Psychological Review 99:195–231

Staba RJ, Wilson CL, Bragin A, Fried I, Engel J (2002) Quantitative analysis of high-frequency oscillations (80-500 Hz) recorded in human epileptic hippocampus and entorhinal cortex. J Neurophysiol 88:1743–1752

Staley KJ (2007) Neurons skip a beat during fast ripples. Neuron 55:828–830

Stark E, Abeles M (2009) Unbiased estimation of precise temporal correlations between spike trains. J Neurosci Methods 179:90–100

Stark E, Eichler R, Roux L, Fujisawa S, Rotstein HG, Buzsáki G (2013) Inhibition-Induced Theta Resonance in Cortical Circuits. Neuron 80:1263–1276

Steriade M (2006) Grouping of brain rhythms in corticothalamic systems. Neuroscience 137:1087–1106

Storm JF (1987) Action potential repolarization and a fast after-hyperpolarization in rat hippocampal pyramidal cells. J Physiol 385:733–759

Storm JF (1989) An after-hyperpolarization of medium duration in rat hippocampal pyramidal cells. J Physiol 409:171–190

Suh J, Rivest AJ, Nakashiba T, Tominaga T, Tonegawa S (2011) Entorhinal cortex layer III input to the hippocampus is crucial for temporal association memory. Science 334:1415–1420

Sullivan D, Csicsvari J, Mizuseki K, Montgomery S, Diba K, Buzsaki G (2011) Relationships between Hippocampal Sharp Waves, Ripples, and Fast Gamma Oscillation: Influence of Dentate and Entorhinal Cortical Activity. J Neurosci 31:8605–8616

Syková E, Nicholson C (2008) Diffusion in brain extracellular space. Physiol Rev 88:1277–1340

Takahashi H, Magee JC (2009) Pathway interactions and synaptic plasticity in the dendritic tuft regions of CA1 pyramidal neurons. Neuron 62:102–111

Takahashi M, Lauwereyns J, Sakurai Y, Tsukada M (2009) Behavioral state-dependent episodic representations in rat CA1 neuronal activity during spatial alternation. Cognitive neurodynamics 3:165–175

Takahashi N, Kitamura K, Matsuo N, Mayford M, Kano M, Matsuki N, Ikegaya Y (2012) Locally synchronized synaptic inputs. Science 335:353–356

Taxidis J, Coombes S, Mason R, Owen MR (2011) Modeling sharp wave-ripple complexes through a CA3-CA1 network model with chemical synapses. Hippocampus

Thompson LT, Best PJ (1989) Place cells and silent cells in the hippocampus of freely-behaving rats. J Neurosci 9:2382–2390

Tiesinga P, Sejnowski TJ (2009) Cortical Enlightenment: Are Attentional Gamma Oscillations Driven by ING or PING? Neuron 63:727–732

Tort ABL, Komorowski RW, Manns JR, Kopell NJ, Eichenbaum H (2009) Theta-gamma coupling increases during the learning of item-context associations. Proc Natl Acad Sci USA 106:20942–20947

Tort ABL, Kramer MA, Thorn C, Gibson DJ, Kubota Y, Graybiel AM, Kopell NJ (2008) Dynamic cross-frequency couplings of local field potential oscillations in rat striatum and hippocampus during performance of a T-maze task. Proc Natl Acad Sci USA 105:20517–20522

Traub RD, Bibbig A (2000) A model of high-frequency ripples in the hippocampus based on synaptic coupling plus axon-axon gap junctions between pyramidal neurons. J Neurosci 20:2086–2093

Traub RD, Jefferys JGR, Whittington MA (1997) Simulation of gamma rhythms in networks of interneurons and pyramidal cells. J Comp Neurosci 4:141–150

Traub RD, Whittington MA, Stanford IM, Jefferys JG (1996) A mechanism for generation of long-range synchronous fast oscillations in the cortex. Nature 383:621–624

Tukker JJ, Fuentealba P, Hartwich K, Somogyi P, Klausberger T (2007) Cell type-specific tuning of hippocampal interneuron firing during gamma oscillations in vivo. J Neurosci 27:8184–8189

Vaidya SP, Johnston D (2013) Temporal synchrony and gamma-to-theta power conversion in the dendrites of CA1 pyramidal neurons. Nat Neurosci:1–11

Vandecasteele M, M S, Royer S, Belluscio M, Berényi A, Diba K, Fujisawa S, Grosmark A, Mao D, Mizuseki K, Patel J, Stark E, Sullivan D, Watson B, Buzsáki G (2012) Large-scale recording of neurons by movable silicon probes in behaving rodents. J Vis Exp:e3568

Vanderwolf CH (1969) Hippocampal electrical activity and voluntary movement in the rat. Electroencephalogr Clin Neurophysiol 26:407–418

Vanrullen R, Dubois J (2011) The psychophysics of brain rhythms. Front Psychology 2:203

Varga C, Golshani P, Soltesz I (2012) Frequency-invariant temporal ordering of interneuronal discharges during hippocampal oscillations in awake mice. Proc Natl Acad Sci USA 109:E2726–34

Viney TJ, Lasztoczi B, Katona L, Crump MG, Tukker JJ, Klausberger T, Somogyi P (2013) Network state-dependent inhibition of identified hippocampal CA3 axo-axonic cells in vivo. Nat Neurosci 16:1802–1811

Waldert S, Lemon RN, Kraskov A (2013) Influence of spiking activity on cortical local field potentials. J Physiol 591:5291–5303

Wang X-J, Buzsáki G (1996) Gamma oscillation by synaptic inhibition in a hippocampal interneuronal network model. J Neurosci 16:6402–6413

Wang XJ (2010) Neurophysiological and Computational Principles of Cortical Rhythms in Cognition. Physiol Rev 90:1195–1268

Weiss SA, Faber DS (2010) Field effects in the CNS play functional roles. Front Neural Circuits 4:15

Whittington MA, Cunningham MO, Lebeau FEN, Racca C, Traub RD (2010) Multiple origins of the cortical gamma rhythm. Dev Neurobiol

Whittington MA, Traub RD, Jefferys JG (1995) Synchronized oscillations in interneuron networks driven by metabotropic glutamate receptor activation. Nature 373:612–615

Wierzynski CM, Lubenov EV, Gu M, Siapas AG (2009) State-dependent spike-timing relationships between hippocampal and prefrontal circuits during sleep. Neuron 61:587–596

Wilson MA, McNaughton BL (1994) Reactivation of hippocampal ensemble memories during sleep. Science 265:676–679

Ylinen A, Soltesz I, Bragin A, Penttonen M, Sik A, Buzsàki G (1995a) Intracellular correlates of hippocampal theta rhythm in identified pyramidal cells, granule cells, and basket cells. Hippocampus 5:78–90

Ylinen A, Bragin A, Nádasdy Z, Jando G, Szabó I, Sik A, Buzsáki G (1995b) Sharp wave-associated high-frequency oscillation (200 Hz) in the intact hippocampus: network and intracellular mechanisms. J Neurosci 15:30–46

Zanos TP, Mineault PJ, Pack CC (2011) Removal of spurious correlations between spikes and local field potentials. J Neurophysiol 105:474–486

Zemankovics R, Veres JM, Oren I, Hájos N (2013) Feedforward inhibition underlies the propagation of cholinergically induced gamma oscillations from hippocampal CA3 to CA1. J Neurosci 33:12337–12351